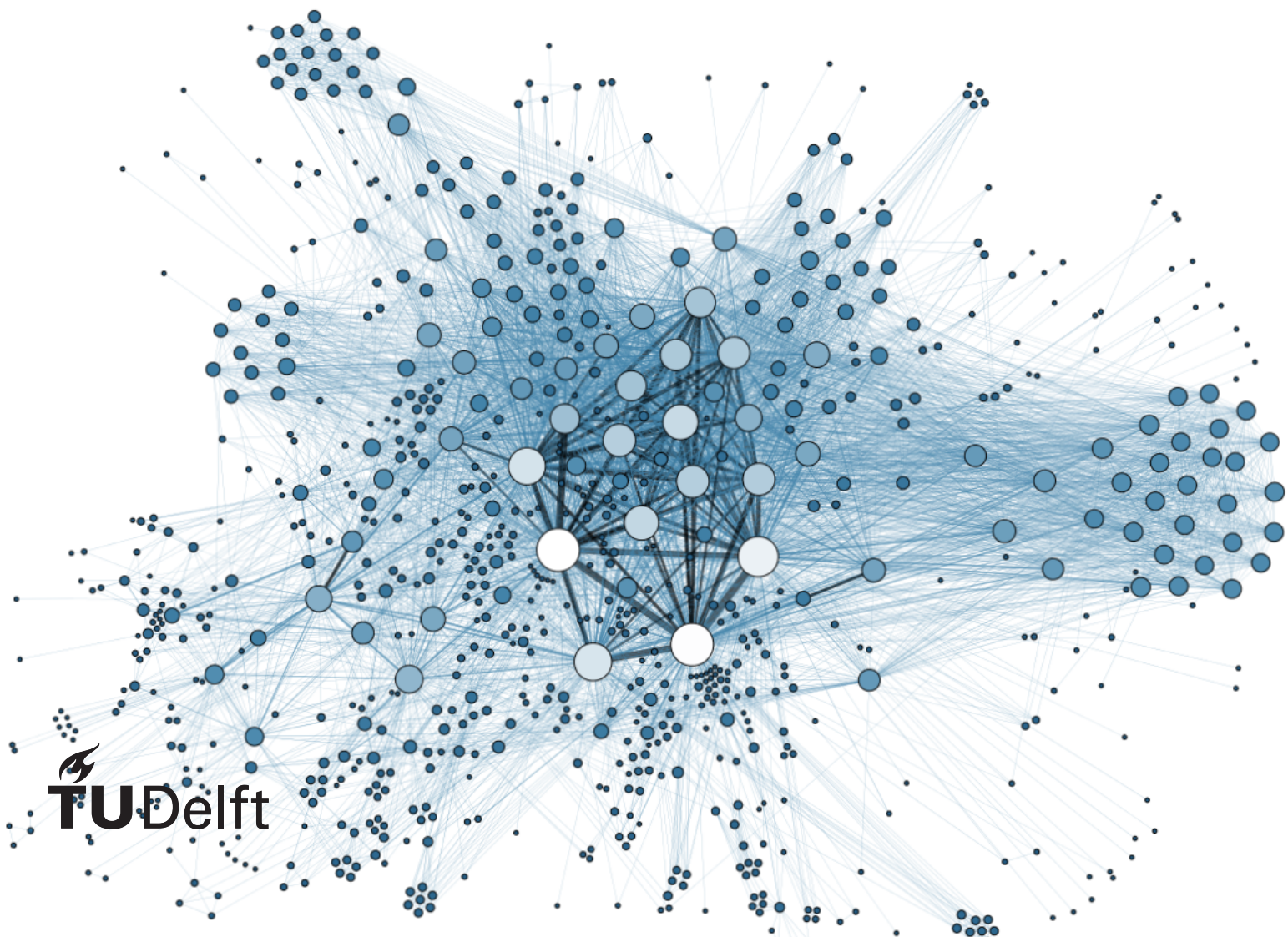


Expanding the Abilities of Impact Testing for Rubber Characterization

Using an inverse approach for extracting material properties

W. de Roos



Expanding the Abilities of Impact Testing for Rubber Characterization

*Using an inverse approach for extracting
material properties*

by

W. de Roos

to obtain the degree of Master of Science
at the Delft University of Technology,
to be defended publicly on Monday April 15, 2019 at 14:00 PM.

Student number: 4234278
Project duration: October 1, 2017 – April 15, 2019
Thesis committee: Dr. ir. R. Happee, TU Delft, Chairman
Dr. ir. D. de Klerk, TU Delft, Supervisor
Dr. ir. K.M.B Jansen TU Delft
Ir. E. Pasma, Vibes, Company Supervisor

This thesis is confidential and cannot be made public until April 15, 2019.

An electronic version of this thesis is available at <http://repository.tudelft.nl/>.

Preface

Roughly twelve years back I started my MBO study automotive after a difficult secondary school period. From that point onwards I followed all degrees of education up to now where I am graduating for a master's degree in vehicle engineering. Reaching this final goal after twelve years makes me very proud. I am grateful for all the support I got from my dear ones during this long period. Mostly I would like to thank my Annemarijn, who is my girlfriend for already more than seven years. She always was supportive and compassionate, even so she is happy to start with the "ordinary non-studying lives". In general I would like to thank the Vibes.technology crew who were always friendly and helpful. Also the Vibes software, Dirac and the Vibes toolbox, where very helpful tools during this research. In particular I want to thank my supervisors Dennis de Klerk and Eric Pasma for giving the opportunity to graduate at Vibes and guiding me during this research.

The limitations that were faced in this research resulted in creative solutions. I think what followed is a research with a different twist. In my opinion the presented method is a good alternative for current ones. The method proves its potential for material properties characterization with limited experimental effort.

*W. de Roos
Delft, April 2019*

Abstract

Vibrations are experienced as unwanted dynamic motions and the industry takes a lot of care to reduce these motions to improve comfort and to increase vehicle component durability. The properties of rubber, being generally soft while showing large inherent damping, makes the material a perfect choice to use in vibration isolators. To minimize vibrations the transfer path from vibrational source to the driver almost always includes a highly damped material like rubber. With the current trend of electrification in the automotive industry, higher order vibrations are becoming more pronounced. Although the produced sound is not of a high octave with respect to traditional combustion engines, they are experienced as unpleasant. Considering a large frequency range, the dynamic characterization of a rubber object is proven to be a difficult topic. In the search of improved rubber characterization new methods arise.

The goal of this research is to provide a new approach for extracting material properties from the experimental impact method. Literature research is done on the rubber specific behaviour and how this affects the modelling approach. In the research itself both numerical and experimental characterization is used. Through impact testing the receptance of the rubber object is measured and by applying inverse substructuring the dynamic stiffness is obtained. The Finite Element model is used to directly obtain the dynamic stiffness. The numerical and experimental results are made comparable by applying the virtual point transformation method. With the finite element material model being the optimization variable, the numerical dynamic stiffness is optimized to match the experimental results. The rubber properties are obtained from the optimized material model.

The presented inverse approach makes it possible to use the impact method for characterizing rubber material properties. It therefore broadens the abilities of impact testing used for rubber characterization. With the new method the drivingpoint properties can be predicted which do not depend on complex decoupling methods. The obtained material properties are material, but not geometry related. The findings can be used for different geometries of the same rubber. The new approach has the ability to significantly reduce experimental effort because the material properties can be extracted from one single loadcase, whereas the experimental should excite all loadcases to fully characterize the dynamic stiffness.

Contents

Abstract	ii
I Part One - Literature Review	1
1 Introduction	2
1.1 Fundamentals of Rubber	3
2 Rubber Behaviour	4
2.1 Incompressible	4
2.2 Hyperelastic.	4
2.3 Viscoelastic	6
2.4 Stiffness effects	11
2.5 Conclusion on rubber behaviour	15
3 Modelling Rubber Behaviour	16
3.1 Hyperelastic Material Models	16
3.2 Viscoelastic Material Models	19
3.3 Conclusion on rubber modelling	25
4 Experimental Characterization	26
4.1 Hyperelasticity	26
4.2 Viscoelasticity.	27
5 Summary and Conclusion	28
6 Master Thesis Approach	31
II Part Two - Thesis	33
7 Case Introduction	34
7.1 Context and Problem Statement	34
7.2 Approach and Challenges.	34
7.3 Contributions.	35
7.4 Research object	35
8 Numerical	37
8.1 Approach	37
8.2 FE Model	37
8.3 Material model	41
8.4 Dynamic Simulation	46
8.5 Quality of results	47
9 Experimental	49
9.1 Introduction	49
9.2 Approach	50
9.3 Equipment	52
9.4 Validation models.	55
9.5 Results	58
10 Material Model Optimization	65
10.1 Optimization approach	65
10.2 Results	67
10.3 Improvements	71

11 Validation	73
11.1 Model update	73
11.2 Drivingpoint-stiffness validation	74
11.3 Drivingpoint-Stiffness Rubber	77
12 Conclusions and Recommendations	79
12.1 Recap	79
12.2 Conclusions.	80
12.3 Recommendations	81
Bibliography	82
A Theoretical Background	87
A.1 Virtual Point Theory	87
B Parameters	89
B.1 DMA data	89
B.2 Material model	89
B.3 Equipment	90
C Impact variation effects on untransformed FRFs	92
C.1 Effect of Impact Position	92
C.2 Effect of Impact Direction.	96
C.3 Averaging of FRFs	99
C.4 Summary	101
D Software	103
D.1 Software interaction	103
D.2 Data-processing	104
E Additional Experimental Results	106
E.1 Validating matrix symmetry.	106

List of abbreviations

FRF:	F requency R esponse F unction
FE:	F inite E lement
VP:	V irtual P oint
RBE:	R igid B ody E lement
NR:	N atural R ubber
DMA:	D ynamic M echanical A nalysis
IRHD:	I nternational R ubber H ardness D egree
TS:	T ransmission S imulator
SNR:	S ignal-to- N oise R atio
DoF:	D egree o f F reedom
TF:	T ransfer F unction

I

Part One - Literature Review



Introduction

In automotive industry, costumers are very demanding on the product they buy. The demand on comfort level rises and vibrations are a key feature which effects comfort. Vibrations are normally experienced as unwanted dynamic motions and the industry takes a lot of care to reduce these motions to improve comfort and to increase vehicle component durability. Humans experiencing vibrations through body movement and noise.

Energy of the vibration source needs to be reflected or absorbed. This can be done by significantly changing the impedance or inducing additional damping respectively. Aforementioned can be achieved by introducing a much softer component compared to the surrounding structure or an increase in mass. Increasing the mass will come with a penalty in the form of increased fuel consumption. In practice therefore changing the impedance is done by introducing a vibration isolator. The properties of rubber, being generally soft while showing large inherent damping, makes the material a perfect choice for use in vibration isolators. To minimize vibrations the transfer path from vibrational source to driver almost always includes a highly damped material like rubber.

With the current trend of electrification in the automotive industry, higher order vibrations are becoming more pronounced. Although the sound level is not of a high octave level in comparison to traditional combustion engines, they are experienced as striking and unpleasant [22] [22]. The focus on a larger frequency range adds complexity to the analysis. The nonlinear and highly damped behaviour of rubber becomes even more pronounced which makes it very challenging to characterize. The goal is the master thesis is to predict the dynamic behaviour using a finite element (FE) model. If the rubber behaviour can be modelled correctly this result can be extrapolated, whereas experimental characterizing of one mount limits the use of results. The quality of vibration noise analysis can be significantly improved when the complex rubber behaviour can be modelled within a FE program.

Knowledge is needed to reach the goal of this thesis. The goal of this literature review is to determine *how and which rubber specific behaviour must be included in a numerical model to properly predict the dynamic behaviour of a rubber engine mount under steady-state conditions?*

Sub-questions answered in this literature review are;

- What behaviour is rubber specific?
- Which mechanisms inside the material result in the rubber specific behaviour?
- Which external factors trigger these rubber specific material behaviour?
- What behaviour is relevant for this application?
- How can the relevant behavioural effects be represented within a material model?
- What experiments provide sufficient information?
- How is the dynamic behaviour of a certain geometry effected by the choice of material model?

1.1. Fundamentals of Rubber

Rubber is nowadays extensively applied in industry. The material was first discovered by ancient native tribes in South and Central America. Columbus brought the material to Europe. From the 1930s the implementation abilities increase due to development in bonding technologies between rubber and metal. Elastomers are used because of their excellent sealing and frictional or damping characteristics. On the last-mentioned strength lies the focus for this literature review. The name rubber is often used interchangeable with the term elastomer within the literature. The word rubber is a collective term for vulcanized elastomers, which means that rubber is an elastic polymer (elastomer).

1.1.1. Production process, structure and application

Rubber can be divided into two main categories, natural (NR) and synthetic. To create natural rubber, the sap of the so called "rubber trees" is solidified into thin sheets and is compressed into bales which is the raw material of NR. Rubber is built up by long molecule chains which forms a polymer. The raw material of NR, latex, has no links between the molecule chains which makes it soft and plastic.

Charles Goodyear accidentally found out how he could make natural rubber useful for industry. After adding sulphur to the latex then heating up to a certain temperature eventually seems the crucial factor. This process is called vulcanization. During vulcanization the mixture is heated up to 170 ° C, at which the cross-links (sulphur) connecting the molecular chains (Gil and Jesus, 2006). After the vulcanization process it becomes a soft and highly elastic solid. The final properties of the vulcanized rubber depend mainly of the choice of the rubber, the mixture composition, the production process, and the product design [36].

Synthetic rubber is a manufactured elastomer, made of petroleum products by polymerizing different monomers. Biggest advantage of synthetic elastomers is the capability of fine-tuning the material properties. In comparison to NR, synthetic rubber can better withstand high temperatures, oils and abrasion, but lack in fatigue resistance [53]. This factor is crucial for the use in vibration damping and therefore NR is the first choice in many automotive applications compared to synthetic rubber.

1.1.2. Fillers

In the search of improving NR properties, fillers are now widely used. The filler type that is often used is carbon black (CB). The particles of the CB filler are varying between 20-50 μm in size which form agglomerates within the rubber material. In practice, rubber is often reinforced with filler that has a volume value of 30%. The filler and the elastomer are connected via cross-links and two separate phases emerge in the vulcanized rubber. The rubber phase forms a continuous network, and the filler material lumps inside the rubber network [49]. This makes it a two-phase material made from constituents with completely different mechanical properties [4].

The addition of filler content effects the mechanical properties of the elastomer. Literature shows that the filler has effect on hardness and damping [14, 26], stiffness [15] and temperature [14] or frequency [53] dependence. Nonlinearity becomes more pronounced at filled elastomers which makes them more difficult to characterize. Bokobza [9] shows hyperelastic behaviour for different CB filler contents.

When a more precise control over stiffness is required, the particle size is increased and number is lowered. More on the effects of filler can be found in [14], [26], [30], [36] and [15]. The effect of filler on rubber behaviour is further discussed in the individual upcoming sections.

2

Rubber Behaviour

This section describes theory about the rubber specific behaviour. Both (quasi-)static and dynamic relevant behaviour is discussed. It captures the mechanistic explanation, how the behaviour is triggered and the relevance in terms to this application.

2.1. Incompressible

The bulk modulus B is a material constant which defines its resistance to a change in volume when subjected to as compressed loading condition. Rubber is nearly incompressible, due to the fact that the bulk modulus is usually 1000-2000 times higher than the shear modulus [6]. Equation 2.1 shows the relation between the Poisson's ratio and shear and bulk modulus. It shows that the Poisson's ratio is close to one-half, typically 0.499 [25]. At small strains and therefor limited pressure, the Poisson's ratio can assumed to be constant. When strain values become larger, the Poisson's ratio becomes a function of the strain itself. The incompressibility of CB-filled rubber has been confirmed by different researchers [4] (Bischoff, 2001; Reichert, 1987; Ogden, 1976; Penn, 1970; MacKnight, 1966). Where (Reichert, 1987) shows a limited volume variation of 1% at large strain $\lambda=4$ which confirms the assumption of incompressibility for this application where only a small part of such strain is reached. With increasing enclosure of the rubber geometry, the influence of incompressibility becomes more pronounced [50]. A quick estimation learns us that the enclosed surface of the engine mount is roughly $\frac{1}{6}$. It can be assumed that the effect of incompressibility is not at its largest, but cannot be neglected.

$$\lim_{B/G \rightarrow \infty} \nu = \frac{3B/G - 2}{6B/G + 2} = \frac{1}{2} \quad (2.1)$$

When incompressibility is assumed, the following relation for the principle stretches holds, which will be used later:

$$\lambda_1 \lambda_2 \lambda_3 = 1 \quad (2.2)$$

2.2. Hyperelastic

This section captures the theory of the hyperelastic phenomenon and covers the mechanistic explanation. In this section it must be assumed that the strain is applied (quasi-)static, such that dissipating effects are neglected [15]. This means that the loading process is fully reversible, such that loading and unloading follows the same path and can be described be a single line.

If it comes down to elastic behaviour, rubber behaves significantly different in comparison to metals. Where most metal can be described by Hooke's law within the elastic region, rubber cannot. Rubber has the ability of deforming largely and within this region the stress strain relation is nonlinear. The behaviour is referred to as hyperelastic behaviour and is represented by a s-shaped curve shown in Figure 2.1. Figure 2.1 also shows the hyperelastic behaviour of an elastomer in comparison to the elastic behaviour often assumed for metals.

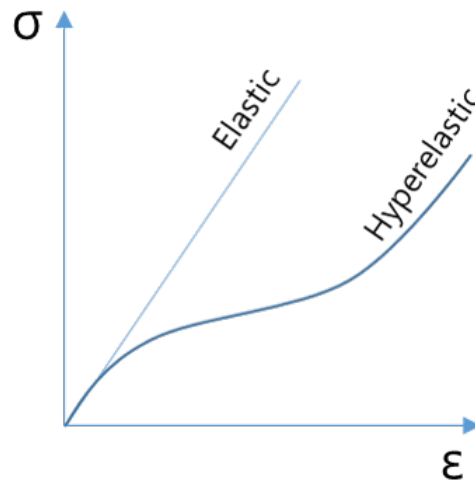


Figure 2.1: Linear Elastic versus Hyperelastic behaviour

The upturn of the S-shaped curve represent a dramatic increase of modulus. At a certain point, the polymer chains will be stretched to the maximum point that the covalent cross links will allow and this cause a dramatic increase in the elastic modulus of the material [34]. Another aspect in the stress-strain relation of elastomer is the significant difference between compression and tension behaviour. This is a result of the high ratio between the bulk and shear modulus, which result in the incompressible behaviour. It causes larger stress in compression compared to tension at the same absolute strain value.

The stiffness is effected by changing the filler content. Ciambella [15] shows the results of the work of Yeoh & Flemming (1997). It is shown that the initial stiffness increases when filler concentration is increased. The initial stiffness is the tangent stiffness in the unloaded configuration. It is therefor expected that when dealing with a highly filled rubber, the S-shaped curve in tension will be tilted in the counter clock wise direction in comparison to a unfilled one. This is also confirmed by the work of Bokobza [9] as shown in Figure 2.2.

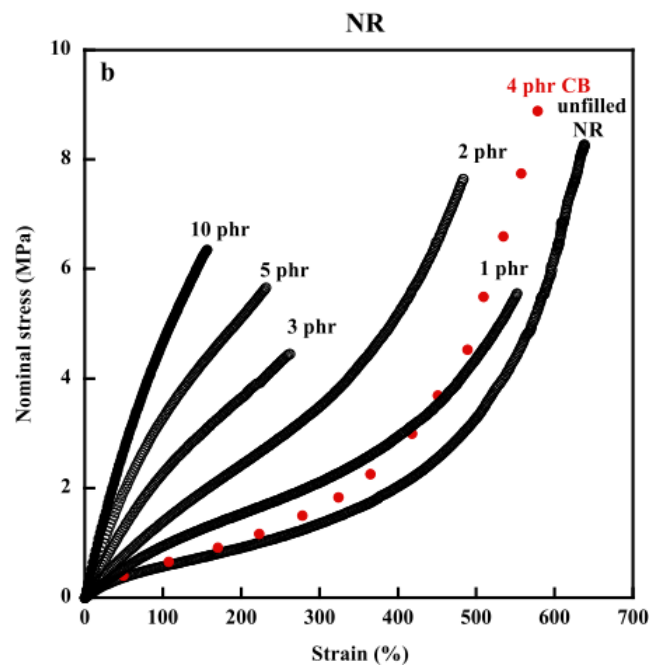


Figure 2.2: Filler effect on Hyperelasticity [9]

Wang et al. [72] researched the effect of the filler network on the dynamic modulus and its hysteresis during the dynamic straining. Results show that the filler network can significantly increase the effective volume of the filler due to the rubber trapped in the agglomerates, leading to high elastic modulus [36].

The S-shaped curve is for most NR observed within a range of multiple 100% of deformation. Because a mount is limited in its motion, such a range is not triggered during this research and it is therefore expected that only a limited section of the stress-strain curve is triggered. This can lead to some simplification in terms of material models which will be discussed in section 3.1.

2.3. Viscoelastic

Up to this section it was assumed that the stress-strain relation can be represented by a single line. For a dynamic analysis this is no longer valid. Rubber materials behave in a viscoelastic manner under dynamic straining. As its name suggests viscoelastic material exhibits both viscous liquid and elastic solid behaviour. Rubber can exhibit all intermediate range of properties between an elastic solid and a viscous liquid. The point at which it acts in between a solid and a liquid is determined by the frequency. Figure 3.1 shows a comparison between viscoelastic behaviour and individual solid and liquid behaviour described by Hooke and Newton respectively. The figure shows the stress reaction to a dynamically applied strain. A linear solid stress reaction is instantaneous whereas a fluid has a 90 degree phase lag. The phase lag of a viscoelastic material such as rubber is determined by the loss angle and varies with the frequency of the applied strain.

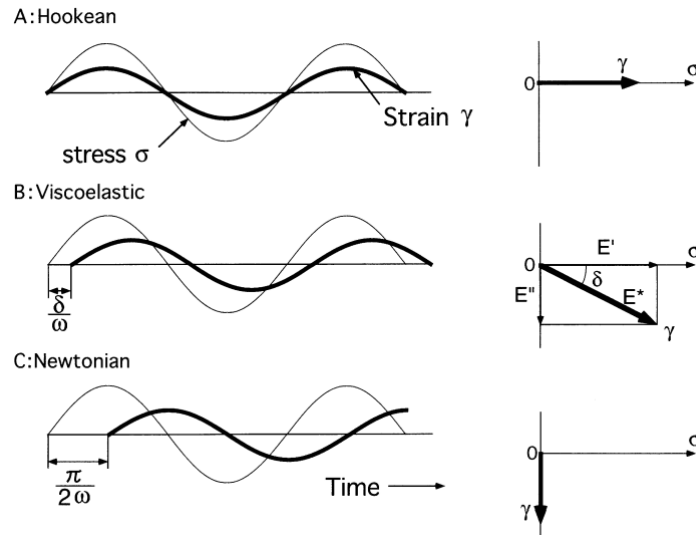


Figure 2.3: Viscoelastic vs. separate viscous and elastic behaviour [45]

2.3.1. Complex Moduli

Linear viscoelastic material behaviour is often characterized in terms of a complex modulus [50]. The complex modulus is used interchangeably with the term dynamic modulus and can be seen as a frequency related characterization of viscoelastic materials. The modulus of interest depends on the expected mode of deformation. Throughout literature complex values are used to define bulk, elastic and shear modulus.

$$B = B' + iB'' \quad (2.3)$$

$$E = E' + iE'' \quad (2.4)$$

$$G = G' + iG'' \quad (2.5)$$

These moduli are used to describe material behaviour under compression, elastic and shear deformation modes respectively. The complex modulus consists of a real part which is referred to as the storage modulus and is seen as the stiffness. The imaginary part represents the loss modulus and is seen as damping. They represent the capability of storing or dissipating energy respectively. The complex modulus can also be expressed in terms of an absolute value and phase angle.

Besides the complex moduli previously mentioned which relate stress to strain, the dynamic stiffness is a modulus often used to describe the viscoelastic behaviour of rubber mounts. The dynamic stiffness relates force to displacement and dependent on both geometry and material properties.

$$K = K' + iK'' \quad (2.6)$$

The dynamic stiffness is a useful measure for experimental characterization of complex geometries. For modelling purpose the interest lies on linking stress to strain. The next section explains bulk, tensile, shear modulus and dynamic stiffness respectively.

The dynamic stiffness of an elastomer that is exposed to a sinusoidal displacement $x_i(t)$ with the corresponding output force $f_0(t)$ can be described as in [3]:

$$\begin{aligned} K^* &= \frac{F_0^*}{X_i} = K' + jK'' \\ &= \frac{F_0}{X_i} \cos \delta + j \frac{F_0}{X_i} \sin \delta \end{aligned} \quad (2.7)$$

The displacement and the output force, respectively, are given by $x_i(t) = X_i \cdot e^{j\omega t}$, $f_0(t) = F_0 \cdot e^{j(\omega t + \delta)}$ and $F_0^* = F_0 \cdot e^{j\omega t}$. X_i is the displacement amplitude, F_0 is the force amplitude and δ is the phase angle between the input displacement and the output force, and ω is the input frequency. The dynamic stiffness K_d is the magnitude of K^*

$$K_d = |K^*| = \sqrt{(K')^2 + (K'')^2} = \frac{F_0}{X_i} \quad (2.8)$$

The loss factor β is used for determining the damping or the hysteresis of the engine mount. It is defined as

$$\beta = \tan \delta = \frac{K''}{K'} \quad (2.9)$$

Bulk modulus

The bulk modulus is a parameter used to describe compressibility and is complementary to shear and tensile moduli. Of this three moduli, the bulk modulus is the least researched due to the experimental complexity [13]. For an isotropic solid, standard elasticity theory can relate bulk modulus directly to the tensile and shear moduli.

$$B = \frac{E}{3(1 - 2\nu)} = \frac{1}{(3G - E)} \quad (2.10)$$

Because the Poisson's ratio of rubber is near 0.5, the relation fails as $1 - 2\nu$ goes to zero. Minor measurement errors of tensile or shear modulus can result in a large error for the calculated bulk modulus. The bulk modulus can therefore not be calculated with results from tensile and shear modulus. Burns and Dumbleday [13] researched the bulk modulus of elastomers and found that the bulk modulus shows little dependence upon chemical composition of the elastomer. Both storage and loss bulk modulus differs from tensile and shear behaviour which are varying widely with chemical composition. Because the precise composition is unknown, this result makes it reasonable to take a general value for the bulk modulus. Storage bulk modulus B' of around 2 GPa is found for NR elastomer type, which is a value also stated by Sandell [59]. Losses are found around 1 or 2% of the average storage bulk modulus B' . The losses for bulk therefore also show significant difference from that at tensile or shear deformation.

Due to incompressible assumption, it can be assumed that dilatation and deviatoric responses can be decoupled. The dilatation response is the response to pressure in all three direction. Kari [32] states that elastic behaviour is present at dilatation and viscoelastic for deviation which is also stated in the work of Burns and Dumbleday [13] which shows that the storage bulk modulus of NR has minor frequency dependence. The fact that the bulk modulus shows no viscoelastic behaviour result is simplifications for the viscoelastic material model later discussed in section 3.2.

Elastic and shear modulus

The elastic and shear moduli are used to describe the response to elongation and shear deformation respectively. The elastic modulus is proportionally to the shear modulus by $E = 3G$. For a filled rubber the factor can become up to 4 [12]. For a reinforced rubber, shear deformation shows less strain dependence than deformation in tension or compression [59]. It can be assumed that the change in behaviour as a function of frequency is equal between the elastic and shear modulus. The expected effect of frequency on the elastic and shear modulus is shown in Figure 2.5 from the work of Höfer and Lion [29]. The general behaviour of rubber within a large audible frequency range is shown in Figure 2.4

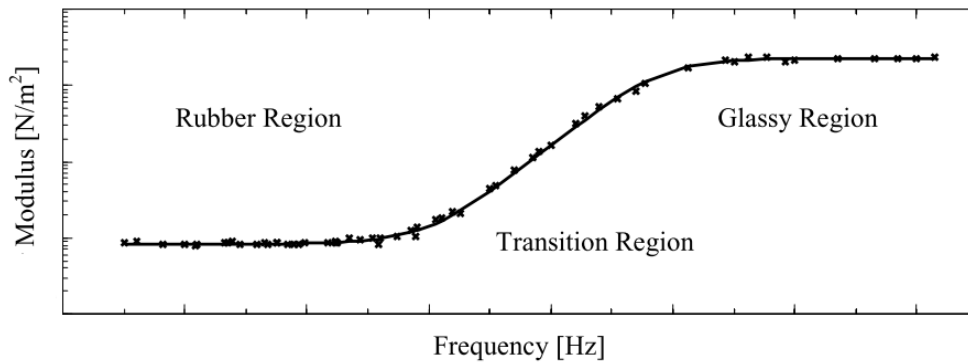
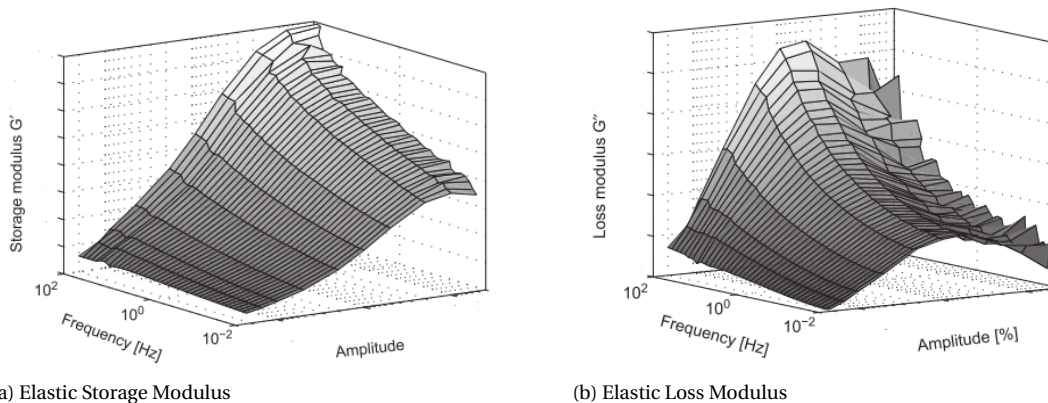


Figure 2.4: Absolute modulus trend-line [16]



(a) Elastic Storage Modulus

(b) Elastic Loss Modulus

Figure 2.5: Effect of frequency and amplitude on the elastic modulus[29]

2.3.2. Dynamic Stiffness

In the search of experimentally characterizing the viscoelastic behaviour of complex geometry the dynamic stiffness shows to be a good measure. It differs from the other moduli in the fact that the stiffness describes a force displacement relation. Multiple research like García Tárrago et al. [24], Laka [36] and Noll et al. [47] is focused on the dynamic stiffness which is geometry and material related. The dynamic stiffness is strongly dependent on the excited frequency and holds both stiffness, damping and inertia properties.

García Tárrago et al. [24] researched the dynamic stiffness of a CB filled rubber bushing in both axial and radial(torsion) direction. It presents a simple engineering design formula including frequency and dynamic strain amplitude dependence. Within a limited frequency range it is able to represent the dynamic stiffness, for a hollow cylindrical bushing. The effect that amplitude and frequency has on the dynamic stiffness shows comparison to the effect it has on shear modulus. This comparison may be an result of the type of loading that is applied during testing.

Richards and Singh [56] found that within a limited frequency range there is a relation between the hardness and dynamic-to-static stiffness ratio. It notes however that a complex geometry can result in a significantly deviation in this trend. It seems reasonable to assume that an engine mount is a complex geometry and

therefor this relation is not a good measure for the dynamic stiffness.

Sjöberg [60] researched the dynamic stiffness for a blocked force and freely oscillating motion. The sample was a simple cylinder of medium CB filled NR. The effect of dynamic strain amplitude on the dynamic stiffness is researched. The magnitude starts decaying towards an asymptotically minimum at large strain. At the point where the decaying of the magnitude starts flattening out, the loss angle shows an optimum. This effect is known as the Payne effect and is also observed by (Jrad,2013) [31]. The author advised to include wave propagation and temperature effect to improve dynamic stiffness prediction. If the designed model is in need of further improvement, the wave propagation is an effect at which will be focused.

Jrad et al. [31] determines the dynamic stiffness trough harmonic dynamic tests (DMA). It experimentally researched the effects that dynamic strain amplitude, preload and frequency has on the dynamic stiffness. Increasing frequency raises both magnitude and phase within the researched frequency range. Results show that the dynamic strain amplitude has significant effect on the dynamic stiffness magnitude. This phenomenon is referred to as the Payne effect. Preload increases the magnitude but has no effect on phase angle. The sample shows softening behaviour with increasing amplitude as well as hardening behaviour with increasing preloads. The softening effect is also presented by García Tárrago et al. [24].

The results of Lee et al. [38] show that for different prestrain values the dynamic-to-static stiffness ratio is constant which implies that the effect of prestrain can be evaluated only on the static stiffness and from there on the dynamic stiffness can be predicted. This technique limits the experimental effort. Results show that the error in the dynamic stiffness prediction increases when the component is loaded in shear.

In summary, García Tárrago et al. [24] presents a simple engineering design formula for a cylindrical bushing. An engine mount is not perfect cylindrical, however it can give a quick first estimation. A relation between hardness and dynamic-to-static stiffness ratio presented by Richards and Singh [56] cannot be assumed due to a complex geometry. If the developed FE model needs improvement, wave propagation is an effect which needs to be considered to take into account as suggested by Sjöberg [60]. Jrad et al. [31] gives a good indication for the expected behaviour under influence of frequency, prestrain and dynamic strain amplitude. In terms of experimental characterization of the preload effect, Lee et al. [38] found that the dynamic-to-static stiffness ratio is constant for different levels of prestrain. If the effect of preload is needed to be considered this relation limits experimental effort significantly.

2.3.3. Energy Dissipation

The (quasi-)static material parameters that describe hyperelasticity are used to find long term solutions. In order to determine a frequency dependent solution, the damping of a material plays a significant roll. Damping is included in the viscoelastic material properties. Yu et al. [75] explains that rubber characteristics for use in an engine mount is always a compromise. Lighter damping is desirable for a low transmissibility at high frequencies and high damping is required to minimize engine movement and absorb engine shake. Lower frequency often lead to larger amplitude of excitation whereas higher frequencies lead to smaller vibration amplitude. In engine mount related research therefor the focus has been on finding and manipulating frequency dependent behaviour.

Throughout literature different terminology is used such as damping, hysteresis, loss angle, loss factor and loss modulus. They all refer to one physical phenomenon which is an energy loss due to dissipation within the material. Damping is a collective term used when talking about energy dissipation, but is not a measure of the phenomenon. Different measures for damping are given by;

$$\text{loss modulus} = E'' \quad (2.11)$$

$$\text{loss angle} = \delta \quad (2.12)$$

$$\text{loss factor} = \tan \delta = \frac{E''}{E'} \quad (2.13)$$

Laka [36] presents relations between all of these different terminology. Again all forms of damping are dependent on dynamic strain amplitude [24], frequency [24, 74] and temperature. The degree of dependence is determined by the composition of the material.

When rubber is subjected to a sinusoidal varying strain, the stress will also react in a sinusoidal way, assuming linear viscoelastic behaviour. In rubber there is a time delay in the stress reaction to the excited strain. This

time delay is a consequence of the present damping and can be represented by a phase shift/angle as can be seen in Figure 2.6.

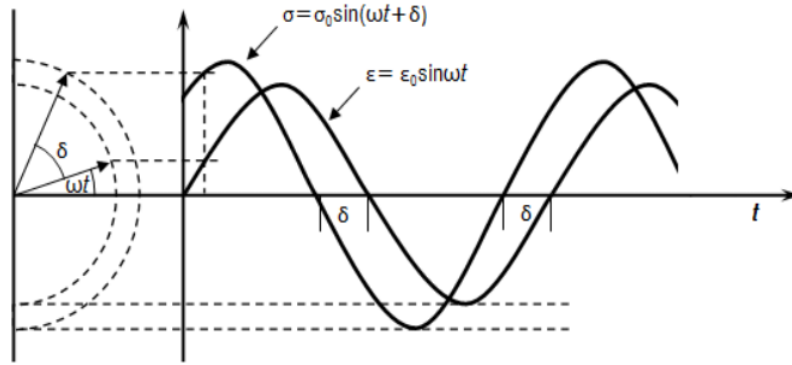


Figure 2.6: Phase shift in viscoelastic reactive behaviour of rubber[36]

Instead of plotting results to time, the damping can be represented by a stress-strain plot as shown in Figure 2.7a. For a linear viscoelastic material the hysteresis is presented as a perfect ellipse. The ellipse is associated with the dissipated energy U_c during one loading cycle and can be calculated with Equation 2.14. The surface of the ellipse represent the energy the sample can hold. Integrating over one quarter of the ellipse gives the maximum stored elastic energy W_c which can be seen from Equation 2.16.

$$U_c = \pi \sigma_0 \varepsilon_0 \sin \delta \quad (2.14)$$

$$\begin{aligned} U_c &= \frac{\omega \varepsilon_0^2}{2} E'' \frac{2\pi}{\omega} \\ &= \pi E'' \varepsilon_0^2 \end{aligned} \quad (2.15)$$

$$\begin{aligned} W_c &= \frac{1}{2} E' \varepsilon_0^2 \\ &= \frac{1}{2} \sigma_0 \varepsilon_0 \cos \delta \end{aligned} \quad (2.16)$$

In practice elastomers behave nonlinear and therefore the hysteresis is not a perfectly ellipse. Österlöf [53], Dorfmann and Ogden [21] and Sandell [59] show that for CB filled elastomers the hysteresis does not show a perfect elliptical shape. This can be explained by the fact that a perfect ellipse represents a constant modulus with damping. A perfect ellipse represents a linear viscoelastic material and if a nonlinear viscoelastic material such as a highly filled NR is considered, the dynamic strain amplitude effect is taken into account. In such a case both storage and damping modulus are not constant. Equation 2.16 shows the relation between stored energy and the storage modulus. More theory about the hysteresis in elastomers can be found in the work of Moore and Geyer [43].

For viscoelastic materials, the hysteresis is attributed the phase angle δ as $d = \sin \delta$.

$$d = \frac{U_c}{\pi \sigma_0 \varepsilon_0} \quad (2.17)$$

Luo et al. [40] derived an equation to calculate the hysteresis loss as function of strain amplitude and frequency. Within the limited frequency range researched, both test result and predictions of the hysteresis shows limited dependence on the frequency. The hysteresis loss shows significant dependence on the dynamic strain amplitude and also filler content. Chazeau et al. [14] concluded that an unfilled elastomer exhibit linear viscoelastic behaviour for shear strain excitation up to 20%, while results for CB filled elastomer shows nonlinear viscoelastic behaviour at shear strain as low as 0.5%. The deviation of the hysteresis in unfilled rubber is often quite small and can be neglected. The filler network has the property that it is not stable

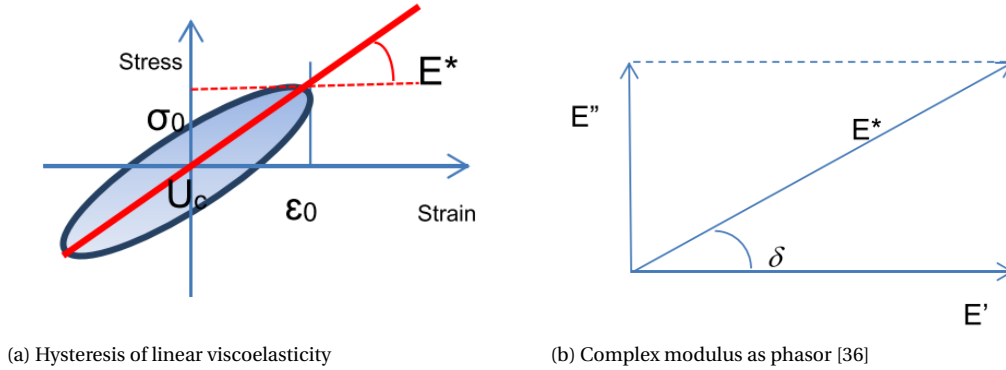


Figure 2.7: Elastic modulus representation

and breaks up into smaller units when increasing mechanical strain [30]. When subjected to cyclic straining, a stable filler network can reduce the hysteresis of the filled rubber, where the breakdown and reformation of the filler network would cause an additional energy dissipation resulting in the higher hysteresis.

The straight line in Figure 2.7a represents the magnitude of the complex modulus E_{dyn} also shown by the phasor diagram as E^* in Figure 2.7b. The imaginary part of the complex modulus, in whatever form, represent the loss modulus. If literature talks about the complex modulus, than loss angle, loss factor and loss modulus are all measures to describe material damping. The complex modulus is defined by Equation 2.18.

$$E^* = \frac{\sigma_0}{\epsilon_0} e^{i\delta} = E' + iE'' \quad (2.18)$$

$$\tan \delta = \frac{E''}{E'} \quad (2.19)$$

In summary there are multiple measures of damping in elastomers. Depending on the interest of the researcher different terminology is used. The time plots are useful when interested in stress reactions over a certain time period. Because the focus lies on frequency related results the time plot is not useful. The stress-strain plot is a intuitive way of representing damping and can also show amplitude dependence. The plot however lacks the ability to represent the dependence on frequency because the plot becomes occupied with numerous different data samples. In this research the complex moduli is the optimal method to present damping for example as function of frequency or amplitude.

2.4. Stiffness effects

In this section different phenomena are reviewed that are known to affect the stiffness of rubber. The phenomena are:

- Prestrain,
- Payne and
- Mullins effect

Two well-known amplitude effects occurring in filled vulcanized rubber material are the Mullin's and the Payne effect. This section goes into further detail on these two softening phenomena and a conclusion is drawn in terms of relevance for research. The Payne effect is triggered by the dynamic strain amplitude whereas the Mullins' effect is related to the deformation history.

2.4.1. Prestrain effect

A certain level of prestrain is present at all engine mounts. During the manufacturing process the rubber geometry is often compressed inside the outer metal shell, which introduces the first prestrain. A second source of prestrain is the mounted vibration source which is often a significant weight. This induces a second

deformation. In this research the term prestrain is used as a collective term for more specific terms like precompression and pretension. The first prestrain will be a compression, whereas the second can result in tension, compression or strain deformation. This will depend on the orientation of the mount relative to the loading direction. In this section a selection of experimental results from other researchers are reviewed. The results are being analyzed with a focus on the level of prestrain, filler content and frequency range. This will result in an expectation sketch for the effect of prestrain.

For this research, the practical situation can be described as a relatively large initial deformation superimposed with small oscillatory displacement. Research of (Kim, 2004) [35], (Wollscheid, 2013) [74] and (Suphadon,2010) [63] is focused on this type of loading conditions. Research done by (Kim, 2004) [35], (Wollscheid, 2013) [74], (Suphadon,2010) [63], (Lee,2001) [37] and (Jrad,2013) [31] experimentally proves that the complex moduli shows dependence on the prestrain level. This section clarifies the experimental results from the aforementioned research, which will result in assumptions and used for this research.

Lee and Kim [37] researched the effect of precompression for a 46% CB filled NR. It used an shape-factor to compensate for the effect of deformation. An increase is shown for both moduli at all levels of pretension as a function of frequency. The loss modulus increases in a somewhat linear manner and the storage modulus increases significantly at low frequencies after decaying towards higher frequencies. The results imply that the storage modulus reaches an asymptotically value at high frequency. The normalized storage modulus from (Lee,2001) [37] for a NR with 46% CB compares well with the results found by (Kim,2004) [35] for the 50% CB filled NR.

The focus of previous research like that of (Kim, 2004) [35] lies on finding the effect of precompression on the complex elastic modulus. Figure 2.8 shows the for zero prestrain, normalized storage modulus for NR with different levels of CB filler. When dealing with an unfilled rubber, the dependence on precompression can be assumed to behave in a linear manner. With increasing filler content, the dependence becomes more non-linear. The author draws the careful conclusion that the effect prestrain has on the complex tensile modulus is somewhat proportional to the filler content. In this paper it is suggested that the separability assumption is only applicable to unfilled rubber. For filled rubber, the static precompression has an effect on its time dependent properties and therefore should be taken into account.

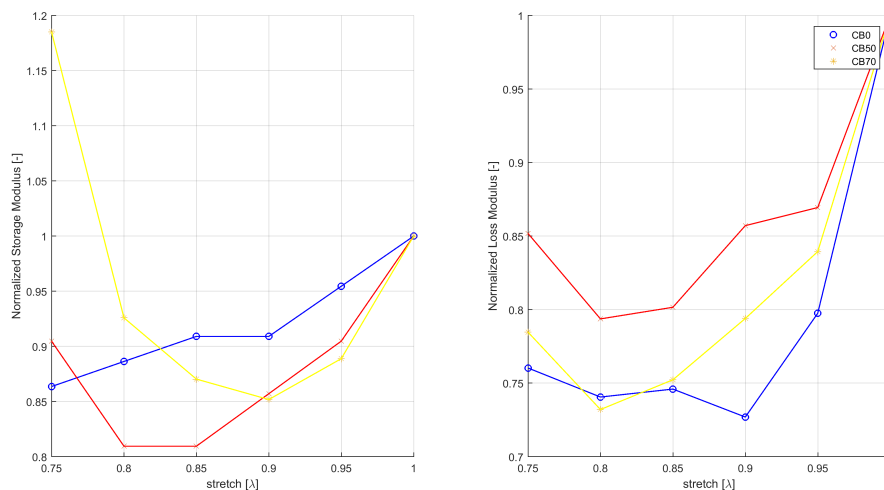


Figure 2.8: Normalized effect of prestrain for different levels of filler [35]

The work of (Suphadon,2009 and 2010) [62, 63] researched the effect of static extension on the shear loss modulus when superimposed with small torsional oscillations. It shows that for unfilled NR the static prestrain has no significant effect on the loss modulus up to a strain of 200%. It is concluded that up to this strain level, the effect is a consequence of geometric changing of the sample and not of the applied strain. It is concluded that the viscoelastic properties are not affected due to prestrain. The results [62] are confirmed in its work of 2010 [63].

Wollscheid and Lion [74] researched also the prestrain effect on complex tensile modulus, but obtained more broader results than that of Kim et al. [35]. A larger range of both prestrain and frequency is investigated for one CB filled rubber. Results show the effect of predeformation (λ ranging from 0.8 to 1.4) on the complex modulus up to a frequency of 500 kHz. Both storage and loss modulus show decreasing behaviour with increasing λ . As a function of frequency both moduli show the some nonlinear upwards trend that seems independent of prestrain level. Looking at these results, a correction factor can be an interesting method to adjust frequency dependent tensile modulus for different prestrain levels. Such a method is also presented by (Lee,2001) [37]. It adjusts the Morman's formula by implementing a strain-dependence to the relaxation function. A pre-strain dependence is used at a reference frequency.

As previously mentioned the amount of filler content is largely responsible for the decision of neglecting prestrain effects. An extreme case is researched by Thorin et al. [64] and gives an indication for upper limits because it investigates highly filled rubber. Results show that up to 1% of prestrain both storage and loss modulus are relatively constant. From 1% up both moduli start increasing exponential.

The aforementioned results suggest that a shift factor can account for the prestrain effect on the frequency dependent storage modulus of filled rubber. Static experiments described in section 4.1 can be used for determining the shift factor. The frequency dependent complex moduli can be determined by dynamic experiment at zero prestrain. If this method is applicable, experimental effort is significantly reduced because prestrain is not a parameter that has to be varied within the dynamic experiments.

2.4.2. Payne effect

Besides the static prestrain dependence as described in section 2.4.1, rubber behaviour changes under the influence of the dynamic strain amplitude. The dynamic strain amplitude, later referred as strain amplitude, is the amplitude of a vibration when a rubber geometry is harmonically excited. The Payne effect [54] is sometimes referred to as the Fletcher-Gent effect (Fletcher & Gent, 1953). The Payne effect describes the effect dynamic strain amplitude has on the complex moduli of interest. When talking about the Payne effect, the scope lies outside the linear viscoelastic region where no amplitude effect is taken into account. The dependency becomes more pronounced with increased amount of filler [23, 74]. For unfilled rubber the Payne effect is not present and this can be assumed for certain filled rubber types as well. The strain amplitude range at which this is valid depends on the composition of the elastomer [74]. Wollscheid and Lion [74] shows that for a 20 PHR (part per hundred rubber) the Payne effect can be ignored within a dynamic strain ranging from $10^{-2}\%$ to $10^1\%$. In this region the elastic storage and loss modulus shows almost constant behaviour. The effect on the absolute and loss shear modulus for a harmonically loaded rubber is illustrated in Figure 2.9. The storage modulus decreases with increasing amplitude and the damping d /loss factor shows a maximum at moderate strain amplitude [29, 50]. A result which is also found by Sjöberg [60], Österlöf [53] and Karlsson and Persson [33].

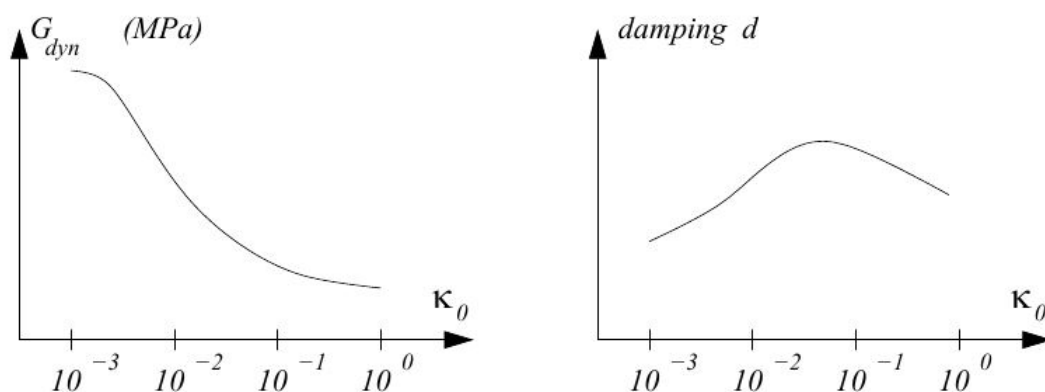


Figure 2.9: Shear modulus as a function of strain [50]

At small deformations, the storage modulus is higher because the carbon-black agglomerates, which are the “hardest” regions, are not broken. As the deformation is increased, the agglomerates are broken into smaller agglomerates. Therefore, the storage modulus decreases because there are now more mobile units or “soft”

regions in the rubber matrix. At large deformations, the CB agglomerates break down until the aggregates themselves are mobile units. The agglomerates present at intermediate amplitudes may be identified with the “hard” regions. The breaking of the structure is often described as a frictional behaviour, which is an energy dissipation mechanism. Hence, the loss factor of the elastomer increases, as shown by (Medalia,1978).

In this research the focus lies on high frequency excitations that are characterized by their very low strain amplitude. The amplitude of an operating engine is very small in the high frequency region. The stiffness of engine mounts can therefore be considered as independent of amplitude in the audio frequency range [46]. The result of [74] show that it seems reasonable that the Payne effect can be neglected because the expected dynamic strain amplitude are of such a low value. Pitfall is that the rubber of interest may contain a higher level of CB-filler which will lower the dynamic strain amplitude until which the Payne effect can be neglected. During experimental characterization the applied displacement can be controlled and verified by measurements.

2.4.3. Mullins effect

The Mullins effect is about the stress-softening that is produced when an elastomer is harmonically deformed for the first few time as presented in Figure 2.10. In literature it is sometimes identified as damage and is common to all rubbers [36]. It is seen as damage because the Mullins effect does not recover at a fixed temperature. The Mullins effect (Mullins, 1947) is a viscoelastic effect and results in a significant reduction in the stress at a given level of strain during the unloading path as compared with the stress on initial loading in stress-strain cyclic tests [21]. The difference is a result of residual strain after deformation. In filled rubber this is due to the mechanical hysteresis from filler particles debonding from each other or from the polymer chains caused by the stretching [15]. Therefore highly reinforced elastomers suffer a more pronounced stiffness reduction than those with low filler content. After a few loading cycles the internal microstructure reaches a permanent state and changes in stiffness become no more significant.

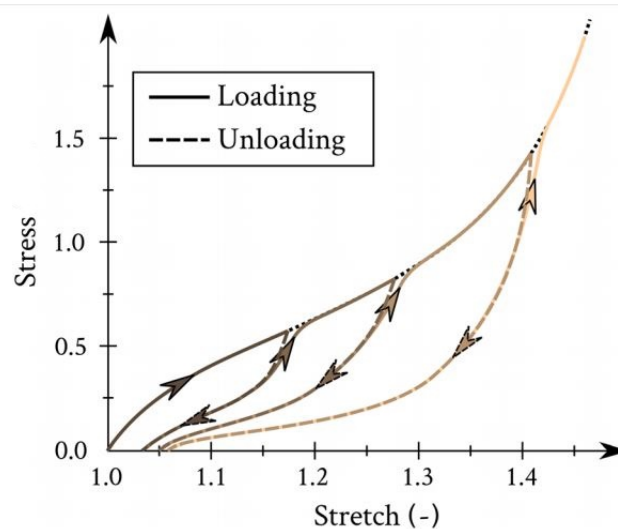


Figure 2.10: Representation of Mullins effect [19]

Different mechanistic explanations for the Mullins effect are given in literature. A few are covalent bond rupture, molecules slipping, filler rupture and disentanglement as shown in Figure 2.11. For a more extensive overview and mechanistic explanation the reader is referred to the work of Diani et al. [20].

The Mullins effect is the instantaneous and irreversible softening of the stress–strain curve that occurs whenever the load increases beyond its prior all-time maximum value. The irreversibility holds when a fixed temperature is held.

For this research it can be assumed that the rubber is already been excited with a larger amplitude than the region of interest. This is valid because during driving manoeuvres the rubber is loaded at a significantly higher level than during steady state highway conditions. The samples used for the experiment can be preconditioned beyond the level of interest to exclude the Mullins effect from measurements. More about preconditioning

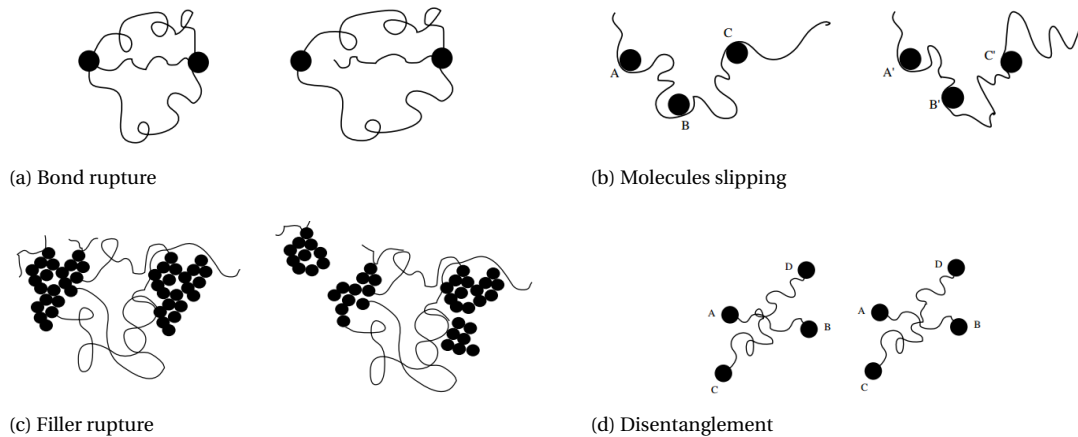


Figure 2.11: Physical explanation of the Mullins effect

tioning to exclude Mullins effect can be found in research of Dorfmann and Ogden [21]. It is also assumed that the temperature will not reach the level at which recovery of the previously broken bounds takes place and therefor also the material stiffness. Because of these facts, the Mullins effect does not have to be taken into account for correctly modelling the dynamic behaviour that is done in chapter 3.2.

2.5. Conclusion on rubber behaviour

In this section the previously mentioned effects are considered in terms of the application. The incompressible, hyperelastic and viscoelastic behaviour are treated in this chapter. Apart from this general behaviour there are specific rubber softening effects mentioned which are the Mullins and Payne effect. The effect of prestrain is also introduced in this chapter. Concluding on the previous results the following can be assumed:

- Incompressible
 - Bulk modulus not a function of frequency
- Hyperelastic
 - Limited region triggered
 - Material model simplifications
- Viscoelastic
 - Moduli show severe frequency dependence
 - Small dynamic strain amplitude and therefor linear viscoelastic behaviour
- Experiment considerations
 - Control displacement to prevent the Payne effect from occurring
 - Precondition sample to prevent the Mullins effect from being observed
- Filler
 - Filler content not provided by the manufacturer which leads to uncertainty. General effect are known and will be taken into account during analysis.

3

Modelling Rubber Behaviour

In the previously section the relevant rubber behaviour is discussed. The behaviour of the aforementioned relevant behaviour needs to be modelled. This section explores different methods for modelling this rubber behaviour. A selection of applicable methods are reviewed which will give a guideline when modelling rubber within a FE software.

In section 3.1 it is explained how the static stress strain relation is represented. The five most applied hyperelastic material models are reviewed. In section 3.2 different models are reviewed that could represent the viscoelastic behaviour with a small expansion in terms of modelling nonlinear viscoelastic behaviour. The following hyperelastic and viscoelastic material models are discussed:

Hyperelastic

- Yeoh
- Neo-Hooke (NH)
- Mooney-Rivlin (MR)
- Arruda-Boyce (AB)
- Ogden

Viscoelastic

- Maxwell
- Kelvin-Voigt
- Zener
- Generalized Maxwell
- Fractional Derivative

3.1. Hyperelastic Material Models

The hyperelastic behaviour as described in section 2.2 needs to be modelled. For a (quasi-)static analysis the elastic behaviour of an elastomer is sufficiently described by a hyperelastic material model. To model the hyperelastic behaviour of rubber a relation between stress and strain needs to be determined which is called a constitutive relation. The surface under the S-shaped stress-strain curve described by a strain energy density (SED) function W . The derivative of the SED function with respect to the strain results in the corresponding stress.

$$\sigma_{ij} = \frac{\partial W}{\partial \varepsilon_{ij}} \quad (3.1)$$

The SED function can be used within the FE software Abaqus, where a wide variety of hyperelastic material models are available. This section makes no attempt in explaining the derivation of SED function. The SED function W can be based on the principle stretches or the strain invariants, whereas the last mentioned is the most applied one. It is usually based on the first, and sometimes second strain invariant.

$$W = W(F) = W(\lambda_1, \lambda_2, \lambda_3) = W(I_1, I_2, I_3) \quad (3.2)$$

where $\lambda_1, \lambda_2, \lambda_3$ are principal stretches and I_1, I_2, I_3 are the invariants of the left Cauchy-Green strain tensor

For a hyperelastic, isotropic and incompressible material, the Cauchy stress tensor σ_{ij} , is given by:

$$\sigma = 2 \left[\left(\frac{\partial W}{\partial I_1} + I_1 \frac{\partial W}{\partial I_2} \right) \mathbf{B} - \frac{\partial W}{\partial I_2} \mathbf{B}^2 \right] + p \mathbf{I} \quad (3.3)$$

where p is an undetermined reaction stress which enforces the incompressibility constraint. Only the deviatoric stress causes strain when an incompressible body is considered [36]. The deviatoric stress can be written as:

$$\begin{aligned} s &= \sigma - p\mathbf{I} \\ &= 2 \left[\left(\frac{\partial W}{\partial I_1} + I_1 \frac{\partial W}{\partial I_2} \right) \mathbf{B} - \frac{\partial W}{\partial I_2} \mathbf{B}^2 \right] \end{aligned} \quad (3.4)$$

The strain invariants I_1, I_2, I_3 of the left Cauchy-Green strain tensor, B , can be obtained respectively as:

$$\begin{aligned} I_1 &= \text{trace}(\mathbf{B}) &= \lambda_1^2 + \lambda_2^2 + \lambda_3^2 \\ I_2 &= \frac{1}{2}(I_1^2 - \mathbf{B} \cdot \mathbf{B}) &= \lambda_1^2 \lambda_2^2 + \lambda_1^2 \lambda_3^2 + \lambda_2^2 \lambda_3^2 \\ I_3 &= \det(\mathbf{B}) &= \lambda_1^2 \lambda_2^2 \lambda_3^2 = 1 \end{aligned} \quad (3.5)$$

As shown by the work of Baaser et al. [5] some simplifications can be applied due to incompressibility conditions. Assuming a constant volume leads to: $J = \det \mathbf{F} = 1$ which result in the relation $\lambda_3 = \frac{1}{\lambda_1 \lambda_2}$. With these results the first and second strain invariant can be written as a function of the first and second principle stretch.

$$\begin{aligned} I_1 &= \lambda_1^2 + \lambda_2^2 + \frac{1}{\lambda_1^2 \lambda_2^2} \\ I_2 &= \lambda_1^2 \lambda_2^2 + \frac{1}{\lambda_1^2} + \frac{1}{\lambda_2^2} \end{aligned} \quad (3.6)$$

The goal is to review the most applied hyperelastic models which are expected to be applicable for this research. The hyperelastic models reviewed in this section are the

- Yeoh,
- Neo-Hooke (NH),
- Mooney-Rivlin (MR),
- Arruda-Boyce (AB) and
- Ogden model

The performance of these models under uniaxial tension is presented in Figure 3.1. More about these models being evaluated for automotive purposes can be found in the work of Tobajas et al. [65]. More about the parameter characterization for the MR, Ogden and AB model with uni- and bi-axial tests can be found in [2]. Ogden et al. [48] goes further into detail on the model fitting to experimental data. Other material data extraction is described by Sandell [59]. For an extensive list of different SED functions the reader is referred to the work of Bortoli et al. [10].

The reviewed models are based on a phenomenological, mechanistic or a combined (hybrid) approach. The most hyperelastic models are phenomenological for which the constants have no direct physical meaning [10]. Material models based on this approach fit a polynomial to experimental results from one or more deformation modes and describe the observed behaviour. The mechanistic approach is about modelling the behaviour with arguments about underlying material structure. A hyperelastic material is also sensitive to deformation states. The material model chosen to evaluate, need to behave physically realistic in other deformation modes than the ones experimentally tested. With the expansion of more sophisticated hyperelastic models, data from different deformation modes must be available. Commonly used deformation modes are uniaxial, biaxial and planar tension. More on these experiment can be found in section 4.1. The number of parameters of the model needs be limited in order to limit experimental effort. The material model needs to be able to fit a limited predefined range of the complete s-shape stress-strain curve. This section describes the most used hyperelastic material models for incompressible materials.

The NH and Yeoh model are the most well known and depend only on the first strain invariant and these models can be seen as special cases of the Ogden model. The NH and Yeoh models will often yield in a physically correct behaviour in all direction, as long as they are correctly fitted for one direction [50]. This gives the models a broad application area with limited experimental effort. If only one deformation mode is available, it is advised to stick to the NH, Gent or AB model. Yeoh found that for CB filled NR the dependence

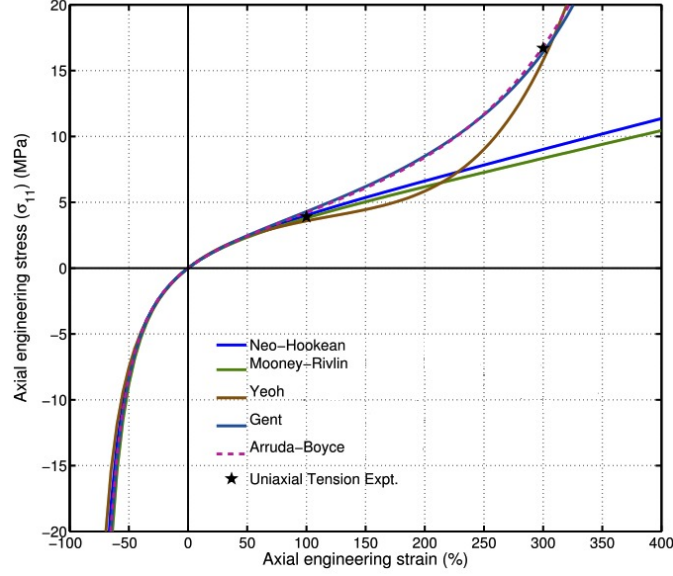


Figure 3.1: Material model comparison for uniaxial tension

on the second invariant I_2 was weak and therefore simplified the MR model. For the Yeoh model caution needs to be taken when deformation takes place at low strain levels (Yeoh, 1995).

Yeoh

$$W = C_{10}(I_1 - 3) + C_{20}(I_1 - 3)^2 + C_{30}(I_1 - 3)^3 \quad (3.7)$$

Neo-Hooke

$$W = C_{10} \cdot (\bar{I}_1 - 3) \quad (3.8)$$

The NH model describes the behaviour of materials that will undergo large deformations. It is a special form of a MR solid, where $C_{01} = 0$. The model is accurate for strain values less than 20% and the shear modulus is assumed to behave constant.

The MR model shows good agreement with tensile test data up to 100% strain, however it has been found inadequate in predicting behaviour in other modes of deformation than the one fitted to. The MR model is not sufficient for multidimensional analysis. Using it for multidimensional analysis results in more experimental effort.

Mooney-Rivlin

This is a special case of the generalized Rivlin model and is a linear combination of the invariants of the left Cauchy-Green deformation tensor B . The original Mooney model is:

$$W = C_{10} \cdot (I_1 - 3) + C_{01} \cdot (I_2 - 3) \quad (3.9)$$

which is often used for unfilled NR [59]. Parameters can be checked with a rule of thumb: $C_{01} = \frac{1}{10} C_{10}$ or $\frac{1}{4} C_{10}$. Numerous models have been developed over the years, but they all can be generalized to a 5th order polynomial strain energy function family.

$$W = \sum_{i=1}^5 \sum_{j=1}^5 C_{ij} (I_1 - 3)^i (I_2 - 3)^j \quad (3.10)$$

which is known as the Mooney-Rivlin model. This family account for non-constant shear modulus. Inclusion of higher order terms can lead to an unstable energy function which yields non-physical results outside the range of the experimental data. In general this model is assumed to be valid up to 100% strain. In the case of CB filled elastomers, only a small range of strain can be fitted as shown by Laka [36].

Tshoegl's [66] (Tshoegl, 1971) research shows that retention of the higher order terms in the generalized RV material model led to a better agreement with test data for both unfilled and filled rubbers.

Arruda-Boyce

The AB is a micro-mechanical model. Such models represents the physics of network deformation. The AB model claims to correct the disability of the MR model and results in a material model that is accurate for multiple modes of deformation at all strain levels, with making use of only uniaxial test data. The AB model as function of first strain invariant is described as:

$$W = C_1 \Theta \left[\frac{1}{2} (I_1 - 3) + \frac{1}{20N} (I_1^2 - 9) + \frac{11}{1050N^2} (I_1^3 - 27) + \frac{19}{7000N^3} (I_1^4 - 81) + \frac{519}{673750N^4} (I_1^5 - 243) \right] \quad (3.11)$$

where $C_1 = k \cdot \Theta$ is a material constant where k is the Boltzmann constant, Θ the temperature and N the number of statistical links of length 1 in the chain between chemical crosslinks.

Ogden Model

The Ogden model differs in the fact that it uses the principle stretches. The use of real powers rather than integer powers makes it able to capture the "upturn" at large strain and is therefor used for large strain analysis. The parameter μ and α are hard to determine because iterative methods must be used instead of simple least square methods [28]. It has not the ability to be used with limited test data.

$$W(\lambda_1, \lambda_2) = \sum_{p=1}^N \frac{\mu_p}{\alpha_p} (\lambda_1^{\alpha_p} + \lambda_2^{\alpha_p} + \lambda_1^{-\alpha_p} \lambda_2^{-\alpha_p} - 3) \quad (3.12)$$

Where in general the shear modulus results from $2\mu = \sum_{p=1}^N \mu_p \alpha_p$

As can be seen in figure 3.1, not all hyperelastic material models are capable of capturing the so called upturn in the S-curve. Due to limited motion inside the engine mount only a limited region of the curve is expected to be triggered during this analysis. For the models to be evaluated it is therefor not critical if they are not able to capture this upturn.

Unfilled rubber can be modelled as an elastic which can be very beneficial and provide quite good results [49]. Predicting the behaviour of filled rubber is complex because it strongly depends on strain amplitude and temperature, but has weak frequency dependence [53]. A more exact stress strain relation adds more complexity to the model [26].

3.2. Viscoelastic Material Models

The frequency dependent behaviour is captured within a viscoelastic model and needs modelling as well. Throughout literature linear viscoelastic behaviour is characterized by different models. In this section the most applied viscoelastic models are reviewed in terms of their performance, complexity and numerical implementation. The performance is determined by the ability to represent previously observed viscoelastic behaviour. Results from the work of Voormeeren [70] are use to compare with. The considered viscoelastic models are all linear, meaning that they do not account for amplitude dependence [26]. Increasing the amount of filler will increase the amplitude dependence and therefore the viscoelastic models can only characterize accurately lightly filled rubbers with negligible amplitude dependent characteristics. With the knowledge of this section a preselection can be made in terms of models that are examined during this research.

It is known that the viscoelasticity holds both elastic and viscous behaviour. The elastic and viscous behaviour is often represented by making use of springs and viscous dash-pots respectively. Examples of such rheological models from simple to more complex are the;

- Maxwell model
- Kelvin-Voigt model (KV model)
- Standard linear solid model (Zener) (SLS model)
- Generalized Maxwell model (GMM)

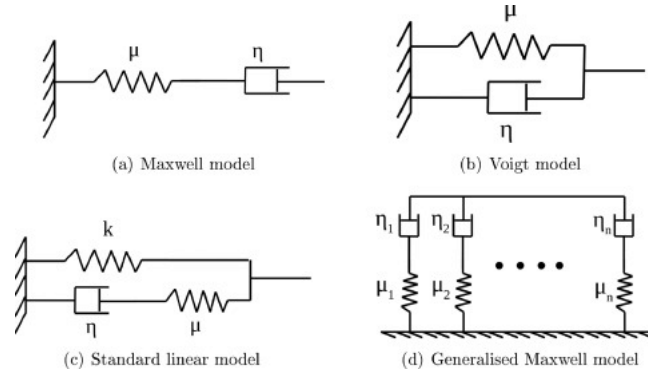


Figure 3.2: Viscoelastic rheological models [44]

The aforementioned models are schematically presented in Figure 3.2.

The Maxwell and Voigt model both use the same elements and are connected in series or parallel respectively as can be seen in Figure 3.2. From the differential equation of the rheological models the complex modulus in the frequency domain can be determined. The complex modulus of the Maxwell model is:

$$\eta \frac{d\sigma(t)}{dt} + E\sigma(t) = \eta E \frac{d\varepsilon(t)}{dt} \quad (3.13)$$

$$E_m^*(\omega) = \frac{E\eta^2\omega^2 + E^2\eta\omega i}{E^2 + \omega^2\eta^2} \quad (3.14)$$

and the complex modulus of the KV model is presented by:

$$\sigma(t) = E\varepsilon(t) + \eta \frac{d\varepsilon(t)}{dt} \quad (3.15)$$

$$E_{kv}^*(\omega) = E + \eta\omega i \quad (3.16)$$

Figure 3.3 shows the normalized complex moduli as a function of frequency. The storage and loss modulus and dynamic stiffness is shown. The storage modulus is about the recovery of energy and the loss modulus about the dissipation of energy. The lines represent different dashpot values.

The Maxwell model yield no physically realistic behaviour in the case of (quasi-)static deformation because the elongation of the dashpot is not limited and therefor the model will behave as a viscous. At low frequency the recovered energy is unrealistic low as can be seen from the storage modulus in Figure 3.3. For the storage modulus of the Maxwell model, the dashpot value determines in which frequency range an asymptotically value is reached. The asymptotic value is determined by the spring value as can be seen from Equation 3.17. The loss modulus has an maximum at intermediate frequency after which it decays to an asymptotic value determined by the dashpot value.

$$\begin{aligned} \lim_{\omega \rightarrow \infty} \text{re}[E_m^*(\omega)] &= E \\ \lim_{\omega \rightarrow \infty} \text{im}[E_m^*(\omega)] &= 0 \end{aligned} \quad (3.17)$$

At higher frequencies, this model recovers more energy than at low frequency. In general this is a behaviour observed for filled NR, like the results of Voormeeren et al. [71] in Figure 3.4.

The disadvantage of the Maxwell model, in term of nonphysical behaviour at low frequency, is solved for the KV model. In the KV model a viscous dashpot is coupled in parallel to an elastic frequency independent spring. The elongation of the damper is now limited by the spring in parallel. At low frequencies the KV model will now behave as a solid instead of a viscous. The storage modulus of the KV model is constant which is realistic only for a small frequency range. The loss modulus is linear which is not a behaviour observed by the work of Voormeeren [70]. The KV model is characterized by the facts that at higher frequencies it overestimates and at the lowest frequencies it will underestimate the loss factor of the dynamic stiffness [61]. This result is confirmed by Figure 3.3 and limits of the KV model are given by Equation 3.18. The loss modulus

is not bounded which result in unrealistic behaviour at high frequency. Because in this research the frequency range is rather large, this will result in a large error.

$$\begin{aligned} \lim_{\omega \rightarrow \infty} \operatorname{re}[E_{kv}^*(\omega)] &= E \\ \lim_{\omega \rightarrow \infty} \operatorname{im}[E_{kv}^*(\omega)] &= \infty \end{aligned} \tag{3.18}$$

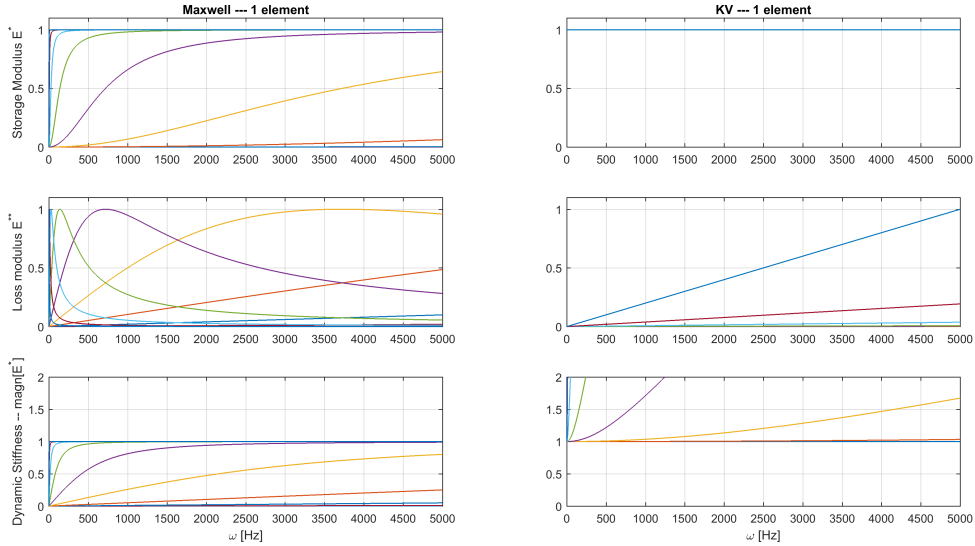


Figure 3.3: Normalized Maxwell and KV model

In general the Maxwell model yield more physical behaviour than the KV model. Both models have pros and cons and are not yet sufficient to characterize the dynamic behaviour of (filled) NR. The Maxwell model has the most potential and therefor improved in different ways. To create an improved storage modulus at low frequency a spring is added in parallel with the Maxwell model, making it a SLS model. The added static stiffness makes it behave as a solid at low frequencies. Withing the FE software Abaqus the static stiffness is determined by the hyperelastic model previously mentioned. The SLS model is also referred to as the Zener and three parameter Maxwell model. In the search of improving experimental fitting capabilities, the Maxwell model is improved in to the Generalized Maxwell Model (GMM). Both SLS and GMM models are reviewed in to upcoming part.

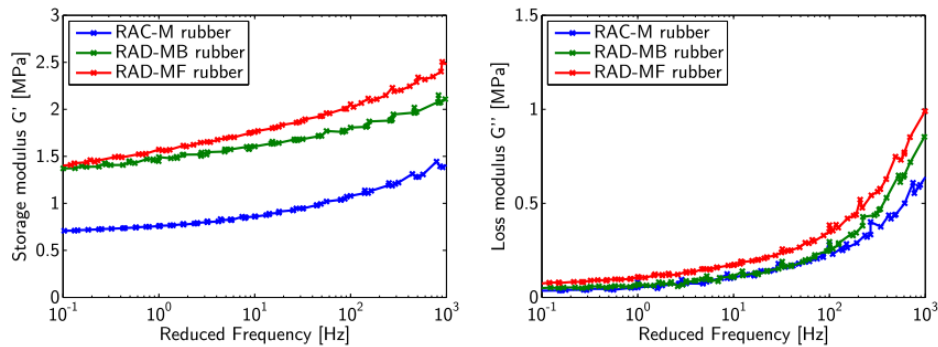


Figure 3.4: Result from Voormeeren et al. [71], used as guideline

The Zener model, shown in Figure 3.2.c, represents the behaviour of a linear standard viscoelastic solid. It consist of two springs in parallel where one is placed in series with a dashpot. The Zener model merges the behaviour of the previously looked at Maxwell and KV models. The hysteresis of the Zener model is not

modelled in a quasi-static load case. The strain rate approaches zero in such an analysis and therefore the contribution from the dashpot is very small. This can be seen in Figure 3.5 where the loss modulus is zero at a frequency of zero Hertz. The SLS model can be represented by the following differential equation and complex modulus.

$$\sigma(t) + \frac{\eta}{E_d} \frac{d\sigma(t)}{dt} = E_\infty \varepsilon(t) + \eta \frac{(E_\infty + E_d)}{E_d} \frac{d\varepsilon(t)}{dt} \quad (3.19)$$

$$E_{sls}^* = \frac{E_\infty E_d^2 + (E_d + E_\infty) \eta^2 \omega^2 + E_d^2 \eta \omega i}{E_d^2 + \eta^2 \omega^2} \quad (3.20)$$

The storage modulus of the Zener model at low frequency is now determined by the value of E_∞ . This yields a more realistic (quasi-)static behaviour. The asymptotic values at infinitely large frequency are given by Equation 3.21.

$$\begin{aligned} \lim_{\omega \rightarrow \infty} \operatorname{re}[E_{sls}^*(\omega)] &= E_d + E_\infty \\ \lim_{\omega \rightarrow \infty} \operatorname{im}[E_{sls}^*(\omega)] &= 0 \end{aligned} \quad (3.21)$$

The position of the peak of the loss modulus can be related to the ratio between E_d and η .

$$\omega \approx \frac{E_d}{\eta} \quad (3.22)$$

[60]

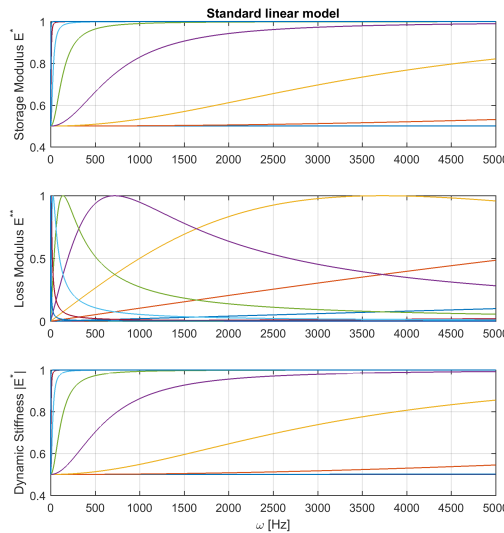


Figure 3.5: SLS / Zener model

The reviewed Zener model is, like the Maxwell and KV model, limited in the shape it can adapt to. To increase the correlation between the Zener model fitted to experimental data, more Maxwell elements can be added to the model. By doing so, a generalized Maxwell model is created. In the next part the GMM is reviewed including some additional modifications.

When multiple Maxwell models are connected in parallel a Generalized Maxwell Model (GMM) is created as shown by Figure 3.6. The addition of more Maxwell elements gives the GMM more ability to fit experimental data with minimal error. Negative effect of this addition is a more complex material model, with more parameters to fit. The number of Maxwell elements must be a compromise between frequency range of interest, precision and computational effort. Equal to the Zener model, the static behaviour is determined by the value of E_∞ which is referred to as the static stiffness.

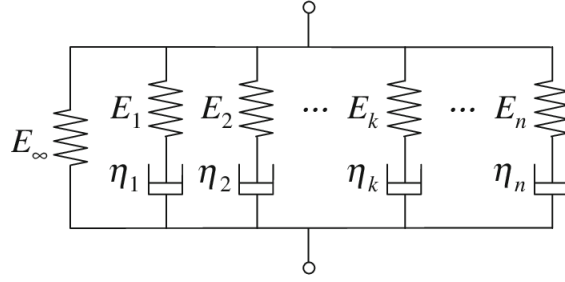


Figure 3.6: Generalized Maxwell Model (GMM)

Rouleau et al. [57] shows rubber modelling with a GMM. The complex modulus of the GMM is represented as:

$$G^*(\omega) = G_\infty + \sum_{k=1}^m G_k \cdot \frac{i\omega\tau_k}{1 + i\omega\tau_k} \quad (3.23)$$

Rewriting Equation 3.23 with the relation $\tau_k = \eta_k/G_k$ from Thorin et al. [64] and the fact that both η_i and C_i represents both dashpot values gives:

$$G^*(\omega) = G_\infty + \sum_{i=1}^N \frac{G_i\eta\omega j}{G_i + \eta\omega j} \quad (3.24)$$

Writing in a clear way, separating storage and loss modulus gives:

$$G_{gmm}^*(\omega) = G_\infty + \sum_{i=1}^N \frac{G_i\eta^2\omega^2 + G_i^2\eta\omega j}{G_i^2 + \eta^2\omega^2} \quad (3.25)$$

The previous result shows the comparison between the presented equations of Jrad et al. [31] and Rouleau et al. [57]. The GMM is capable of representing every complex modulus of interest.

$$\begin{aligned} \lim_{\omega \rightarrow \infty} \text{re}[G_{gmm}^*(\omega)] &= G_0 + \sum_{i=1}^N G_i \\ \lim_{\omega \rightarrow \infty} \text{im}[G_{gmm}^*(\omega)] &= 0 \end{aligned} \quad (3.26)$$

Thorin et al. [64] modifies the GMM with a prestrain dependence. More on the effect of prestrain can be found in section 2.4.1. In this research the spring properties are made dependent on the prestrain level. A linear and proportional difference functions are used for the prestrain dependence. The proportional function has a value at which it becomes active. If the prestrain is below the value, it can be considered that the effect is negligible. It is able to implement the effect up to a prestrain of 6%. Above this the writer advised to develop new Maxwell elements.

The work of Jrad et al. [31] tries to model the nonlinear behaviour by adding a nonlinear spring in parallel with the GMM making it a nonlinear GMM (NLGMM). The philosophy behind this model is the separation of nonlinear elasticity (hyperelastic) and linear viscoelasticity. In the FE software Abaqus, the combination of hyperelasticity and viscoelasticity leads to an equivalent NLGMM. Jrad et al. [31] presents the equation for the dynamic stiffness of a NLGMM:

$$Z^*(\omega) = K_0 + \sum_{i=1}^N \frac{K_i C_i \omega j}{K_i + C_i \omega j} \quad (3.27)$$

Applying a viscoelastic model to a wide frequency range often leads to an increasing number of parameters. In the search of describing large frequency range behaviour with limited parameters, the fractional derivative model has been researched and applied. The work of Rouleau et al. [57] also shows the modelling of rubber with a fractional derivative model (FDM). In a FDM the dashpots are replaced by pot elements. The complex modulus of the FDM is represented as:

$$G^*(\omega) = G_0 + (G_\infty - G_0) \cdot \frac{(i\omega\tau)^\alpha}{1 + (i\omega\tau)^\alpha} \quad (3.28)$$

In general the FDM needs significantly less parameters to yield the same fitting quality as that of the GMM and is advised when large frequency range is considered [50]. In this research the results are 24 vs. 4 parameters.

The GMM is implemented in the FE software *Abaqus* by the Prony series. The Prony series is the Fourier Transform of the time domain relaxation. The Prony series within Abaqus is used in combination with the hyperelastic properties. The Prony series has advantages over the previously mentioned FDM. The Prony series is more numerical efficient because the response depends only on the previous step, whereas the FDM depends on the entire strain history [50]. The Prony series method also has the advantage that it is implemented in the software which is used for in this research.

In the frequency domain the Prony series are represented by:

$$G_s(\omega) = G_0 \left[1 - \sum_{i=1}^N \bar{g}_i^P \right] + G_0 \sum_{i=1}^N \frac{\bar{g}_i^P \tau_i^2 \omega^2}{1 + \tau_i^2 \omega^2} \quad (3.29)$$

$$G_l(\omega) = G_0 \sum_{i=1}^N \frac{\bar{g}_i^P \tau_i \omega}{1 + \tau_i^2 \omega^2} \quad (3.30)$$

$$e^2 = \sum_{i=1}^M \frac{1}{G_\infty^2} \left[(G_s - \bar{G}_s)_i^2 + (G_l - \bar{G}_l)_i^2 \right] \quad (3.31)$$

The parameters Abaqus needed to define the Prony series are; g_i , τ_i . The Prony series in Abaqus is limited to 12. Abaqus/Standard assumes that the frequency dependent shear, which acts in deviatoric way, and volumetric behaviour are independent. The volumetric behaviour again can be expressed by a storage and loss moduli [Abaqus manual]. It is however assumed that the bulk modulus is not of interest for an incompressible material in this application.

3.2.1. Nonlinear viscoelasticity

In the previous section it is assumed that the rubber behaves in a linear viscoelastic manner. It is shown that such behaviour is observed for unfilled and lightly filled NR. If the NR is filled the dependence on dynamic strain amplitude cannot be easily ignored. As discussed in section 2.4 the Payne effect describes this softening phenomenon. Rate-independent damping mechanisms has been used in order to model the amplitude dependence. Frictional elements are used to represent the Payne effect [4]. Austrell [4] presents a combined viscous and frictional model. It is a Zener model extended with a friction and spring element in parallel. This model included step size dependent relaxation and amplitude dependent dynamic modulus.

The work of Gil-Negrete et al. [26] combines a FDM with frictional elements to model the nonlinear viscoelastic behaviour of CB filled NR. The model is shown in Figure 3.7(a). It shows the so called overlay technique to overcome disabilities from the FE software. Different FE models are created with identical meshing and nodes but with different material definitions. After the applied loading the results of the individual models can be merged as shown in Figure 3.7(b). The applied loading conditions must be displacement inducing straining because applying force will result in variation of displacement between the models. The resulting stresses from the different FE models can be added.

The work of Olsson and Austrell [51], Laka [36] and Sandell [59] also shows the use of the overlay technique for including the Payne effect in a nonlinear viscoelastic material model. More on the effect of adding frictional elements to previously mentioned linear viscoelastic material models can be found in Appendix B in the work of Karlsson and Persson [33].

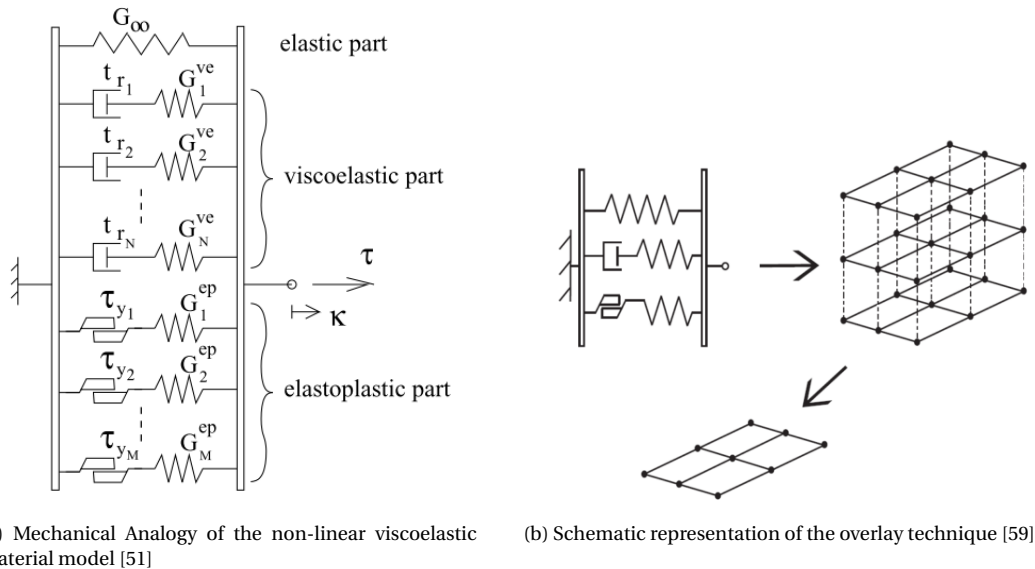


Figure 3.7: Overlay technique

3.3. Conclusion on rubber modelling

This section concludes the previously remarks in terms of modelling rubber specific behaviour. A selection of models is reviewed that can represent hyperelastic or viscoelastic behaviour.

The hyperelastic models where reviewed first. Material composition is not provided by the manufacturer and therefore the so called phenomenological models are preferred. The model does not have to capture the upturn at large deformations because of limited range of motion of an engine mount. To capture this upturn a higher order polynomial is needed which lead to more computational effort. The remaining models that are phenomenological and limits computational effort by ignoring the upturn are the Neo-Hookean and Mooney-Rivlin models. It is shown that the Mooney-Rivlin is not good in undergoing deformation modes other than the ones fitted to. The MR model is based on the first and second strain invariant and it is shown that the dependence on NR on the second strain invariants is small. These facts make it that it is expected that the *Neo-Hookean* hyperelastic material model will be sufficient to represent the (quasi-)static behaviour of NR.

Secondly the material models that can represent viscoelastic behaviour are reviewed. It is shown the the more simplified models such as the Maxwell and KV connect represent the complex viscoelastic behaviour of rubber over a large range of frequency. The Zener model (SLS) improves in that fact with limited parameters, however it lacks in the capability of fitting to experimental data. This can be improved by making use of the *Generalized Maxwell model* which is a Zener model added in parallel with Maxwell elements. The additional elements gives it more mobility to adapt to experimental data. The GMM is more numerical efficient than the FDM because the response depends only on the previous step, whereas the FDM depends on the entire strain history. The GMM is implemented in Abaqus that is the FE software used during the Master Thesis.

The modelling of nonlinear viscoelastic behaviour is also briefly discussed. It not expected that the vibrations excite the nonlinear viscoelastic region. This expectation can be affected by the unknown filler content and therefore knowledge is needed to capture this effect when it is being observed during experiments. Adding frictional elements cannot be combined with a viscoelastic material model which makes it necessary to use of the overlay method.

4

Experimental Characterization

4.1. Hyperelasticity

This section gives more insight in the experimental effort needed to characterize hyperelastic behaviour. The three most commonly used tests are described. The experimental process is briefly explained before there is looked at data processing that includes determining output that can be used for the hyperelastic material model described in section 3.1.

Data for rubber material models can be obtained from tests in uniaxial tension, uniaxial compression (equibiaxial tension) and simple (pure) shear. It is possible to fit the material model to data obtained from a single test. The coefficients obtained are proven to perform well in describing loading condition equal to that of the test. As described in section 3.1 material models have difficulty with describing other modes of deformation than the one fitted to, which makes it limited in use. With this knowledge it seems reasonable to assume that more modes of deformation improves the robustness of the material model.

4.1.1. Uniaxial test

In this test the goal is to subject the specimen to a pure tensile strain. To achieve this goal, no lateral constraints must be present that can prevent the specimen from thinning. This thinning is a response to the tensile strain. It is widely accepted that this is the case when the specimen is at least 10 times longer than the thickness or width. Care should be taken when measuring the elongation of the specimen. This cannot be done at the clamps, but has to be done at the specimen away from the clamps at a position where only pure tensile strain is present. Measuring is done by a noncontacting device like a video or laser extensometer. The load P can be measured by a load cell. The relevant principle strain and stresses are given by:

$$\lambda_2 = \lambda = \frac{L}{L_0}, \quad \lambda_1 = \lambda_3 = \sqrt{\frac{A}{A_0}} \quad (4.1)$$

$$\sigma_2 = \sigma = \frac{P}{A_0}, \quad \sigma_1 = \sigma_3 = 0 \quad (4.2)$$

4.1.2. Biaxial test

During a biaxial tensile test the sample is equally strained in two directions.

$$\lambda_1 = \lambda_2 = \lambda = \frac{L}{L_0}, \quad \lambda_3 = \frac{1}{\lambda^2} \quad (4.3)$$

$$\sigma_1 = \sigma_2 = \sigma, \quad \sigma_3 = 0 \quad (4.4)$$

About compressive test: Equivalent to biaxial deformation • Lubricated platens minimize “barrelling” • May contain volumetric effects • Not good at high strains

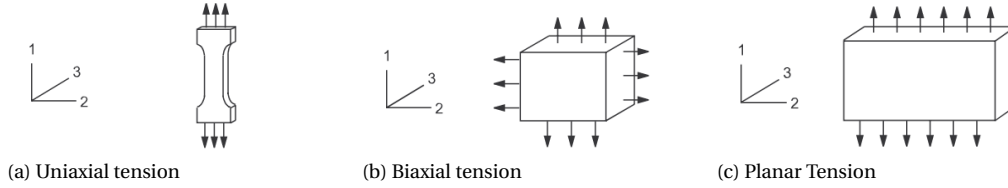
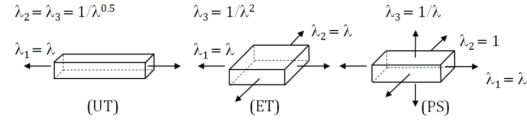


Figure 4.1: Schematic representation of hyperelastic experiments

Strain invariant	UT	ET	PS
I_1	$\lambda^2 + 2\lambda^{-1}$	$2\lambda^2 + \lambda^{-4}$	$\lambda^2 + \lambda^{-2} + 1$
I_2	$2\lambda + \lambda^{-2}$	$\lambda^4 + 2\lambda^{-2}$	$\lambda^2 + \lambda^{-2} + 1$
I_3	1	1	1

(a) Strain invariants in relation the principle stretch



(b) Principle stretches during experiments

Figure 4.2: Relevant relation for hyperelastic experiments

4.1.3. Planar tension test

This test is also referred to as the planar shear test. It shows comparison to the uniaxial tension test, only with a very wide specimen. Due to the geometry of the specimen it is possible to apply a pure shear state at some location of the specimen. The width is now at least 10 times bigger than the length in tension. The test is very sensitive to this ratio. With this ratio it is accepted to assume that thinning only occurs in the thickness direction [2]. At the center of the specimen a pure shear exists at a 45 degree angle to the stretching direction.

$$\lambda_1 = 1, \quad \lambda_2 = \lambda = \frac{L}{L_0}, \quad \lambda_3 = \frac{t}{t_0} \quad (4.5)$$

$$\sigma_1 \neq 0, \quad \sigma_2 = \sigma, \quad \sigma_3 = 0 \quad (4.6)$$

4.2. Viscoelasticity

In order to parametrize the viscoelastic material model, a so called Dynamic Mechanical Analysis (DMA) needs to be performed. During this analysis the rubber sample will be dynamically strained with a sinusoidal vibration. Complex moduli are results obtained during such analysis and are a function of frequency. The complex modulus that is obtained depends on the loading condition the sample is excited to. The DMA can obtain results for a large frequency range by making use of the time temperature superposition principle (TTSP). It is shown that lowering temperature has the same effects as increasing frequency. By cooling the sample the frequency during the experiment can be limited to 100Hz while obtaining results in a KHz range. Shift factors need to be determined in order to relate a temperature change to a change in frequency. A so called master curve can now be obtained which consists of individual temperature measurements.

A more thorough explanation of the DMA of rubber can be found in the work of Menard and Menard [41]. An example of experimental results for three different rubber mounts can be found in the appendix of the work of Voormeeren et al. [71].

5

Summary and Conclusion

This section summarizes and concludes the finding of the previous chapters. In this literature review the goal was to find answers to the question *"How and which rubber specific behaviour must be included in a numerical model to properly predict the dynamic behaviour of a rubber engine mount under steady-state conditions?"*. The main question is subdivided and is answered in terms of rubber specific behaviour and which are relevant, its mechanistic explanation, external triggers, representation by material models, experimental needs and influence of aforementioned in the dynamic behaviour.

In this literature study it is shown that in general the behaviour of rubber is rather complex. The behaviour is influenced by material composition where the addition of filler plays a dominant role. The complexity of the behaviour is related to difficulties in both characterization and modelling. Rubber is characterized by its hyperelastic and viscoelastic behaviour triggered by static and dynamic straining respectively. Rubber exhibits also softening effects which are called the Mullin's and Payne effect. The effect of prestrain on rubber behaviour is researched and should be considered in this research.

Hyperelasticity is characterized by a strong nonlinear relation between stress and strain under static loading conditions. The stretched polymer chains are at a certain point extended to a maximum which is determined by the covalent cross links. Reaching this limit results in a drastic increase of modulus. The behaviour is triggered by large deformation and is observed in a range of 100s of percent deformation. For this research a significant static deformation is expected, however in general engineering application such range is not reached. It is therefor reasonable to assume that only a limited section of the hyperelastic curve is triggered during the static deformation. In this research the modelling of the behaviour is only focused on mimicking the effects observed during experiments, which makes the phenomenological models the most interesting. The hyperelastic behaviour can be modelled with a strain energy density function which describes the surface under the stress-strain curve. Because the upturn does not have to be captured in the material model the amount of parameters can be limited, which minimizes both computational and experimental effort. Because of the choice for a phenomenological model which not have to capture the upturn and limits computational and experimental effort the Neo-Hooke, Mooney-Rivlin and Yeoh are models that fit these criteria. Typically three deformation modes are triggered during experiments to properly fit the material model parameters. These three deformation modes are uniaxial, biaxial and planar tension. The exact need of experiments is determined by the choice of material model and the deformation modes that are expected for the real situation. Considering the previously chosen material models, the material parameter fit has a more significant influence on the static and low frequency solution of the FE model than the choice of material model. The static solution determines the initial conditions for the dynamic analysis and therefor an offset for the dynamic solution is expected when material parameters are not fitted correctly. It is expected that the initial conditions effect storage but not loss modulus. Peaks of the eigenfrequencies are therefor expected to be constant, but the location are likely to vary.

- Hyperelasticity: represented by a Strain Energy Density function
- Engine mount has limited range of motion: upturn in s-shaped curve not triggered
- Material model does not have to capture upturn: simplified material model

- Material composition not provided by manufacturer: phenomenological models preferred
- Engine mount made of Natural Rubber: dependence on second strain invariant is small
- The *Neo-Hooke model* is able to represent the NR (quasi-)static behaviour sufficiently for this application

The linear viscoelastic behaviour describes the stiffness and damping which are frequency dependent. In order to model the dynamic behaviour properly, the viscoelastic properties are of interest. The frequency range of interest is rather large and therefore the effect it has on the viscoelastic behaviour as well. High frequency excitations are typically characterized by their low amplitude and therefore it is expected that linear viscoelastic behaviour can be considered. In this literature review the most applied viscoelastic models are discussed. They are of the rheological sort which represents the behaviour with a combination of springs and dashpots. In general, when comparing trendlines, it is proven that the Zener model yields the most promising dynamic behaviour when comparing to experimental result from other research. The trendline gives information about the dynamic character of the combined elements, however not about its capability of merging to experimental data. To improve this ability it can be extended to a generalized Maxwell model. The generalized Maxwell model is represented in Abaqus by the so called "Prony series". The viscoelastic properties within Abaqus makes use of a long term elastic modulus which is the static value. Abaqus gets this value from the hyperelastic material model previously mentioned. The hyperelastic and viscoelastic material defined in Abaqus are cooperating and are dependent on each other. During this research the viscoelastic material properties are represented by the Prony series in Abaqus. A dynamic mechanical analysis gives enough information to determine the viscoelastic properties of a rubber sample. The sample can be exposed to multiple deformation modes and a large frequency range result can be observed with such an analysis. The use of the device is rather expensive for this application and is therefore not used during the research. As a first assumption experimental data is used from another research that matches this one. This result will give a good starting point for further refinement. The choice of material model determines how well the model is capable to fit experimental data over a certain frequency range. Deviation in terms of fitting translated to both stiffness and damping properties under influence of frequency. A change of resonance frequency and peak height is expected due to the change in stiffness and damping respectively.

- Interest in describing the behaviour over a large frequency range
- Vibrations are of small amplitude: linear viscoelastic behaviour
- Behaviour represented in a rheological way: spring and dampers
- Model must fit experimental data with limited error: higher order polynomial
- The *Generalized Maxwell model* with a sufficient number of elements is able to describe the linear viscoelastic behaviour over a large range of frequency
- DMA can be used to provide data to characterize the viscoelastic material model
- GMM implemented in Abaqus by means of "Prony series"

The Mullin's and Payne effect are two types of softening phenomena triggered in different ways. The Mullin's effect can be seen as damage done during the first loading cycle of a higher level than the prior all-time maximum value. After a few loading cycles the internal microstructure reaches a permanent state. Recovery of the Mullin's effect is not observed at room temperature. The Mullin's effect is explained in multiple ways throughout literature. The mechanisms responsible for the Mullin's effect are covalent bond rupture, slipping of molecules, filler rupture and disentanglement. It is an effect which is not relevant for modelling, but needs to be taken into account during experiments. Experiments have to be done on preconditioned samples that are loaded beyond the level excited to during the dynamic experiment. For the practical situation it seems reasonable to expect that an engine mount is preconditioned during dynamic driving conditions. Dynamic excitation during steady-state conditions are not expected to be higher than during cornering situations for example. Because no recovery is observed the preconditioning holds over time. The Payne effect is also a softening phenomenon but cannot be seen as damage. It is triggered by a dynamic strain amplitude that lies outside the range wherein linear viscoelasticity is valid. The Payne effect increases with the amount of filler and is not present at unfilled rubber. Because composition of the sample is not known the Payne effect cannot be excluded. Research that is discussed in this literature review gives reason to assume that the Payne effect is not triggered in the application of interest. This is due to the expected dynamic strain amplitude which is small and the fact that the NR used for the engine mount is not expected to be highly filled. Effort should be made to be sure that the Payne effect is not present during experiments. Fitting a linear viscoelastic material to nonlinear behaviour will introduce unnecessary errors. If the Payne effect is observed a nonlinear

viscoelastic material model must be used. The overlay technique shows to be a good method to combine hyperelasticity with frequency and amplitude dependent behaviour within a FE model. Multiple models with identical meshing represent the individual behaviour. Stresses from the different models that are introduced by the applied strain can be added in order to find the final solution.

Payne effect

- Payne effect: amplitude dependent viscoelastic behaviour
- Small vibration: no Payne effect expected in real case situation
- Experiments: displacement controlled to prevent the Payne effect from occurring
- Filler content unknown: strain level at which the Payne effect is observed is uncertain

Mullins effect

- Mullins effect observed during first few loading cycles
- Experiments: sample must be preconditioned by loading it with an x number of times to a strain higher than expected during experiments
- During dynamic driving conditions the engine mount is expected to be preconditioned already in the real case

6

Master Thesis Approach

This final chapter will present the approach for my upcoming master thesis. The approach is a result of the knowledge collected in this literature review and things encountered while setting up the master thesis plan. The thesis will begin with creating more knowledge on the effect of material parameters on static and dynamic stiffness. The knowledge is needed to later on be able to vary observed differences.

1. Create general knowledge on
 - the effect of material parameters on static and dynamic stiffness
 - experimental needs

In parallel to the previous step the thesis start with characterizing the geometry of the engine mount and define sufficient simplifications being applied to the modelled geometry. The static displacement under a certain load must be obtained experimentally resulting in the geometry related stiffness. If the geometry is modelled correctly the static behaviour from the FE model can be merged with experimental result. By doing so, the first improvement of the material parameters is made.

2. characterize and model geometry of engine mount
3. apply simplification to geometry in FE model
4. experimentally characterize static stiffness
5. compare FE analysis with experimental results
6. improve material parameters that concern static behaviour

If the static behaviour is matched to focus lies on the dynamic behaviour. The dynamic behaviour will be experimentally characterized by means of its dynamic stiffness. Inertia effect are affecting the dynamic stiffness and therefor the vibrating shell must be characterized by means of inertia in six DOF. The dynamic stiffness is determined by making use of shaker or impact test. More knowledge is needed to decide on the method to use. Forces will be detected by making use of a load cell that can operate in compression and tension loading conditions. Results will be obtained up to a maximum frequency allowed by the used method. Larger frequency range limits extrapolation errors. Again the experimental results are compared with the dynamic behaviour obtained with the FE analysis. The goal is to find general differences between the two results. The knowledge generated on the effect of material behaviour on the dynamic stiffness can be used improve the material parameters in order to better adapt to the experimental behaviour.

7. experimentally characterize dynamic stiffness
8. identify striking differences between data from experiment and FE analysis
9. adapt material model parameters without affecting static behaviour
10. create general guidelines for modelling the dynamic behaviour

The final goal of the master thesis is to characterize the dynamic behaviour of a rubber engine mount and capture this in a FE model that fits the dynamic substructuring framework.

10. Output the dynamic stiffness;
 - in six DOF

- as a function of frequency
- between two virtual points

11. Validation in the real case and mounted situation

It must improve current techniques that mimic the dynamic stiffness. Ultimate validation will be when it is able to improve transfer functions of connected structures with the engine mount being mounted in between them.

II

Part Two - Thesis

7

Case Introduction

In this chapter more information can be found on the case which is studied in this research. The problem statement, which also sketches the context, can be found in Section 7.1. The characterization approach is presented in Section 7.2. Besides that Section 7.2 also includes the challenges, arising from the approach. The scientific contribution of this work is clarified in Section 7.3. The properties and the reasoning behind the chosen object can be found in Section 7.4.

7.1. Context and Problem Statement

The characterization of rubber dynamic behaviour is proven to be a difficult topic. Nowadays impacts methods [27, 39, 52] are used for characterizing the dynamic properties of rubber elements. The method does not extract material properties which the disadvantage that results are case specific. The approach of Haeussler et al. [27] is interesting because its output can be made directly comparable with numerical results. Although the method is promising it has some negatives:

- Obtaining the dynamic stiffness requires matrix inversion. Measurement errors can have a significant affect on the matrix inversion.
- From the experiment only the transfer-stiffness can directly be determined. The attached structure eliminates the ability to directly obtain the drivingpoint-stiffness¹. Decoupling methods and therefore knowledge on the dynamic behaviour of the attached structures is needed to obtain the drivingpoint-stiffness.
- The characterization approach is geometry related. The results cannot be extrapolated.

The goal is to extract the rubber material properties by making use of impact testing. Obtaining a correct material model opens up a range of opportunities. The material properties enables one to overcome the drivingpoint-stiffness characterization difficulties. The method expands the experimental characterization abilities. It has the ability to reduce the necessary experimental effort and can increase the quality of difficult to characterize DoF of the stiffness matrix. The inverse approach opens the opportunity for extrapolating results to other geometries of the same material. Next it is explained by which approach these goals are to be reached. Also the challenges, needed to be overcome, are presented.

7.2. Approach and Challenges

In between the literature review and the actual research it was concluded that a DMA measurement couldn't be conducted as a consequence of lacking budget. It introduces more uncertainties with respect to the material model parameters which again has an effect on the performance of the numerical model. Despite these facts, this work presents a promising approach for conquering these negatives. The alternative approach includes the following steps:

1. Experimentally characterize the research object by making use of impact testing.

¹The BS ISO 10846 states that the dynamic driving point stiffness is the frequency dependent ratio of force on the input side of vibration isolation to the displacement on the input side with the output side blocked.

2. Obtain an initial viscoelastic material model
3. Obtain the transfer-stiffness from a FE model that includes a viscoelastic material model.
4. Build a tool which can optimize the initial material model parameters to match the experimental data.
5. Expand the numerical model to match the experimental setup. Obtain the drivingpoint-stiffness which is used as a validation measure with respect to the experimental results.

From the previous steps a number of challenges arise:

- Experimentally characterize the research object considering the damping and the nonlinear material behaviour.
- Obtain an initial viscoelastic material model with zero material specific data.
- Construct a FE model including a viscoelastic material model from which the transfer-stiffness can be obtained between two virtual points.
- Build an optimization tool which requires to interconnect Matlab with FE software and Python.
- Expand the numerical model to sufficiently mimic the experimental situation.

The results in this work are findings to the following questions:

- **Can a combination of impact testing and numerical simulation provide a method to obtain rubber material properties?**
- *Which experimental conditions are needed to characterize only the rubber object?*
- *Does an impact test method provide good quality data for the optimization?*
- *Which approach is needed to make the experimental and numerical results comparable?*
- *Which experimental results are best used as a reference value for the optimization?*
- *What optimization approach is best for this case?*
- *Does the optimized material model resembles behaviour observed in literature?*
- *Can the experimental results provide one with a validation measure?*

7.3. Contributions

In this section it is shown which scientific contributions this work provides.

1. The inverse approach enables one to extract material properties from the experimental impact method.
2. The impact method is able to characterize the dynamic transfer-stiffness of a rubber object up to the first eigenfrequency of the attached structures.
3. It is proven that an initial viscoelastic material, obtained from other research, is sufficient for optimization purposes. The optimization method enables one to find a global minimum for a time consuming objective function.
4. Without applying decoupling methods, which require knowledge on the dynamic behaviour of the attached structures, it is possible to numerically predict the drivingpoint-stiffness within a respectable margin.
5. The presented method enables one to significantly reduce the experimental effort.
6. The moduli optimized for a translational load case is usable for prediction a, hard to experimentally characterize, rotational load case.

7.4. Research object

The goal of this research is to characterize the dynamic rubber properties. A commercial vibration damper is used, which provided no information in terms of dynamic properties or material composition. It is a Natural Rubber (NR) that has a Shore A hardness of 58.

The research object is a cylindrical shaped vibration damper. These type of vibration dampers are used for mounting a vibration source (engine) on a base or in a frame. It consists of a cylindrical rubber component that is fixed to two metal faces. The steel plate is on the other side connected to a M10 thread. A schematic representation of the vibration damper is shown in Figure 7.1 and the geometric parameters D , H and h are presented in Table 7.1.

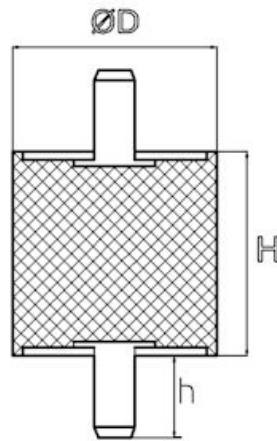


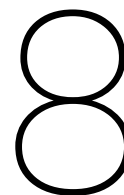
Figure 7.1: Cut-trough of the vibration damper used in this research

Table 7.1: Geometric parameters of the vibration absorber

Object nr	D [mm]	H [mm]	h [mm]
<i>I</i>	50	30	28

The object is chosen because:

- The basic geometry enables one to minimize the complexity of the numerical model. In this work, fast simulations are dominant over model complexity.
- The object can be directly mounted to other structures which is beneficial for the experimental setup.
- The rubber is bounded to a stiff metal surface.



Numerical

This section describes the process of modelling and simulations. Both are done with Abaqus which is mainly used for its wide variety of viscoelastic material models. The results are analysed with Matlab. In this work the ability of Abaqus to be activated with Matlab is proven to be very beneficial.

In Section 8.1 the general numerical approach is presented. It is a quick overview from which the modelling, simulation and analysis steps can be obtained. Secondly in Section 8.2 the construction of the FE model is presented. The construction of the FE model concerns meshing, virtual point implementation, numerical effects and boundary conditions. Hereafter in Section 8.3 the choice of material model is presented including the derivation of the material model parameters.

Section 8.4 describes the process of running simulations. Which steps are needed to extract the relevant output and which loading and boundary conditions need to be applied. In this section it is further defined which steps are needed to simulate relevant experimental conditions.

8.1. Approach

The main goal in this chapter is to obtain the dynamic stiffness matrix from the rubber cylinder by making use of numerical simulations. Therefore a model has to be built with an appropriate material model which represents the complex dynamic behaviour of rubber. The analysis depends on running dynamic simulations which are needed to be set up. The results of the simulations need to be translated to Matlab in which it can be analysed.

The previously mentioned overview can be simplified towards the following steps:

1. Construct the FE model concerning:
 - (a) build geometry (Sec. 8.2)
 - (b) meshing taking into account the complex rubber behaviour (Sec. 8.2)
 - (c) boundary conditions (Sec. 8.2)
 - (d) coupling methods (Sec. 8.2)
 - (e) derivation of initial material model parameters (Sec. 8.3)
 - (f) implement dynamic simulation (Sec. 8.4)
2. Data-transfer (Sec. D)
 - (a) input parameters for geometry and material model
 - (b) output relevant field output for constructing dynamic stiffness matrix
3. Data-processing (Sec. 8.4.1)
 - (a) Construct Dynamic Stiffness matrix

8.2. FE Model

In this section the full build of the FE model is described. Background knowledge, with respect to element criteria, coupling methods and boundary conditions, is presented from which FE choices can be explained.

8.2.1. Element selection

Size, shape, order of interpolation and type of integration are all factors which influence the results determined by the FE software. The available element shapes are further defined in Section 8.2.1. The order which is used for interpolating results in between corner nodes is in further detail explained in Section 8.2.1 and the integration method in Section 8.2.1. The interpolation method effects solutions like the displacement field. Stress and strain are a solution which are found in an integral way. The integration method determines the number of points within the element where integral solutions need to be determined.

Element shape

For a 3D stress analyses, Abaqus includes a number of element shapes; hexahedral, tetrahedral and pentahedron elements. Later also referred to as hex, tet and wedge elements respectively. Figure 8.1 shows hex, wedge and tet elements in both linear and quadratic order from left to right respectively. The choice for a certain element shape depends mostly on the geometric complexity, the expected level of stress and strain and the type of simulation.

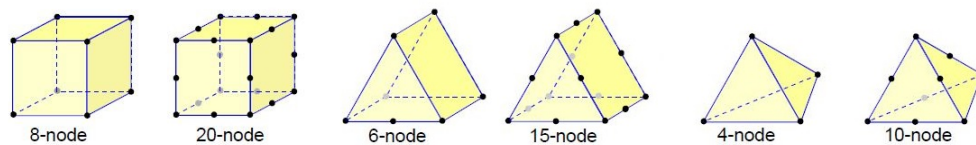


Figure 8.1: 3D stress element types

Tet elements will not be used in this research. Tet elements are outperformed by hex elements when it comes down to convergence rate. If the shape is meshed with hex elements in a good way, accuracy is equal at lower computational effort. The strength of tet element is that these elements are better in filling up complex geometric sections. Because this work contains a basic geometry, tet elements are not used.

Hybrid formulation

As described in Section 2.1 rubber shows (nearly) incompressible behaviour. Applying incompressible behaviour to a standard numerical element adds an extra constraint which makes the element overconstrained. If such an element cannot resolve all these constraints, it will suffer from *volumetric locking*¹

Think of a cylinder filled with rubber, that is being compressed by a piston. It can be imagined that there is almost zero piston displacement, however a significant stress is build up inside the rubber element, which adds stiffness to the geometry. A very small displacement leads to a extremely large change in pressure. The displacement-based solution that is used in standard element types is far to sensitive. Round-off from the computer can be a reason for this technique to fail. The solution for an incompressible material can therefor not be obtained in terms of the displacement history only.

A way to prevent volumetric locking is to apply the hybrid formulation. Hybrid element use is advised when modelling fully incompressible material and also nearly incompressible material that shows hyperelastic behaviour [18]. The hybrid formulation is only present in the Abaqus/Standard software and is therefore a reason to use this specific software type from Abaqus. A hybrid element separates the pressure stress from the displacement solution and couples both solution with the constitutive theory and the compatibility condition [18]. The coupling is implemented by Lagrange multipliers. Adding more internal variables will lead to more computational effort. A hybrid element also has an active distortion control with a default length ratio of 0.1.

Tet and wedge elements are advised to use only for filling regions of meshes of hex-type elements. Each hybrid tet-element (C3D6H) adds a constraint equation to fulfil the incompressible behaviour. A mesh with only such elements will be overconstrained [18]. Quick and stable simulations are dominant and no complex geometries are present. The rubber will be meshed with hybrid elements and the Abaqus manual advises to use hex shaped elements due possible overconstraintment when using tet shaped elements.

¹Volumetric locking can be indicated by large variations in hydrostatic pressure from one integration point to the other. In Abaqus the (hydrostatic) pressure, without averaging at the nodes, can be a method to check the presence volumetric locking. A quilt-style contour of the pressure will show this effect. If the pressure shows a checkerboard pattern volumetric locking is occurring. The checkerboard pattern represents significant changes in pressure between integration points.

First- and second-order elements

First- and second-order element are referred to as linear and quadratic elements under "Geometric order" within Abaqus. Because this terminology conflicts with others, the first- and second-order terms are used throughout this thesis. The order determines the way a solution is found in between the corners of an element.

- "First-order" means that the solution between the nodes is calculated by linear interpolation.
 - First-order interpolation applied on tet elements have generally poor convergence rate and therefore need very fine meshing to produce good results [18].
 - First-order tet and wedge elements are overly stiff in stress analysis resulting from their vulnerability to volumetric locking as described in Section 8.2.1 [76], even when using hybrid formulation [18].
- "Second-order" means that the interpolation function between the corners is of a quadratic form.
 - Second-order elements are able to capture geometric features, such as curved edges, with fewer elements than first-order elements. As discussed in Section 8.2.1, the meshing needs to be checked for distortion.
 - A second-order element is less sensitive to distortion. If there are severe stress concentration present in the model, second-order element will capture this more effectively [18].

Overly stiff in stress analysis, which makes them less useful because the stiffness of the geometric has an significant effect on the FRF determined during the dynamic analysis.

Full- and reduced-integration elements

Some solution are found be integrating over the volume of the element. Abaqus evaluates the response of the material at each integration point in each element that is present in the geometry. For almost all element types the Gaussian quadrature technique is used to integrate.

It is said that reduced integration elements experiencing problems with hourglassing and full integration elements are sensitive for both shear and volumetric locking. Because no pure bending is present, shear locking is not present in this research. Reduced integration is only an option for the hex element within the available element types.

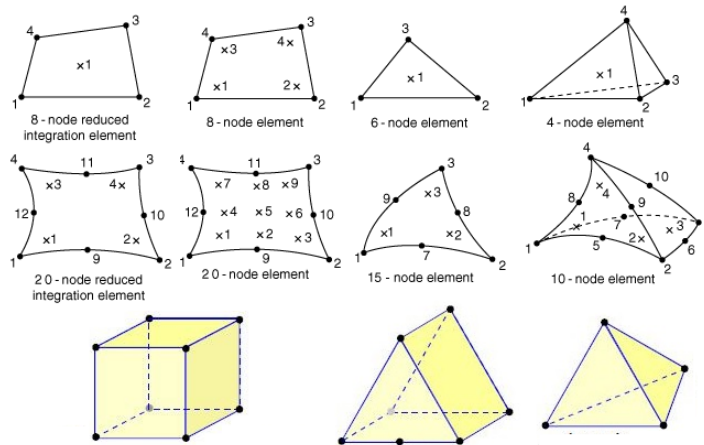


Figure 8.2: Integration points for output [<http://abaqus.software.polimi.it/v2016/books/usb/default.htm?startat=pt06ch27s01aus114.html>]

Summarizing the current section and also Section 8.2.1 will result in a selection of element which yet seems applicable for this research. Both first-order tet and wedge (tri) are both discarded from the available element types. That means that four element types are still available where the first- and second-order are the preferable shape. For large deformation with the risk of distortion, first-order elements are preferred. *The most volume should be meshed with first-order hex shaped elements. In complex sections of the geometry, tet or wedge elements can be used.* As a first assumption, first-order elements are preferred.

Table 8.1: Integration options for 3D stress elements

	Linear		Quadratic	
<i>Integration</i>	<i>Full</i>	<i>Reduced</i>	<i>Full</i>	<i>Reduced</i>
Hex	X	X	X	X
Wedge	X		X	
Tet	X		X	
<i>Pressure</i>	<i>Constant</i>	<i>Linear</i>	<i>Constant</i>	<i>Linear</i>
Hex	X			X
Wedge	X			X
Tet		X	X	

8.2.2. Coupling to Virtual Point

As previously mentioned, the goal is to find Dynamic Stiffness that fits within the dynamic substructuring framework. Results from this model must be compatible to;

- be coupled with experimentally characterized structures, and
- to be directly comparable to experimental results of the same object.

The coupling method of interest in this work is the virtual point² transformation method as described by van der Seijs et al. [68]. More background information with respect to the virtual point method can be found in Appendix A.1. The goal is to represent the VP conditions within the FE model. The results obtained from the numerical model can then directly be compared to the virtual point transformed experimental results.

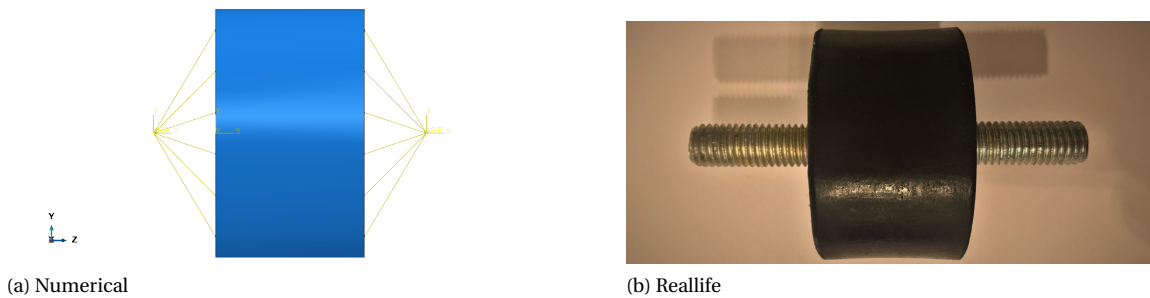


Figure 8.3: Side-views

The Virtual Point methods works on the assumption that the area between the Virtual Point, sensors and impacts is rigid. The measured values can then be transformed towards to virtual forces and displacements within the Virtual Point. A rigid coupling in FE software is a Rigid Body Element (RBE). The RBE2 and RBE3 coupling types are represented as a kinematic and distributed coupling within Abaqus respectively.

- The *kinematic coupling* is a RBE2 coupling which adds stiffness to the surface at which it is attached. It constraints motion between the nodes located at the meshed surface and the Virtual Point, which results in a nonuniform stress distribution at the surface.
- As the name suggest both *distributing type constraints* distribute the forces equally over the coupled surface and does allow relative motion between constrained and unconstrained DoF. The distribution type constraint allows the surface to deform, which results in a more uniform stress distribution on the surface.

The virtual points are modelled in Abaqus as reference points, which has no material properties and can be located anywhere. The connection between the rigid surface of the rubber geometry and the related reference point is made by adding coupling constraints. As previously mentioned the Virtual Point method work when assuming the surface is rigid. Therefore deformation of the surface is not allowed. Because of this reason the Kinematic Coupling is used which resembles an RBE of type 2.

The VP modelling allows one to apply displacement and forces directly to the virtual point, which is something is experimentally impossible. For determining the dynamic stiffness within and between the two virtual

²A virtual point is an imaginary point which can represent input or output forces and acceleration.

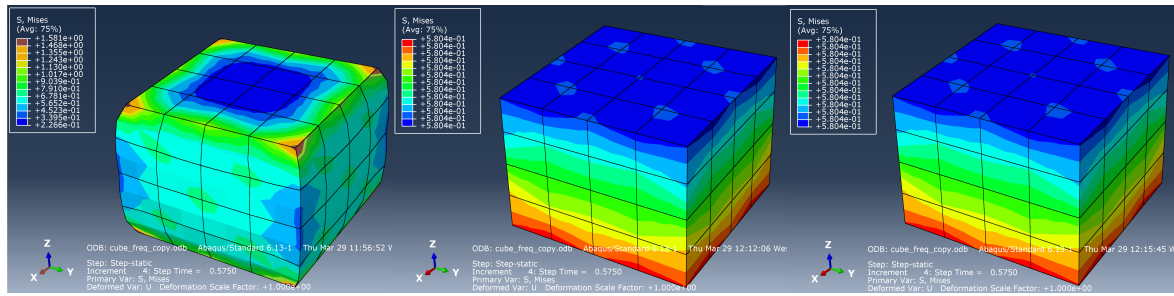


Figure 8.4: Coupling types; Kinematic, Continuum distributing and Structural distributing

points, the boundary conditions and loading conditions can now be applied at the virtual points.

Metal Shells

The stiffness of the metal shells is replaced by the RBE2 element. The material is several orders stiffer than the rubber. It will not be beneficial to model and mesh these parts because it will lead to more complex model increasing computational effort. The stiffness of the metal element is replaced by the coupling constraint added to the nodes that are located on the rubber/metal bonded surface [76].

Damping of the metal parts is neglected in the FE model. Metal is a material with minimal damping, which makes it reasonable to assume this is near zero with respect to the highly damped character of rubber.

The mass affects the dynamic stiffness with its inertia. For the mass effects two scenarios are possible:

1. *Compare the numerical results with experiments.*

If one's goal is to compare experimental results of the mount with that of the FE model than all inertia values of experimentally attached structures must be present within the model.

2. *Use the numerical results for coupling to other structures.*

If the stiffness from the FE model is determined with the goal of coupling, than the inertia can be neglected. The mass of the metal is big with respect to the mount's mass, but small in comparison to the structures later coupled with. The effect the metal mass has on the coupled FRF of the structure is negligible.

For the implementation of inertial values the reader is referred to Section 11.1 in which the numerical model is updated by implementing the inertia of the attached crosses.

8.3. Material model

In this work a viscoelastic material model is used to represent the rubber behaviour. It is chosen to represent the viscoelastic behaviour with tabular data. The Tabular data is a transformation of the DMA data and is a method in Abaqus to represent linear viscoelastic behaviour. In this section it is presented how the material model data is obtained. For theoretical background on viscoelastic behaviour the reader is referred to section 3.2.

Due to the limited time-frame and budget of this research no fundamental characterization such as a DMA could take place. A DMA would enable one to characterize the rubber within a large frequency range. Lacking the ability to execute such a measurement brings another challenge to the table. The challenge is to define a representative material model from literature with little knowledge on the rubber composition. The only known parameters of the rubber are that;

- it is a *Natural Rubber* and
- it has a Shore A hardness value of 58.

The alternative way for obtaining material model parameters is by combining experimental results of other research. The focus lies on finding data for NR with a known hardness. The parameters that are used in this work can be found in appendix B.2. In the next part it is presented how the material model parameters are obtained, but first some background on the rubber hardness measure.

Shore A Hardness

The Shore A hardness value is a commonly used measure for classifying rubbers. In this work it will be an alternative parameter that is used as an indirect measure for determining the material model parameters for the FE model. In practice two hardness measures are used. The International Rubber Hardness Degree (IRHD) and the Shore A hardness test. Both measures determine the hardness by indenting the rubber object where they differ in the probe shape that is used. The first is an ISO standard and both are nearly identical [59] in the hardness range of 30-80. The rubber used in this work fits this range.

A schematic presentation of the Shore A experiment is found in Figure 8.5. It is found that most rubbers used in vibration and shock isolators generally fall in the range of 35–75 durometer on the Shore A scale [67]. In this work, but in many cases, the hardness is the only available material parameter. The relation between hardness and stiffness is defined by ISO standard 48:2010 which is empirically determined.

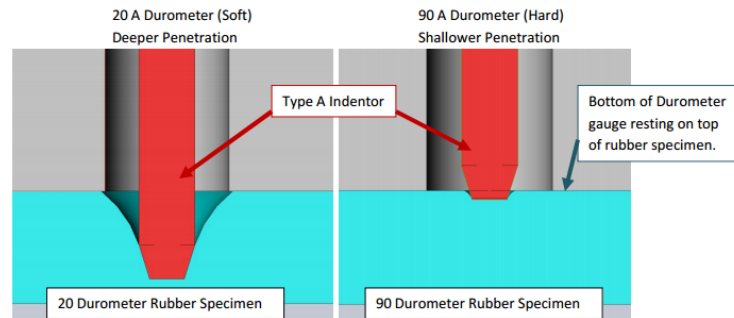


Figure 8.5: Shore A hardness test

The hardness is unfortunately not a measure [33] for the filler content which is known to highly affect the dynamic stiffness and the degree of amplitude dependent behaviour. The next goal is to obtain experimental data of natural rubbers and possibly combine results in a smart manner.

8.3.1. Collecting and Reproducing Experimental Data

In the next part a few experimental results are considered from other relevant research. The obtained material model parameters are used as a first estimate. A few notes have to be made about the data obtained from other research.

- only data of natural rubbers is considered
- the composition of the natural rubbers differs and is in some cases are unknown
- data is reproduced from figures from which differences can occur due to the lack of raw measurement data
- experimental results include both static and dynamic behaviour

In the following a small summation is presented of the relevant data found in literature. After which the data will be reproduced and combined to obtain a first estimate for the static and dynamic behaviour of a natural rubber with a Shore A hardness of 58.

- The work of Ucar and Basdogan [67] presents experimental data for three natural rubbers with a hardness of 45,60 and 75. Hyperelastic and viscoelastic properties can be obtained from the uniaxial tensile test and time domain relaxation tests done in this work.
- Kim et al. [35] presents experimental results for natural rubbers with unknown hardness but known filler content. It differs from the work of Ucar and Basdogan [67] that the focus lies on finding hyperelastic behaviour under compressive conditions and not tension.
- Suphadon et al. [62] presents the hyperelastic behaviour of two natural rubbers that are unfilled.
- Gil-Negrete et al. [26] present material model parameters for two natural rubber with a known Shore A hardness of 50 and 70. The work presents parameters a linear elastic, fractional derivative viscoelastic and the von Mises's elastoplastic material models. The 50 rubber is said to be lightly filled whereas the 70 is filled more. Bushing stiffness are presented as well.
- The work of Olsson and Austrell [51] stated that two rubber of Shore A 60 and 80 show large amplitude dependence which can be mainly ascribed to the Mullins effect. This means that preconditioning min-

imizing the amplitude dependence and therefore the degree of nonlinear viscoelasticity. It presents material parameters for a viscoelastic-elastoplastic model.

- The work of Luo et al. [40] presents material model parameters for the Kraus model of a filled NR. More on the Kraus model parameters for filled NR can be found in the work of Chazeau et al. [14].
- The book of Roylance [58] presents the time domain relaxation data of a natural rubber type. This is by far the most complete data but is needed to be transformed to the frequency domain.

(Hyper)elastic

In both the experiment and the FE analysis the applied displacement is held small. Also the preloading resulting from the attached structures will not trigger the hyperelastic behaviour. This means that hyperelastic behaviour is not necessary to be modelled. The focus in this work lies on determining good initial viscoelastic material model parameters.

The hardness is an indirect measure of the stiffness and therefore it can be related to the Young's Modulus (E). The Young's moduli is a good indicator for low frequency viscoelastic behaviour. The hardness measurement is determined after 15 seconds at which for example the relaxation process of the natural rubber in the work of Roylance [58] is already at 95%. Therefore the storage modulus at very low frequency should match the Young's modulus when the same loading conditions apply. It is assumed that the loss modulus is zero for low frequency which is correct behaviour for natural rubbers.

The following semi-empirical relations are found in literature which relate the Shore A hardness with the Young's Modulus;

$$E = \frac{0.0981(56 + 7.62336S)}{0.137505(254 - 2.54S)} \quad (8.1)$$

$$S = 35.22735 + 18.75487 \ln(E) \quad (8.2)$$

which are derived by Gent and by Rigbi respectively. Gent stated that below a Shore A of 40 the experimental results started to differ from the semi-empirical formula. Battermann and Kohler derived an empirical formula which relates the Shore A hardness to the shear modulus:

$$G = 0.86(1.045^S) \quad (8.3)$$

The following Young's moduli and shear modulus are found:

$$E_{\text{Gent}} = \frac{0.0981(56 + 7.62336S)}{0.137505(254 - 2.54S)} = 3.3314 \quad [\text{MPa}] \quad (8.4)$$

$$E_{\text{Rigbi}} = \exp\left(\frac{S - 35.22735}{18.75487}\right) = 3.3677 \quad [\text{MPa}]$$

$$G_{\text{Kohler}} = 0.86(1.045^S) = 11.047 \quad [\text{MPa}] \quad (8.5)$$

It is shown that both relations (Eq. 8.4) from Gent and Rigbi provide near identical results. As mentioned in Section 2.1 the elastic modulus is proportionally to the shear modulus by $E = 3G$ for an incompressible material. For a filled rubber the factor can become up to 4 [12]. From Equation 8.6 it can be seen that one of the relations are defined for minor filled natural rubbers. Because filler content is unknown these result provide a good first estimate of the static modulus.

$$\frac{G_{\text{Kohler}}}{E_{\text{Rigbi}}} = 3.28 \quad (8.6)$$

Viscoelastic

Roylance [58]

The work obtained the Prony series in the time domain for a natural rubber with unknown composition. The

Prony parameters are presented in Table B.1 with M_e being 0.3. The Prony series are in this case used to represent the time domain relaxation behaviour. The relaxation modulus is defined as:

$$M(t) = M_e + \sum_{i=1}^N M_i e^{-t/\tau_i} \quad (8.7)$$

The Prony series obtained through time domain experiments can be used to obtain the frequency dependent behaviour as is shown by Baumgartl, M., Winter [7]. The Prony formulae [17] for the storage and loss modulus are being used:

$$M'(\omega) = M_\infty + \sum_{i=1}^N \frac{\bar{g}_i (\tau_i^2 \omega)^2}{1 + (\tau_i^2 \omega)^2} \quad (8.8)$$

$$M''(\omega) = \sum_{i=1}^N \frac{\bar{g}_i \tau_i \omega}{1 + (\tau_i^2 \omega)^2} \quad (8.9)$$

where \bar{g}_i refers to M_i and $M_\infty = M_e$.

Gil-Negrete et al. [26]

In this work the shear modulus is determined for natural rubbers with four different hardness values; 40, 50, 60 and 70. A near constant shear modulus magnitude is found within a frequency ranging from 0 to 500 Hz. Most deviation from the linear behaviour is observed between 0 and 100 Hz. The following values can be assumed reasonable:

The work also present material model variables from which the behaviour can be extracted. It makes use of the fractional derivative model to represent the nonlinear viscoelastic behaviour:

$$G^* = G_e + \frac{G_{fd} b (i\omega)^\alpha}{G_{fd} + b (i\omega)^\alpha} \quad (8.10)$$

The moduli for the NR without (NR A_) and the two with hardness known (NR A50 and A70) are presented in Figure 8.6. The results are within the same order of magnitude. A large deviation is found in terms of frequency dependent behaviour. Where one loss modulus is decreasing, the other increases. The search therefore continuous for a more consistent dataset which represents frequency dependent behaviour that is expected based on the literature review.

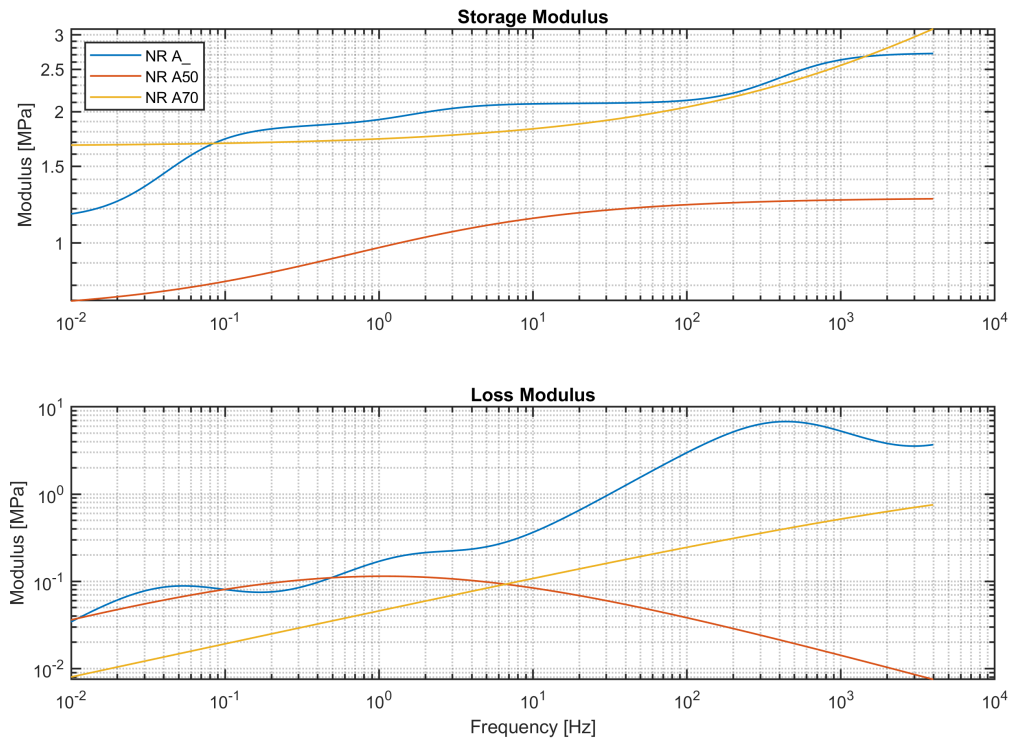


Figure 8.6: Moduli obtained from literature

DMA Dataset

One dataset which fulfils this demands is presented in Figure 8.7. The results are obtained by a DMA which is also executed in the work of Voormeeren [70]. Comparable trends in frequency dependent behaviour is observed. It is expected that the optimization method correct the absolute magnitude of the moduli, but preserves the frequency dependent trend-line. The last DMA measurement is the most complete and direct data. The raw measurement is available from which there are no uncertainties.

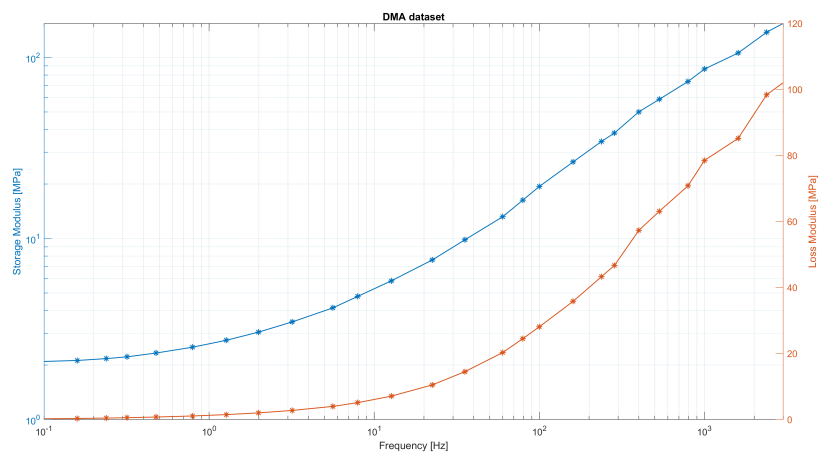


Figure 8.7: DMA data

8.4. Dynamic Simulation

In this section it is presented which steps are taken to fulfil the simulation. More information is presented about both the static and dynamic analysis. Pros and cons are presented for different methods. After the static analysis follows the dynamic one. Within the steady-state dynamic Analysis, Abaqus has multiple options available, namely:

- mode-based method
- subspace-based method
- direct method

The mode-based method is less accurate than the direct and the subspace-based solution, because within the rubber significant material damping is present [Abaqus manual]. Within the mode-based procedure the frequency-dependent behaviour is needed to be modelled with a workaround. It is not advised to use this method because it introduced more uncertainties. This section therefore continues by summarizing the pros and cons of the direct and subspace-based procedure.

In the next part the key features relevant for this work are presented for the two left types of analysis.

Direct solution procedures

- response in terms of physical DOF of the model
- supports frequency-dependent behaviour. Advised to use when viscoelastic material properties must be taken into account.
- more computational expensive with respect to subspace-based steady-state dynamics
- more accurate than subspace-based steady-state dynamics
- includes load stiffness effects
- includes nonlinear effect of a prior response
- can handle nonsymmetric stiffness

Subspace-based procedure

- cost-effective way to include frequency-dependent effect such as damping from viscoelasticity
- linearised response of a system to harmonic excitation
- eigenfrequency extraction step is needed prior to the steady-state dynamic analysis
- less accurate than direct solution method, in particular when dealing with viscoelasticity with a high loss modulus

Because this work is focussed on optimization, the accuracy of the simulation is crucial for finding correct optimized parameters. Both approaches are able to handle viscoelastic behaviour. The subspace-based procedure is however less accurate because it is a modal superposition procedure. The subspace-based method also depends on an eigenfrequency analysis prior to the dynamic simulation. *It is because of these facts that the direct solution method is chosen for this work.*

8.4.1. Data Processing

To obtain the dynamic stiffness, the displacement is used as the input for the FE model. The output are all the reaction forces measured at both VPs. The dynamic stiffness is also referred to as the impedance and is defined by:

$$\text{Impedance: } Z_{mn}(\omega) = \frac{f_m(\omega)}{u_n(\omega)} \quad u_{k \neq n} = 0 \quad (8.11)$$

which relates the applied displacement u at DoF n to a reaction force f at DoF m . An element Z_{mn} is only nonzero if the displacement in n results in a force in m . The dynamic stiffness matrix is column-wise constructed. To fill column n of stiffness matrix Z , DoF n is activated where the other DoF $m \neq n$ are all held fixed. In this case a displacement is applied to DoF n while all others are fixed and resist movement with a certain reaction force f .

Considering the classical method for obtaining the dynamic stiffness than the dynamic stiffness has a sparse character. The surrounding nodes are fixed due to conditioning and can therefore not transfer forces to other DoFs. By applying the virtual point method within the numerical environment, a reduction is made. Using this method also enables us to compute the admittance matrix as describes in Equation 8.12. Obtaining the

receptance is proven to be difficult with the classical method due to the inversion of a sparse impedance matrix.

$$\text{Receptance: } Y_{mn}(\omega) = \frac{u_m(\omega)}{f_n(\omega)} \quad f_{k \neq n} = 0 \quad (8.12)$$

The order in DoF during this work is:

$$m \text{ and } n = \begin{bmatrix} 1 \\ 2 \\ 3 \\ 4 \\ 5 \\ 6 \\ 7 \\ 8 \\ 9 \\ 10 \\ 11 \\ 12 \end{bmatrix} = \begin{bmatrix} f_{x_{vp1}} \\ f_{y_{vp1}} \\ f_{z_{vp1}} \\ M_{x_{vp1}} \\ M_{y_{vp1}} \\ M_{z_{vp1}} \\ f_{x_{vp2}} \\ f_{y_{vp2}} \\ f_{z_{vp2}} \\ M_{x_{vp2}} \\ M_{y_{vp2}} \\ M_{z_{vp2}} \end{bmatrix} \text{ and } \begin{bmatrix} T_{x_{vp1}} \\ T_{y_{vp1}} \\ T_{z_{vp1}} \\ R_{x_{vp1}} \\ R_{y_{vp1}} \\ R_{z_{vp1}} \\ T_{x_{vp2}} \\ T_{y_{vp2}} \\ T_{z_{vp2}} \\ R_{x_{vp2}} \\ R_{y_{vp2}} \\ R_{z_{vp2}} \end{bmatrix}^T \quad (8.13)$$

where $T_{x_{vp1}}$ is the translation in x-direction of virtual point 1. The magnitude and phase of the dynamic stiffness are calculated with Equation 8.14 and 8.15 respectively.

$$|Z_{mn}| = \frac{|f_m|}{|u_n|} \quad (8.14)$$

$$\angle Z_{mn} = \angle f_m - \angle u_n \quad (8.15)$$

8.5. Quality of results

The research object is symmetric in multiple loading directions. The symmetry of the object results in a weak link between applied displacement and some measured reaction forces. The weak link between particular DoF makes these stiffness values sensitive for numerical noise. The obtained phase is found to be more sensitive than the magnitude. Equation 8.16 is used to define the relative magnitude of the complete transfer-stiffness matrix. The measure can indicate which stiffness values are sensitive for numerical noise and are preferable not used for comparison to the experimental results. The normalization is separated in four blocks such that the translational, rotational and cross stiffness values are normalized separately. The results of Equation 8.16 are presented in Figure 8.8. The same result are found for the drivingpoint- and transfer-stiffness matrices. The dark blue boxed indicate the DoF with a strong link. These stiffness values are expected to be of a good quality such that they can be compared to the experimental results. To summarize to following DoF with strong links are found:

- Translational Stiffness: Z_{T_x, T_x} , Z_{T_y, T_y} , Z_{T_z, T_z}
- Rotational Stiffness: Z_{R_x, R_x} , Z_{R_y, R_y} , Z_{R_z, R_z}
- Cross Stiffness: Z_{R_y, T_x} , Z_{T_x, R_y} , Z_{R_x, T_y} , Z_{T_y, R_x}

$$\text{Normalized stiffness magnitude} = \begin{bmatrix} \frac{Z_{(T/T)_{x,y,z}}}{\max(Z_{(T/T)_{x,y,z}})} & \frac{Z_{(R/T)_{x,y,z}}}{\max(Z_{(R/T)_{x,y,z}})} \\ \frac{Z_{(T/R)_{x,y,z}}}{\max(Z_{(T/R)_{x,y,z}})} & \frac{Z_{(R/R)_{x,y,z}}}{\max(Z_{(R/R)_{x,y,z}})} \end{bmatrix} \quad (8.16)$$

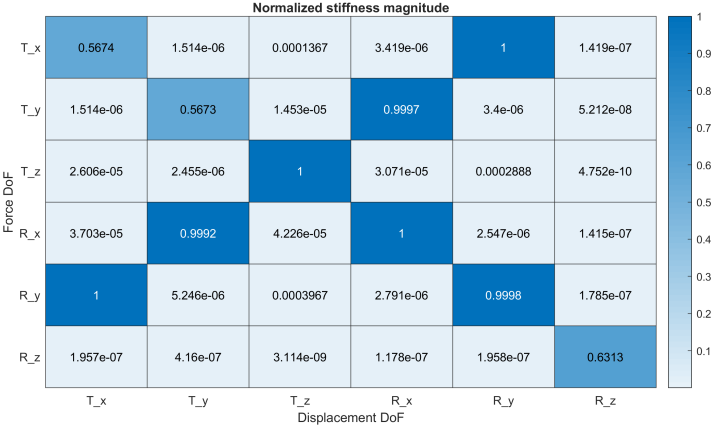


Figure 8.8: Absolute and normalized dynamic transfer stiffness value

9

Experimental

This chapter hold all the information with respect to the experiment. In Section 9.1 the case is introduced and the experimental approach is presented in an overview. The measurement approach is presented in section 9.2. The equipment necessary to conduct the measurement are then presented in 9.3. Before presenting the experimental results two models are used to derive a transferfunction which provides a first validation tool. These models are presented in Section 9.4. With this validation tool ready the experimental results are ready to be presented and analysed in Section 9.5.

9.1. Introduction

The goal for this experiment is to characterize the dynamic behaviour of the *AIB*-structure, where *A* and *B* are the crosses and *I* is the rubber vibration isolator as shown in Figure 9.1. The dynamic behaviour is characterized in terms of the admittance Y which is also referred to as the receptance in literature.

$$\text{Receptance: } Y_{mn}(\omega) = \frac{u_m(\omega)}{f_n(\omega)} \quad f_{k \neq n} = 0 \quad (9.1)$$

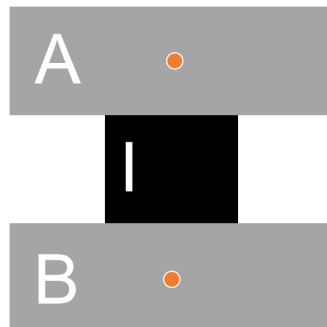


Figure 9.1: Sketch of research object

In this work the impact test method [27, 52, 55, 67] is used for the characterization. Deformation of the object is triggered by the excitation (impact) and acceleration is measured with accelerometers attached on the structure. The impact method has the following advantages:

- multi-DoF characterization
- minimal attached measurement equipment
- enables one to use of the Virtual Point transformation method
- measurement able up to the multi-kHz range
- lean characterization method

Figure 9.2 presents a zoomed view of the experimental setup. The structure hangs in two thin elastic cords which are mounted to a cubed framework. The elastic cords are used to create a so called free-free boundary condition. The elasticity of the cords is chosen such that the decoupling takes place at low frequency (5 Hz). Decoupling means that the motion of the mounted structure is not affected by movement of the frame.

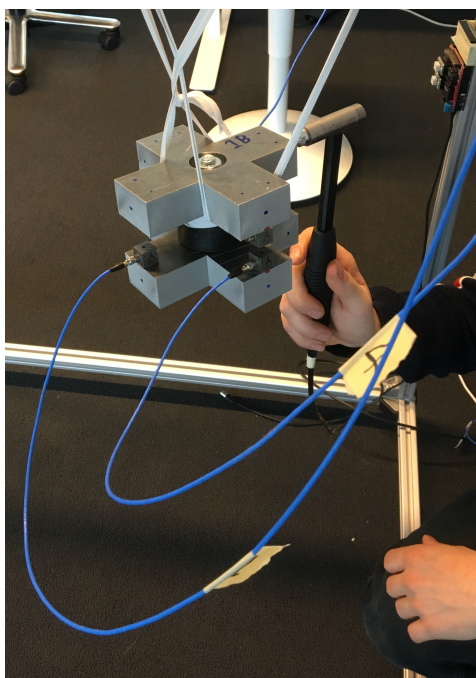


Figure 9.2: Experimental Conditions

9.2. Approach

In this section it is shown how the measurement is executed. At first the workflow during the different experiments is explained. After which it is shown how the data obtained during the experiment is processed with the goal of constructing the 12x12 receptance matrix.

9.2.1. Workflow

The elements of the receptance matrix are filled with the admittance as a function of frequency. The admittance and impedance have an inverse relation. The admittance is more often referred to as receptance in literature. To align with literature in the further work it is referred to as receptance.

Lets first consider which experimental cases needs to be fulfilled in order to fully construct the receptance matrix of the combined *AIB*-structure. As previously mentioned the rubber is mounted in between two transmission simulators (TS). The structure must move freely which enables one to compute the cross values of the receptance matrix. It is therefore that the structure is mounted with a so called free-free boundary condition.

The experiment has to be done with sensors located at both TS 1 and 2. A minimal of 2 three-axial accelerometers and 1 one-axial accelerometer are needed to fully characterize the movement of one transmission simulator as describes by [68]. Because the sensor module is limited to 12 channels, not both TSs can be adopted with sufficient sensors. For a series of impacts the movement of only one TS can be fully characterized. The measurement has to be fulfilled in a roving manner ¹, in which position of impacts and sensors vary during the experiment.

For the experimentally characterized receptance, the following relation between sensor and impact location

¹It is shown by Van Der Seijs [69] that the admittance FRF is always an observation of the structure's dynamics independent of the other FRFs in the measurement. This enables one to spread the matrix construction over a multiple of experiments. Why this is particularly useful in this work is further defined in Section 9.3.3.

can be derived:

$$\begin{bmatrix} u_{1,x} \\ u_{1,y} \\ u_{1,z} \\ r_{1,x} \\ r_{1,y} \\ r_{1,z} \\ u_{2,x} \\ u_{2,y} \\ u_{2,z} \\ r_{2,x} \\ r_{2,y} \\ r_{2,z} \end{bmatrix} = \begin{bmatrix} \text{Impact at TS 1} \\ \text{Sensor at TS 1} \\ \\ \text{Impact at TS 1} \\ \text{Sensor at TS 2} \end{bmatrix} \begin{bmatrix} \text{Impact at TS 2} \\ \text{Sensor at TS 1} \\ \\ \text{Impact at TS 2} \\ \text{Sensor at TS 2} \end{bmatrix} \begin{bmatrix} f_{1,x} \\ f_{1,y} \\ f_{1,z} \\ m_{1,x} \\ m_{1,y} \\ m_{1,z} \\ f_{2,x} \\ f_{2,y} \\ f_{2,z} \\ m_{2,x} \\ m_{2,y} \\ m_{2,z} \end{bmatrix} \quad (9.2)$$

As can be seen from Equation 9.2, 4 variations needs to fulfilled during the experiment. By making use of identical TSs and assuming perfect experimental conditions the receptance matrix is symmetric. Due to uncertainties about the structure and the experimental setup it is chosen to fully characterize the receptance matrix and afterwards validate the degree of symmetry.

To summarize, the experiment can be divided into the following steps:

1. Hit impact on TS 1 and measure on TS 1 which results in the drivingpoint-receptance \mathbf{Y}_{11} .
2. Rotate the structure to improve working conditions.
3. Keep the same sensor positions, but now hit the impacts on TS 2. This combination is needed to obtain the transfer-receptance \mathbf{Y}_{12} which relates impacts in VP₂ to displacement in VP₁.
4. Keep the same object orientation, but replace sensors position to TS 2. Hit again impact on TS 2 to obtain the drivingpoint-receptance \mathbf{Y}_{22} of VP₂
5. Rotate the structure to improve working
6. Finally: keep the same sensor positions, but now hit the impacts on TS 1. This combination is needed to obtain the transfer-receptance \mathbf{Y}_{21} which relates impact on VP₁ to displacement in VP₂.

With now all the data obtained, the next goal is to optimize the measurement by selecting the best available data.

9.2.2. Data selection

This optimization holds impact selection for improved coherence, but also making small sensor adjustments to improve the numerical setup in order to match the imperfect experimental conditions. To data selection mostly done within Dirac. The data selection consists of the following steps:

- **During the experiment**
 1. Validate *impact force consistency*, which prevent observing non-linearities of the rubber.
 2. Observe the force spectrum to detect *double pulse impacts*
 3. Observe coherence of sensor channels parallel to the impact. Coherence performance around anti-resonance frequencies is proven to be a good indicator of *consistent impact positioning*.
 4. Observe coherence of sensor channels perpendicular to the impact. Coherence performance over the range of frequency is proven to be a good indicator of *consistent impact directioning*.
- **After the experiment**
 1. Check the symmetry (reciprocity) of the obtained VP receptance matrix.

9.2.3. Data Processing

The data obtained from the experiment needs to be processed. The goal is to obtain the 12x12 dynamic stiffness matrix which relates forces and moments to displacements and rotations respectively between two points of interest.

To create some background knowledge the following matrix forms are often used:

$$\text{Accelerance: } A_{ij}(\omega) = \frac{\ddot{u}_i(\omega)}{f_j(\omega)} \quad f_{k \neq j} = 0 \quad (9.3)$$

$$\text{Mobility: } M_{ij}(\omega) = \frac{\dot{u}_i(\omega)}{f_j(\omega)} \quad f_{k \neq j} = 0 \quad (9.4)$$

$$\text{Receptance: } Y_{ij}(\omega) = \frac{u_i(\omega)}{f_j(\omega)} \quad f_{k \neq j} = 0 \quad (9.5)$$

In an experimental setup the acceleration is being determined. The time domain signal is transformed to the frequency domain within the Dirac software. Transforming the obtained time domain signal to the frequency domain makes it easy to compute the receptance or mobility matrix from the accelerance. The fact that: $\ddot{\mathbf{u}}(\omega) = j\omega\dot{\mathbf{u}}(\omega)$ and $\ddot{\mathbf{u}}(\omega) = -\omega^2\mathbf{u}(\omega)$ is useful for computing the other matrices. With the accelerance determined from the experiment, the receptance and mobility can be determined by:

$$\text{Mobility: } Y_{ij}(\omega) = \frac{\dot{u}_i(\omega)}{f_j(\omega)} = \frac{1}{j\omega} \frac{\ddot{u}_i(\omega)}{f_j(\omega)} = \frac{-j}{\omega} \frac{\ddot{u}_i(\omega)}{f_j(\omega)} \quad f_{k \neq j} = 0 \quad (9.6)$$

$$\text{Receptance: } Y_{ij}(\omega) = \frac{u_i(\omega)}{f_j(\omega)} = \frac{1}{-\omega^2} \frac{\ddot{u}_i(\omega)}{f_j(\omega)} \quad f_{k \neq j} = 0 \quad (9.7)$$

The receptance is derived from the experimentally obtained accelerance by:

$$Y_{ij}(\omega) = \frac{1}{-\omega^2} \frac{\ddot{u}_i(\omega)}{f_j(\omega)} = \frac{1}{-\omega^2} A_{ij}(\omega) \quad f_{k \neq j} = 0 \quad (9.8)$$

The dynamic stiffness is now determined by:

$$\mathbf{Z}_{\text{exp}}(\omega) = \mathbf{Y}_{\text{exp}}^{-1}(\omega) \rightarrow \begin{bmatrix} Z_{11} & Z_{12} \\ Z_{21} & Z_{22} \end{bmatrix} = \begin{bmatrix} Y_{11} & Y_{12} \\ Y_{21} & Y_{22} \end{bmatrix}^{-1} \quad (9.9)$$

Not all data is proven to be useful as a reference for the optimization. It is shown by Haeussler et al. [27] that:

$$\mathbf{Z}_{12}^I = \mathbf{Z}_{12}^{AIB} \quad \text{and} \quad \mathbf{Z}_{21}^I = \mathbf{Z}_{21}^{AIB} \quad (9.10)$$

which means that the transfer stiffness of the combined structure *AIB* characterizes the behaviour of the rubber element only. This enables one to obtain a matrix that is comparable to the numerical results. It is chosen to invert the receptance matrix of the experiment. By doing so, the coupling between the structures is taken into account. Therefore no further knowledge has to be developed about the coupling dynamics of the experimental structure.

9.3. Equipment

In this section the equipment used during the experiment are defined. This includes measurement equipment as well as additional features. The individual properties of the measurement equipment can be found in Appendix B.3.

9.3.1. Transmission Simulators

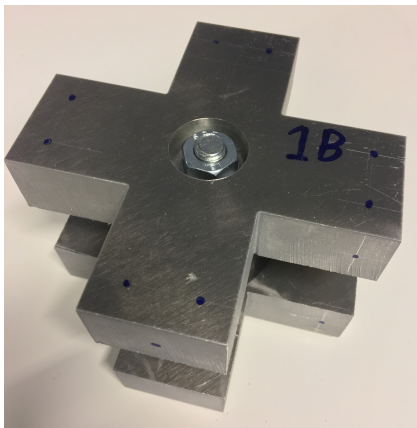
In the experimental setup the use of a transmission simulators (TS) is introduced. Vibrations excited with the impact hammer are to quickly damped out due to the characteristics of the rubber material. It affects the measurement in a negative way. To overcome this problem more mass is added in the form of a TS which enables us to insert and hold more energy in the system which improves experimental results when a rubber object is considered. A TS must;

- be very stiff, to not affect the measurement with its own dynamic character,
- have enough mass to hold a minimum amount of energy during the measurement considering a certain frequency range,
- have flat surfaces which can be hit easily with an impact hammer and to which accelerometers can be attached.

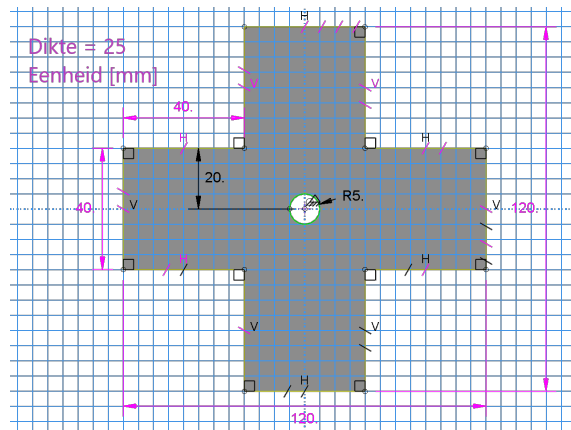
- be able to be connected to the rubber object and mounting frame.

The TS is attached to the top and bottom of the rubber cylinder and one is also attached to the mounting frame. In this work an aluminium cross is used to function as a TS. The fabricated TS and sketch are shown in Figure 9.3a and 9.3b respectively. The reasoning behind the aluminium crosses are:

- **Material choice:**
 - Easier to process than steel.
 - Lighter than steel
 - Stiff
- **Shape choice:**
 - Large enough surface for good impact
 - Effective shape to minimize mass and increase surface.
 - The arms of the cross enables one to apply significant torque with an impact and get higher sensor output for rotations. Therefore the rotational stiffness is better measured.



(a) Fabricated TS



(b) Sketch

Figure 9.3: Transmission Simulator

9.3.2. Excitation

In this work the structure is excited with an impact hammer. An example of a range of impact hammer can be seen in Figure 9.4.



Figure 9.4: Range of impact hammers

Experience has learned that position and direction of the impact must be as consistent as possible. A few critical points need to be considered when measuring with the impact method;

- **Positional accuracy:**
 - Not every impact can hit the exact same location. Errors in position leads to less accurate FRFs as shown

in Appendix C.1. In particular the anti-resonance is highly affected. It is therefore crucial to compare the results of multiple FRFs for one impact position and thereby focussing on the anti-resonance regions.

- **Directional accuracy:**

Not every impact can be hit in the correct direction which is usually perpendicular to the impact surface. A directional error highly affects the cross-measured FRFs as can be seen in Appendix C.2. The FRFs obtained by sensor channels perpendicular to the impact are a good indicator for directional errors.

- **Double Pulse:**

If the structure it hit two times with one impact this is called a double pulse. The double pulse is characterized by a ripple in the force spectrum. The obtained FRF is unusable.

- **Force Dependency:**

In this work it is also important to be consistent in terms of impact force. Linear material behaviour is assumed, but different behaviour can be triggered if impact forces differentiate too much from each other. Impact force must be as small as possible to not trigger motions of a magnitude that results in nonlinear rubber behaviour.

- **Hammer tip:**

The choice of hammer tip is a compromise between the observed frequency range and the impact force. For a wide frequency range a sharp shaped impulse is needed. However this sharp impulse stands for a high force which can result in sensor overshoot [11].

9.3.3. Sensors

This section describes the sensors used in this experiment. To fully define the dynamics of a virtual point a minimum of 6 translational accelerations needs to be measured. As shown by van der Seijs et al. [68] this cannot be fulfilled with two tri-axial accelerometers. The DoF in line with the two sensors is left unmeasured which results in an underdetermined transformation matrix. A third accelerometer must be attached in order to fully characterize the motion of the Virtual Point. Three tri-axial accelerometers are mounted at one transmission simulator as shown in Figure 9.2. The properties of each sensor can be found in appendix B.3.



Figure 9.5: PCB Accelerometer

The PAK hardware can handle up to 12 sensor channels. Unfortunately this makes it impossible to fully characterize the dynamics of the two virtual points in one measurement. Using a limited amount of sensors means that the measurement needs to be fulfilled in a roving manner. More on this is found in section 9.2.1.

- **Positioning:**

- Placement of sensors is always a compromise.
- Sensors must be placed in an area around the virtual point which behaves rigid.
- The sensors will often be placed as far away from the virtual point as possible. This sensor placement results in higher magnitude output for rotations leading to low Signal to Noise Ratio (SNR).
- The sensors cannot be placed at locations where you want to impact the structure. Also placing the sensor close to an impact can quickly lead to sensor overshoot.

- **Mass-loading:**

- Mounting the sensors to the structure adds mass. With $m_{\text{sensor}} = 5.4$ [g] and $m_{\text{TS}} = 525$ [g], means that one sensor adds $\approx 1\%$ of mass.

- **Mounting (wax):**

- Easy removable

- Mechanically filters out high frequencies that could risk exciting an accelerometer's internal resonance²
- Can easily get loose from a small touch.
- Alignment on surface is harder due to the thicker layer of adhesive in comparison to loctide.
- Limited temperature range of application

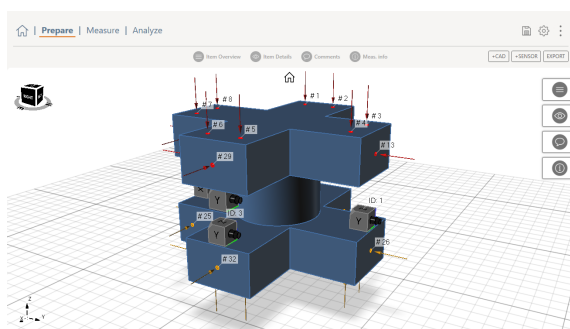
Because the measurement is done in a roving method, the removability of the sensors are important. Also the temperature is held around room-temperature which makes the adhesive method applicable for this experiment.

9.3.4. Dirac Software

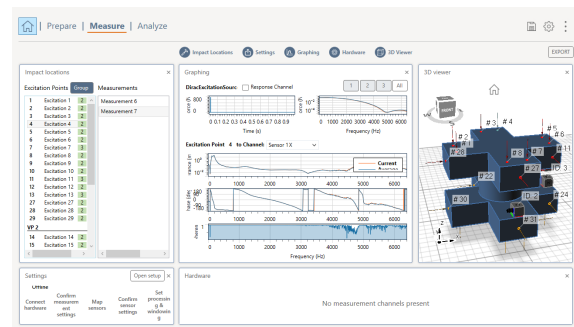
The experiment is prepared with the Dirac software provided by Vibes.technology. This great piece of software enables one to prepare the full experiment in a virtual environment. Dirac enables us to:

- load a 3D model of the object,
- position impacts, sensors and virtual points on the object,
- assign impact and sensor to a virtual point,
- measure and check experimental results in terms of magnitude and phase of the FRF,
- optimize a set of impacts by removing the worst coherence impact combinations,
- check for double pulses and force consistency,
- export FRFs and properties of the instrumentation which can be handled by the Vibes toolbox.

The prepare and measure module are presented in Figure 9.6a and 9.6b respectively.



(a) Prepare module



(b) Measure module

Figure 9.6: Dirac Software

9.4. Validation models

In this section a method is defined to validate the result presented in 9.5. The first goal is to determine the reasonability of the obtained results. This is done by comparing the receptance with that of a simplified systems as presented in Figure 9.7a. Two models are being derived:

- A *base model* which is very simplified and assumes perfect free-free boundary conditions
- An *experimental model* which again is very simplified but now included elements which are representing imperfect experimental conditions

The simplified models are able to give a good first approximation of expected results. The base model used to define results that are not affected by experimental boundary conditions. The experimental model is used to give insights into how the elastic mounting can affect the measurement. The knowledge prevents one to apply optimization to affected experimental results.

From both models the transfer functions can be derived. The magnitude and phase of these models can be used to validate the drivingpoint- and transfer-receptance obtained with the experiment.

The simplifications for both models are that:

²<https://blog.mide.com/accelerometer-mounting-best-practices-for-vibration-measurement>

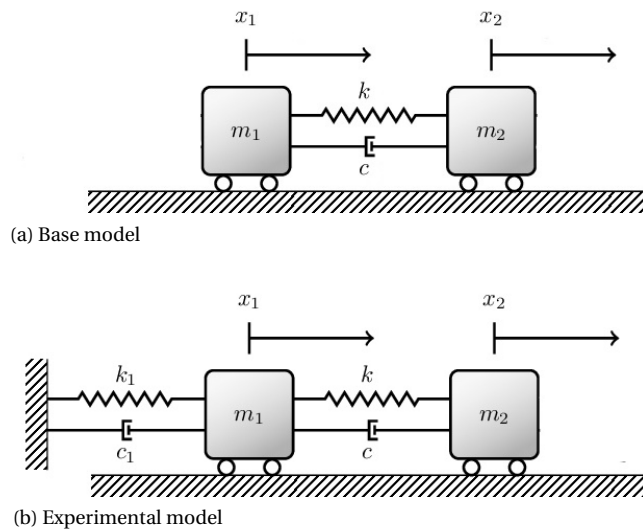


Figure 9.7: Schematic view of simplified models. The force F is applied to the left of m_1 .

- mass of rubber element is ignored
- stiffness and damping are not frequency dependent
- crosses behave rigidly (point-mass)

At first the Equations of Motion (EoM) of the system are defined in Table 9.1. The transfer function, in the Laplace domain, of the models can be derived from the EoM. These describe the individual drivingpoint- and transfer receptance.

Table 9.1: EoM for both models

Base model	$x_1(s)(m_1 s^2 + cs + k) = F(s) + x_2(s)(cs + k) \quad (9.11)$ $x_2(s)(m_2 s^2 + cs + k) = x_1(s)(k + cs) \quad (9.12)$
Experimental model	$x_1(s)(m_1 s^2 + (c + c_1)s + (k + k_1)) = F(s) + x_2(s)(cs + k) \quad (9.13)$ $x_2(s)(m_2 s^2 + cs + k) = x_1(s)((c + c_1)s + (k + k_1)) \quad (9.14)$

Drivingpoint-receptance:

The drivingpoint-receptance is defined as:

$$Y_{11,22}(s) = \frac{x_1(s)}{F_1(s)} \quad (9.15)$$

which can be obtained by replacing the irrelevant x_2 in Equation 9.11:

$$Y_{11,22}^{\text{base}}(s) = \left((m_1 s^2 + cs + k) - \frac{(cs + k)^2}{m_2 s^2 + cs + k} \right)^{-1} \quad (9.16)$$

Writing the transfer function in one fraction it is found that:

$$Y_{11,22}^{\text{base}}(s) = \frac{m_2 s^2 + cs + k}{(m_1 m_2) s^4 + (m_1 + m_2) cs^3 + (m_1 + m_2) ks^2} \quad (9.17)$$

The Bode plot of the drivingpoint-receptance is presented in Figure 9.8. The behaviour is characterized as follows, which can be used to quantify the results from the experiment:

- A slope of -2 before and after resonance frequency
- A factor difference between high and low frequency behaviour as described by equations 9.22 and 9.23.
- Interesting point is: $|Y(\omega = 1)| = \frac{1}{2m}$

The drivingpoint-receptance of the experimental model is now defined as:

$$Y_{11,22}^{\text{exp}}(s) = \frac{m_2 s^2 + cs + k}{m_1 m_2 s^4 + (m_1 + m_2)cs^3 + (m_1 k + m_2 k + m_2 k_e)s^2 + ck_e s + kk_e} \quad (9.18)$$

The FRF of the experimental model can be seen in Figure 9.8. After the first resonance frequency the structure is decoupled from its mounting. After the second resonance the two masses A and B are being decoupled.

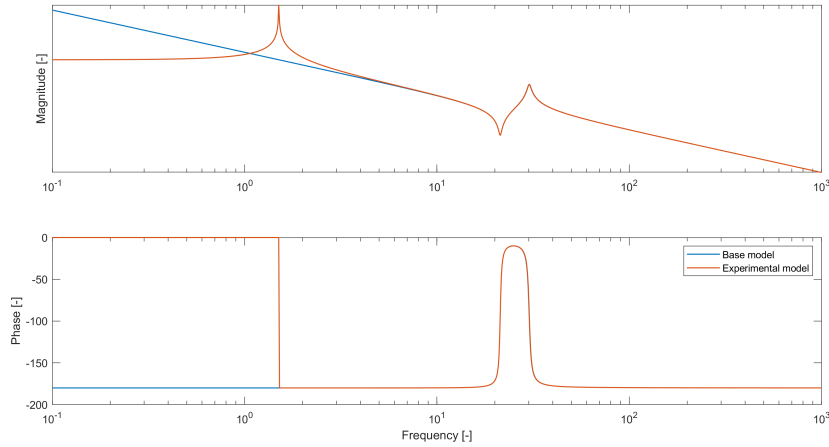


Figure 9.8: Drivingpoint-receptance of both models

Transfer-receptance:

The next goal is to redo the previous, only now for the transfer receptance $Y_{21,12}$. Again the simplified models presented in Figure 9.7a and 9.7b are being analysed. The EoM presented in Table 9.1 are used to obtain the transfer-functions.

The transfer-receptance is defined as:

$$Y_{12,21}(s) = \frac{x_2(s)}{F_1(s)} \quad (9.19)$$

which can be obtained by replacing the irrelevant x_1 in Equation 9.12 and writing the transfer function in one fraction it is found that:

$$Y_{12,21}^{\text{base}}(s) = \frac{cs + k}{m_1 m_2 s^4 + (m_1 + m_2)cs^3 + ((m_1 + m_2)k + c)s^2} \quad (9.20)$$

The transfer-function for the experimental model can be obtained by replacing the irrelevant x_1 in equation 9.13 and writing the transfer function in one fraction it is found that:

$$Y_{12,21}^{\text{exp}}(s) = \frac{cs + k}{m_1 m_2 s^4 + (m_2(c + c_e) + m_1 c)s^3 + (m_2(k + k_e) + m_1 k + cc_e)s^2 + (ck_e + c_e k)s + kk_e} \quad (9.21)$$

The bode plot of the transfer-receptance for both models is presented in Figure 9.9.

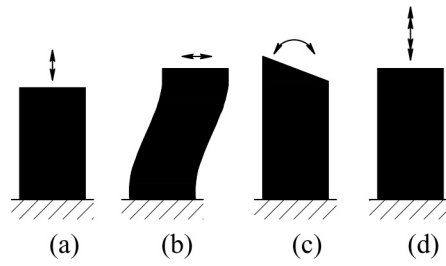


Figure 9.10: Modes of deformation [8]: (a): T_z , (b): $T_{x,y}$, (c): $R_{x,y}$, (d): R_z

9.5.1. Drivingpoint Receptance

The drivingpoint receptance magnitude and phase are presented in Figures 9.11 and 9.12 respectively. The receptance is obtained from accelerance by applying Equation 9.7. The diagonal terms are plotted for a first analysis of the obtained results as shown in Equation 9.30.

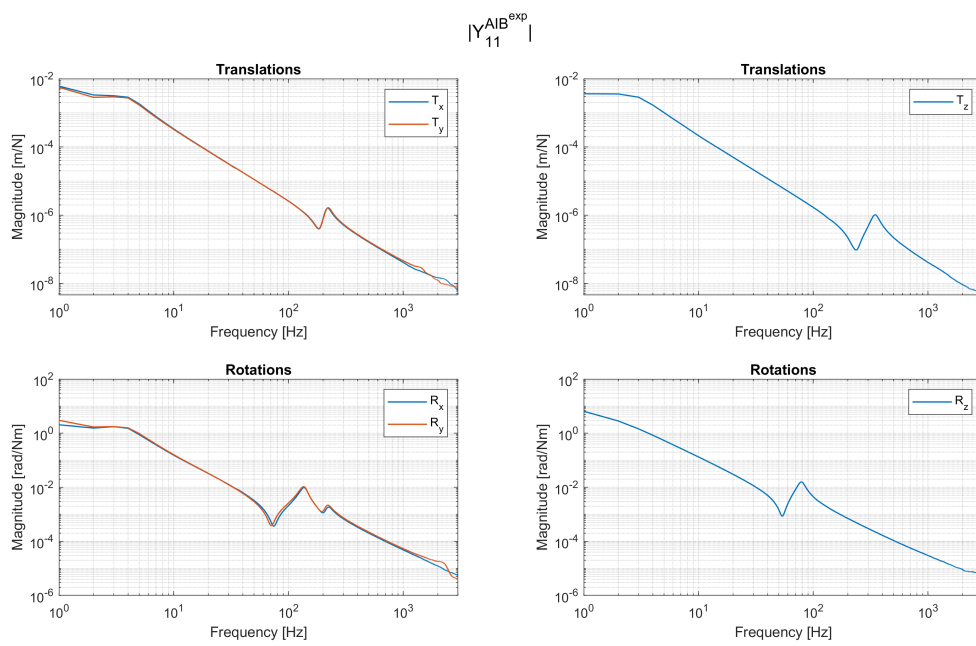


Figure 9.11: Magnitude of Drivingpoint-receptance

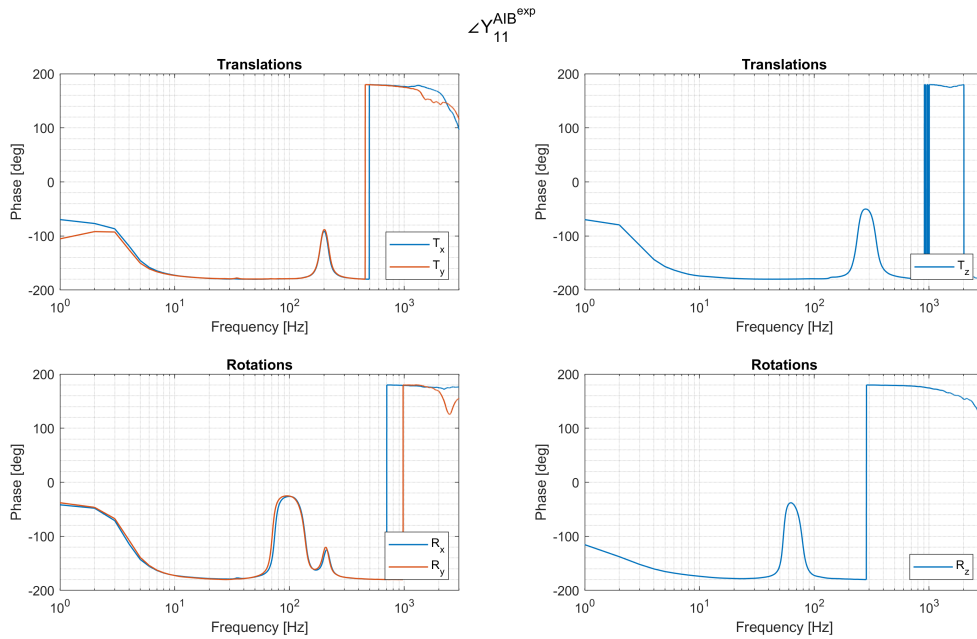


Figure 9.12: Phase of Drivingpoint Receptance

Observations:

1. $T_x \approx T_y$ and $R_x \approx R_y$.
2. The magnitudes show a slope of -2 before and after the (anti-)resonance region.
3. The high frequency mass-line is a factor higher than the low frequency mass-line.
4. Near zero Hertz, all but R_z shows flattening behaviour for the magnitude. At the same frequency the phase starts to go from $\approx -180^\circ$ to $\approx 0^\circ$.
5. An additional anti-resonance is observed for R_x and R_y . The anti-resonance is located at the same frequency region as where the (anti-)resonance is present in T_x and T_y .
6. (Anti-)resonances peaks are rather flat.
7. Minor deviation in magnitude and phase for the symmetric values (T_x, T_y and R_x, R_y).

Physical Explanation:

1. The AIB-structure is symmetric with respect to the x- and y-axis. The receptance in ($T_x \approx T_y$), and around ($R_x \approx R_y$) these axis are therefore expected to be equal. The experimental results confirms the symmetry assumption.
2. The -2 slope is a character of the mass-line in the frequency domain^a. Before and after the (anti-)resonance region the dynamics are dominated by the mass of the two crosses. It can also be declared with high and low frequency behaviour shown by Equation 9.22 and 9.23 respectively.
3. The factor-difference between the two mass-lines can be explained by uncoupling of the two masses. After the resonance frequency the motion of mass 2 is uncoupled from mass 1. This makes it easier to excite mass 1 resulting in a higher valued receptance. It can also be declared with high and low frequency behaviour shown by Equation 9.22 and 9.23 respectively which show a factor 2 difference with the same slope.
4. At low frequency unwanted stiffness and damping are interfering with the structure dynamics. The stiffness and damping are introduced by the elastic cords. The effect is best observed in direction of the elastic cords (T_z). The effect is least observed for R_z because this rotation is perpendicular to the elastic cords. The low frequency difference can be explained by the low frequency of the experimental model presented in Equation 9.28.
5. It shows there is a clear coupling present between the individual DoF.
6. The flat peaks are a result of damping within the structure. The damping is obviously introduced by the rubber material.

7. The high frequency difference can be clarified with the fact that the dynamics of the crosses comes into play. The virtual points dynamics of the aluminium cross is presented in Figure 9.13. Above 3000 Hz the first resonance frequency of the cross is observed at the separate measurement. To simplify matters, the results are therefore observed up to 3000 Hz. Up to this frequency it is reasonable to assume the crosses behave rigidly.

^a<https://ocw.tudelft.nl/wp-content/uploads/4.DynamicsofMotionSystems.pdf>

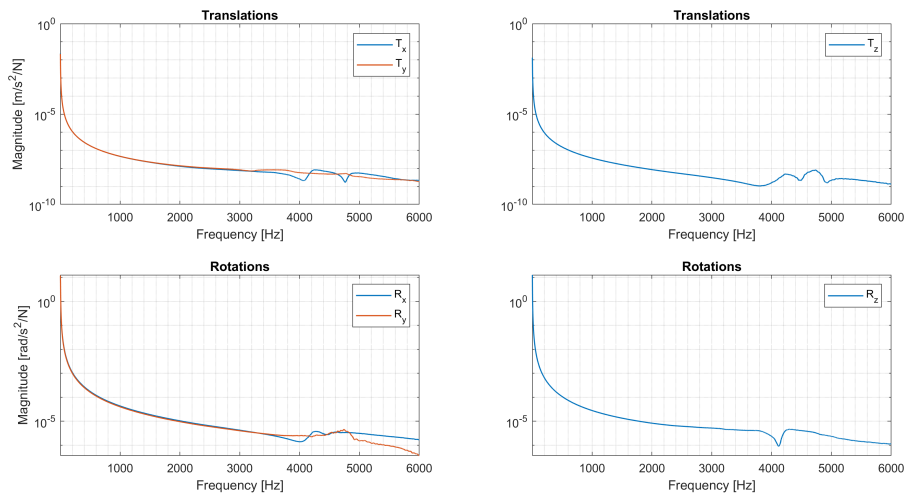


Figure 9.13: Receptance Magnitude of the cross

9.5.2. Transfer Receptance

In this section the experimental results for the transfer receptance Y_{21} are presented. The magnitude and phase of the diagonal terms of Y_{21} are shown in Figure 9.14 and 9.15 respectively.

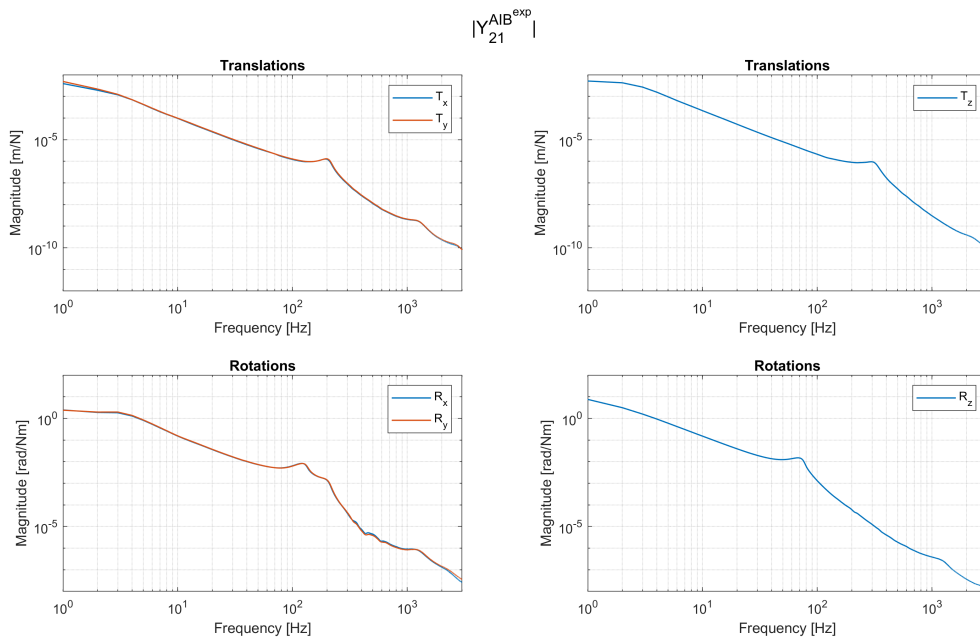


Figure 9.14: Magnitude of Transfer Receptance

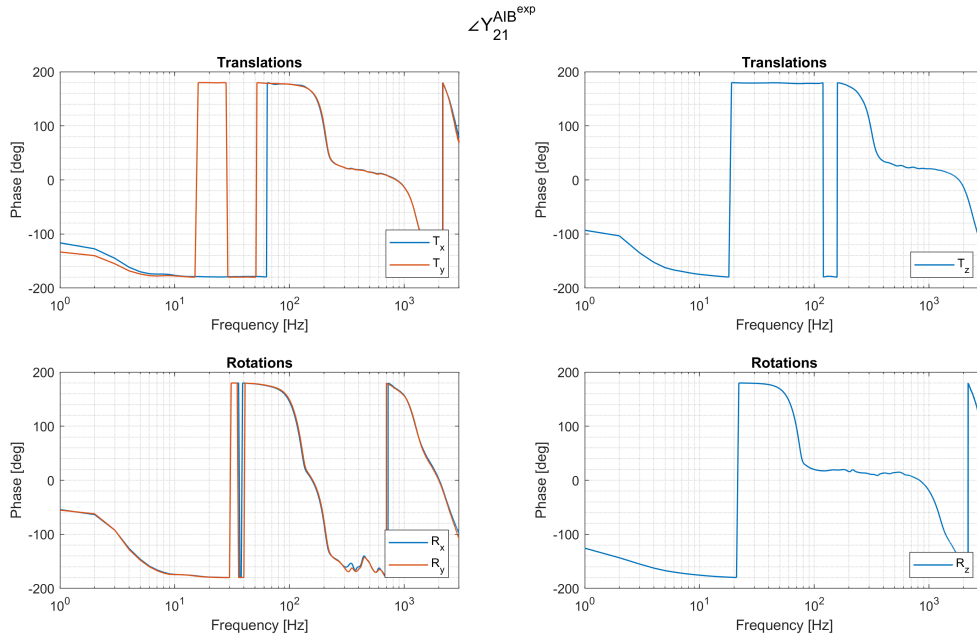


Figure 9.15: Phase of Transfer Receptance

Observations:

1. $T_x \approx T_y$ and $R_x \approx R_y$.
2. The magnitudes show a slope of -2 before and -3 after the (anti-)resonance region.
3. Near zero Hz, all but Y_{R_z} shows flattening behaviour for the magnitude. At the same frequency the phase starts from $\approx -180^\circ$ to $\approx 0^\circ$.
4. Closely located resonance frequencies of $R_{x,y}$, at ≈ 130 and ≈ 200 Hz.

Physical Explanation:

1. Expect due to geometrical symmetry of the object.
2. Decoupling of the two masses after the (anti-)resonance region.
3. As previously shown this affect is caused by the mounting for which elastic cords are being used.
4. The second resonance frequency is also observed for $T_{x,y}$. One can relate to the tension side of the deformation mode where as the other is a result of the compression side.

9.5.3. Transfer-Stiffness

In this section the results for the transfer stiffness's are presented. The transfer stiffness is obtained by inverting the experimentally obtained receptance. A more in-depth view is presented in Section 10.2.1. In general it can be said that the results are very consistent. Up to 600 Hz $R_{x,y}$ shows behaviour which does not compare to the other results. The results are not observed for the comparable DoF of the receptance matrix. It can be said that the behaviour is a consequence of the matrix inversion.

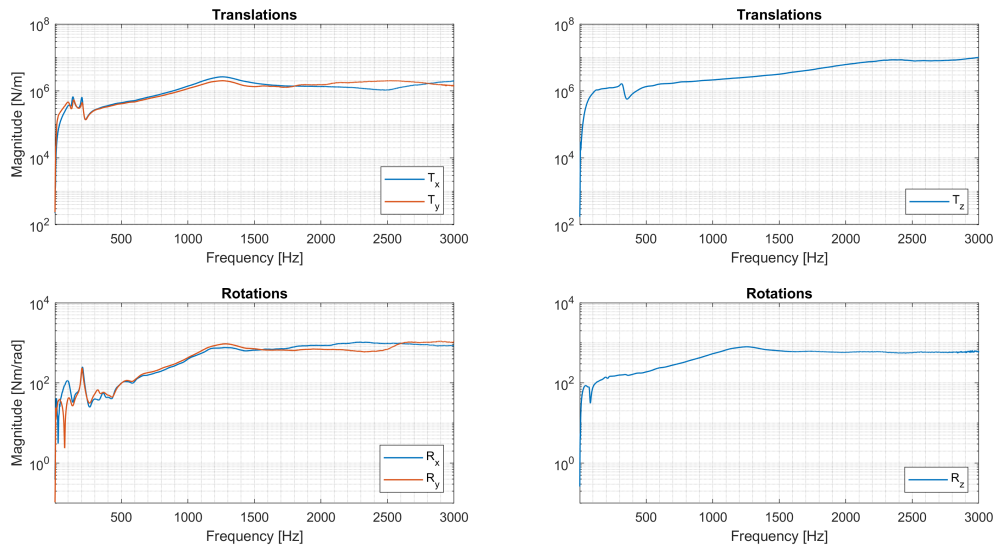


Figure 9.16: Magnitude of Transfer-Stiffness

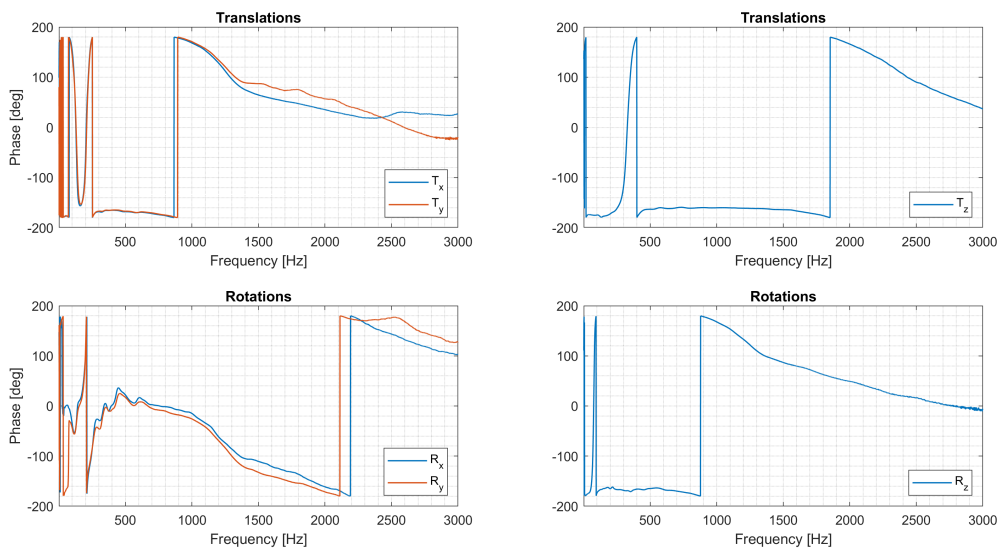


Figure 9.17: Phase of Transfer-Stiffness

9.5.4. Drivingpoint-Stiffness

To complete the presentation of the experimental results the drivingpoint-stiffness is presented. The results for the magnitude and phase of the drivingpoint stiffness are presented in Figure 9.18 and 9.19 respectively. A more in-depth view on the drivingpoint-stiffness is found in Section 11.2.

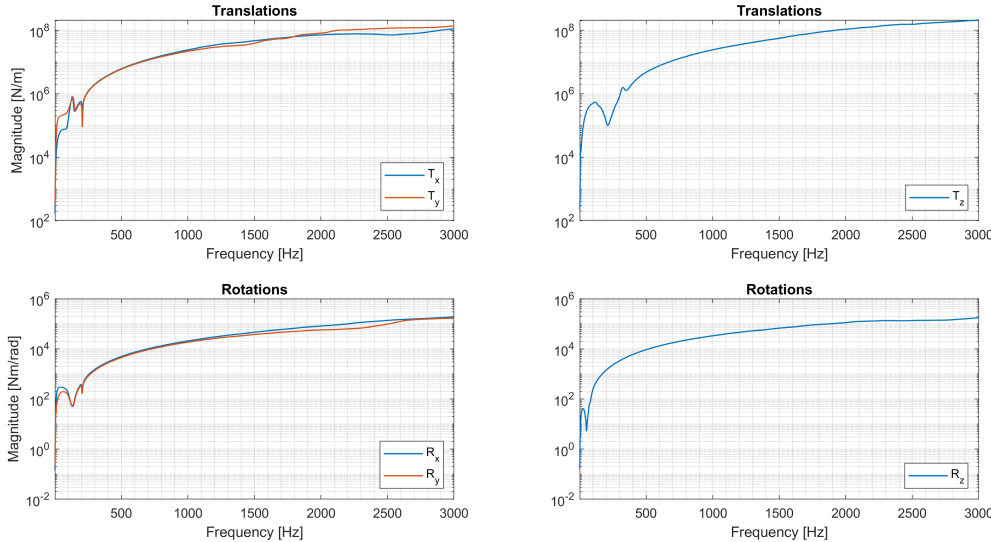


Figure 9.18: Magnitude of Drivingpoint-Stiffness

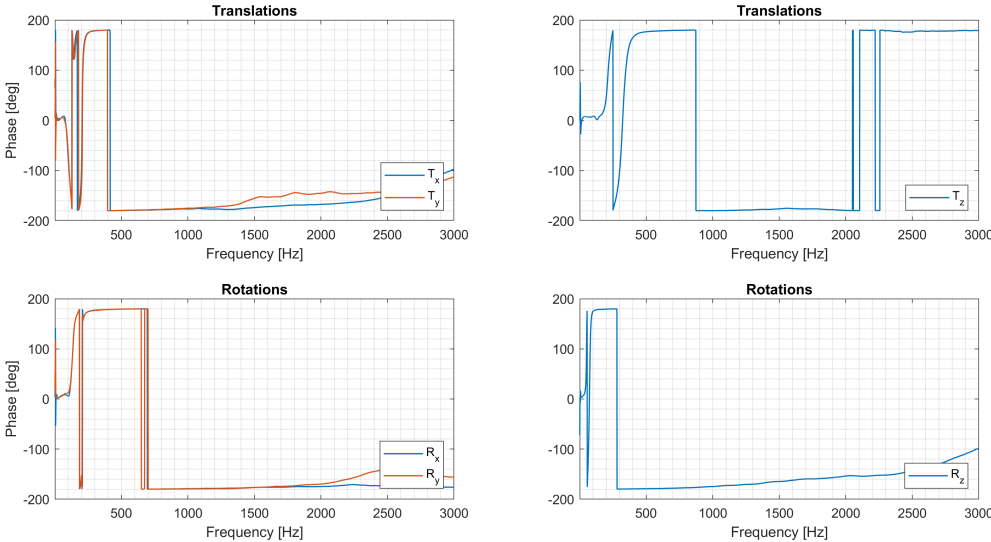


Figure 9.19: Phase of Drivingpoint-Stiffness

10

Material Model Optimization

Section 10.1 goes more in detail on the optimization method and which experimental data is used as a reference. Finally in Section 10.2 the results for the optimized moduli and transfer-stiffness are presented. The results are compared to the benchmark test which is done with the initial material data.

10.1. Optimization approach

In this section the used optimization method is further defined. First it is presented which material parameters are optimized. After this the used error function is presented which is used for the afterwards presented optimization function. Finally it is presented which elements of the stiffness matrix are used for the optimization.

10.1.1. Material model parameters

In the FE model a viscoelastic material model is used. For the initial viscoelastic data is obtained from a Dynamic Mechanical Analysis from other research, as presented in Section 8.3. In the DMA the storage and loss moduli are obtained. The DMA data is translated to tabular data which can be handled by Abaqus as a viscoelastic input. Tabular data is chosen because it enables one to apply point-wise optimization instead of considering the whole frequency range as other material models such as Prony series require. The tabular input is obtained by Equation 10.1 where G_s , G_l and G_∞ are the storage, loss modulus and infinite modulus. The infinite modulus describes the near static behaviour of the rubber.

$$\begin{aligned}\omega\text{RE}(g) &= \frac{G_l}{G_\infty} \\ \omega\text{IM}(g) &= 1 - \frac{G_s}{G_\infty}\end{aligned}\tag{10.1}$$

Although Equation 10.1 is a bit misleading, the dominant dependency of the dynamic stiffness with respect to the moduli values is as follows;

$$\begin{aligned}\text{RE}(\mathbf{Z}) &= f(G_s, G_\infty) \\ \text{IM}(\mathbf{Z}) &= f(G_l, G_\infty)\end{aligned}\tag{10.2}$$

which results in:

$$\mathbf{Z}^* = f(G_s, G_l, G_\infty)\tag{10.3}$$

The long term shear modulus is determined by making use of the rubber hardness. Relations are found in literature as presented in Section 8.3. Using the relation of Kohler to obtain the shear modulus results in:

$$G_\infty = 0.86(1.045^S) = 11.047 \text{ [MPa]}\tag{10.4}$$

10.1.2. Optimization method and objective function

In this work the Matlab optimization tool *surrogateopt* use being used. The Surrogate optimization is a global solver for time-consuming objective functions. The solves searches for a global minimum within the range of the bounded inputs G_s and G_l . The storage and loss shear modulus represent the rubber material properties. The solver is capable of handling nonsmooth objective functions as expected in this work.

The used error function is an addition to the RMSE function. In this work it is found that the optimization tool performs best when separating real and imaginary parts. The error functions for both are combined to come up with the following error function:

$$J(G_s, G_l) = \frac{1}{n} \sqrt{(\text{Re}(Z_n) - \text{Re}(Z_e))^2} + \frac{1}{n} \sqrt{(\text{Im}(Z_n) - \text{Im}(Z_e))^2} \quad (10.5)$$

where Z_n and Z_e are the numerical and experimental stiffness and n is the number of obtained data points.

A coarse material model optimization is applied. The moduli must behave in a continuous manner with respect to frequency as shown in Section 2.3.1. Interpolation is applied to obtain material data in between the obtained points. The approach consist of a coarse optimization at every $n \cdot 250$ Hz, with a maximum frequency of 3000 Hz. Leading to 13 optimized points.

10.1.3. Stiffness matrix element selection

The complete dynamic stiffness matrix consists of 144 elements. Using all elements means that numerically also all transfer stiffness values need to be obtained. The required number of simulation is defined as:

$$\#_{\text{sim}} = c \cdot i \quad (10.6)$$

where i is the number of iterations of the optimization and c is the number of columns of \mathbf{Z} that is required. To reduce the optimization time it is chosen to use one transfer stiffness value to be optimized. The first goal is to minimize the number of reference values. The chosen stiffness values must be;

- relative easy to extract from experimentally obtained receptance matrix \mathbf{Y}
- least sensitive to experimental measurement errors
- least affected by the inversion of receptance matrix \mathbf{Y}

It is known that the driving point stiffness is affected by the mass that is attached to the structure in the experimental setup. For obtaining the drivingpoint-stiffness \mathbf{Z}_{11}^I from \mathbf{Z}_{11}^{AIB} complex decoupling methods are needed which depend on the dynamic stiffness of the attached structures. Because these complex methods are beyond the scope of this research, the driving point stiffness (\mathbf{Z}_{11}^{AIB} and \mathbf{Z}_{22}^{AIB}) is not used for reference.

The transfer stiffness ($\mathbf{Z}_{12} = \mathbf{Z}_{21}$) is known not to be affected by the attached structures. The transfer stiffness can be obtained from the experimental results in a direct manner known as inverse substructuring[73]. The experimental results can be inverted as mentioned previously: The dynamic stiffness is now determined by:

$$\mathbf{Z}(\omega) = \mathbf{Y}(\omega)^{-1} \quad (10.7)$$

As in the work of Haeussler et al. [27], Relation 10.8 is used to obtain a comparable measure. It relations states that the experimentally obtained transfer-stiffness does not on the properties of the attached structures. This indirectly means the experiment is directly comparable to the numerical model in which these masses are not incorporated.

$$\mathbf{Z}_{12}^{I_{\text{num}}} = \mathbf{Z}_{12}^{AIB_{\text{exp}}} \quad \text{and} \quad \mathbf{Z}_{21}^{I_{\text{num}}} = \mathbf{Z}_{21}^{AIB_{\text{exp}}} \quad (10.8)$$

The goal is to further reduce the number of transfer stiffness elements. The cross stiffness values are located in the off-diagonal elements of the transfer stiffness matrix. These stiffness values are typically hard to determine in an experimental fashion. The cross stiffness values are most vulnerable for measurement errors such as;

- minor directional impact errors

- sensitivity of accelerometers (high signal-to-noise ratio)
- orientational placement error of accelerometers

As aforementioned the diagonal terms have a strong link and are therefore least sensitive to measurement errors. The most trustworthy stiffness values are therefore the diagonal values of \mathbf{Z}_{21}^{AIB} consisting of three translations and three rotations. These values are also known as the direct transfer stiffness. These six stiffness values give a good reference with respect to the numerical values.

$$[Z_{Tx} \quad Z_{Ty} \quad Z_{Tz} \quad Z_{Rx} \quad Z_{Ry} \quad Z_{Rz}] \quad (10.9)$$

The large dynamic stiffness matrix originally contained 144 elements. With the previous analysis these are reduced to the 6 most qualified stiffness values that are to be used as reference values for the error function.

10.2. Results

In this section the results are presented for the material model optimization process. At first the optimized transfer-stiffness is presented after which the new moduli values are presented and evaluated.

10.2.1. Benchmark

In this section the initial numerical and the experimental results are compared. The transfer-stiffness matrix is used as a relative measure. The main goal of this is to define how the initial material model parameters perform within the numerical model. The performance is analysed with respect to the diagonal terms of the transfer-stiffness. These are proven to be the most trustworthy elements of the stiffness matrix. Figure 10.1 and 10.2 show the magnitude and phase for the translations and rotations.

$$\mathbf{Z}_{21} = \begin{bmatrix} T_x & & & & & \\ & T_y & & & & \\ & & T_z & & & \\ & & & R_x & & \\ & & & & R_y & \\ & & & & & R_z \end{bmatrix} \quad (10.10)$$

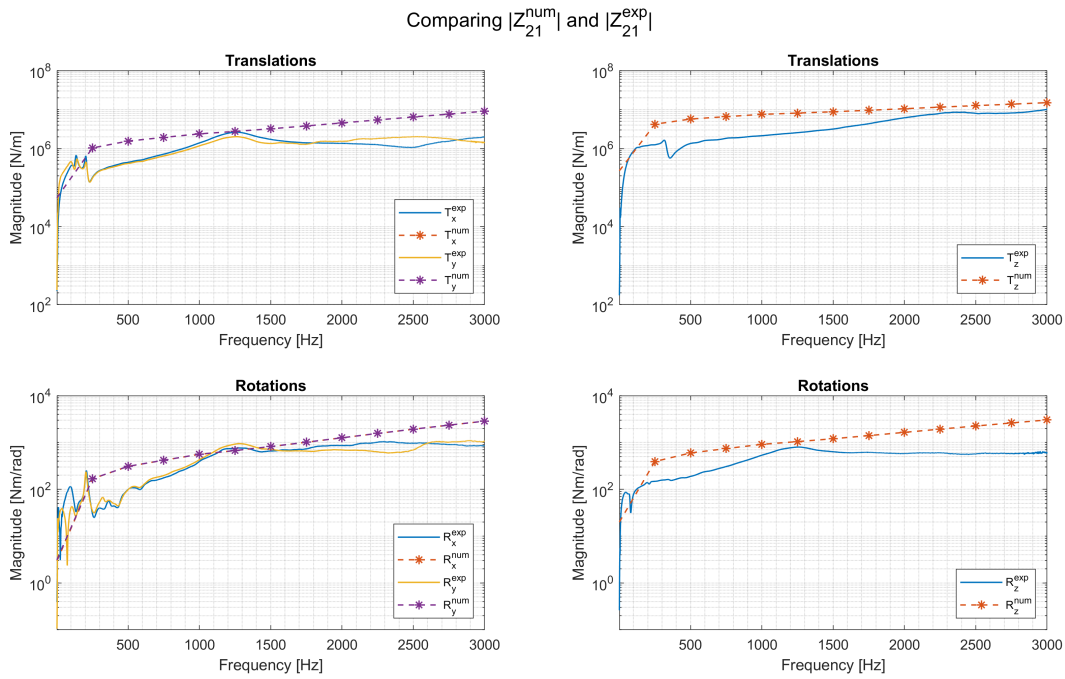


Figure 10.1: Numerical results obtained with the initial material data

Observations $\angle Z_{21}$:

1. In general the moduli are expected to be overly stiff.
2. In the observed frequency range $|Z_{21}^{\text{num}}|$ increases to much at higher frequencies.
3. Due to symmetry $|T_x^{\text{num}}| \equiv |T_y^{\text{num}}|$ and $|R_x^{\text{num}}| \equiv |R_y^{\text{num}}|$

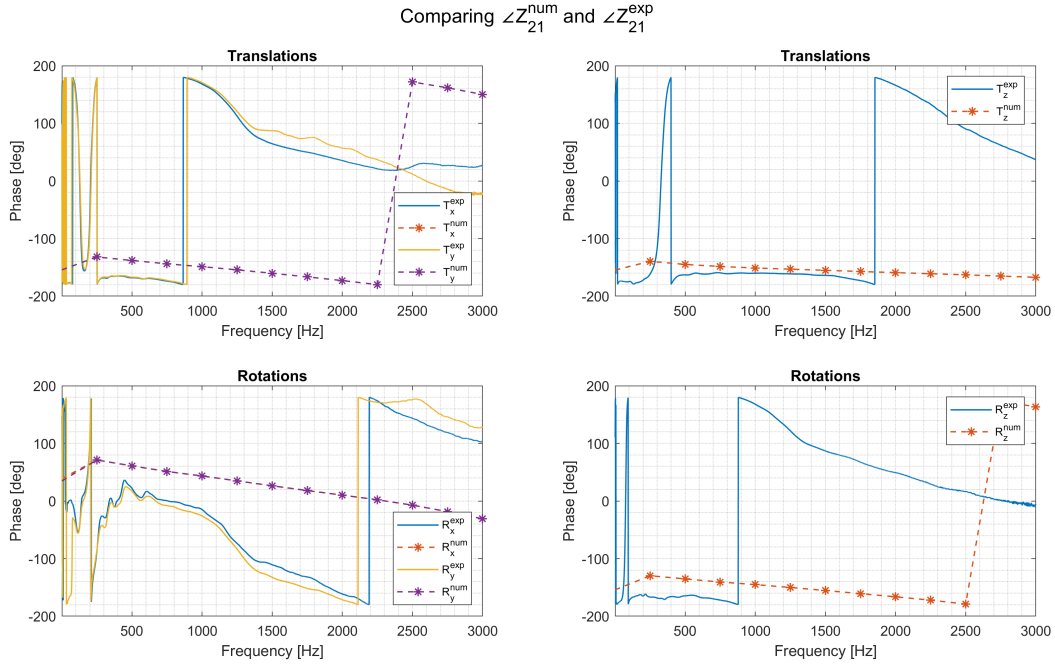


Figure 10.2: Numerical results obtained with the initial material data

Observations $\angle Z_{21}$:

1. In general the numerical phase shows large deviation from experimental results. Deviation in the phase indicates a wrong aspect ratio between the storage and loss modulus.
2. Due to symmetry $\angle T_x^{\text{num}} \equiv \angle T_y^{\text{num}}$ and $\angle R_x^{\text{num}} \equiv \angle R_y^{\text{num}}$

It is shown that the used moduli in general is too high. In the next section it is shown how the optimization method is applied.

10.2.2. Optimized Transfer-stiffness

In this section it is presented how the optimization performs at the individual frequency points. The optimized moduli are used for again comparing numerical and experimental results. The simulations are executed at the same frequency points at which the optimization is done. The moduli are found with an optimization that used the diagonal transfer-stiffness T_x^{exp} as a reference value. The results are again presented in terms of the magnitude and phase of the dynamic transfer-stiffness. The presented results in Figure 10.3 and 10.4 show that the numerical model is significantly improved with respect to the initial model.

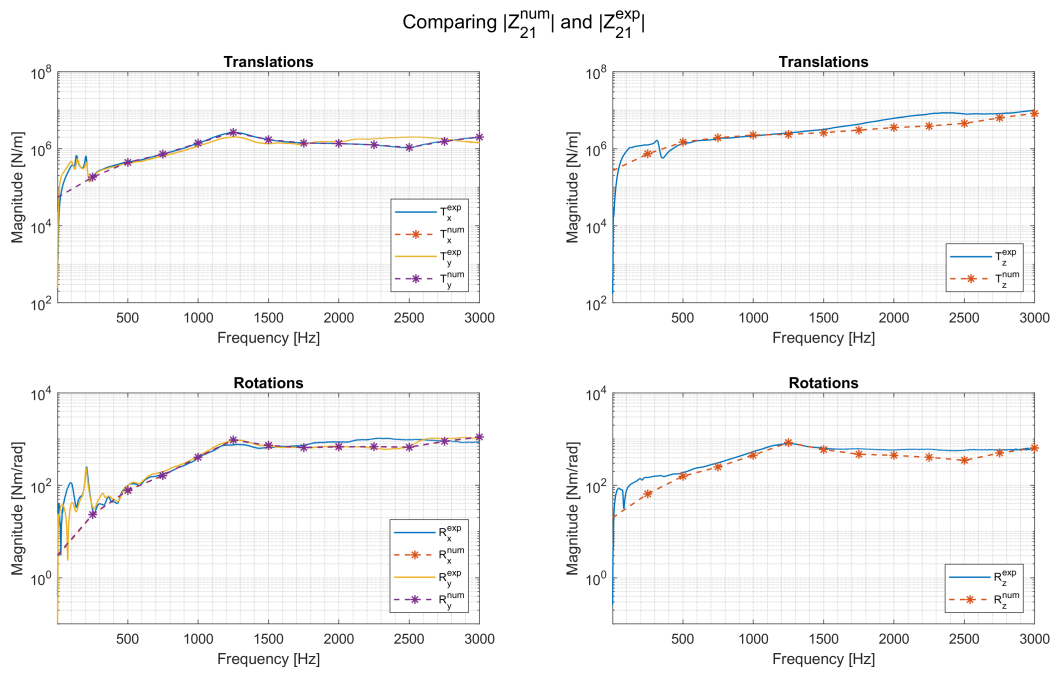


Figure 10.3: Optimized material model performance with respect to the experimental values of $|Z_{21}|$

Observations $|Z_{21}|$:

1. The optimized moduli significantly improves $|Z_{21}^{\text{num}}|$. In general T_x^{num} , T_y^{num} and R_x^{num} outperform T_z^{num} and R_z^{num} .
2. The reference stiffness T_x^{exp} , used for optimization, has a stiffness decrease at 2500 Hz. Optimization point "250 Hz" is located at the resonance frequency. The optimized moduli adapts to these situations which results in an offset in the other stiffness values. Using a second optimization with respect to T_y^{exp} , or the average of T_x^{exp} and T_y^{exp} , is expected to improve overall performance.
3. Optimizing the moduli with respect to T_x^{exp} leads to a perfect prediction of R_y^{num} . Observing the results and due to geometric symmetry the same relation is expected between T_y^{exp} and R_x^{num} .

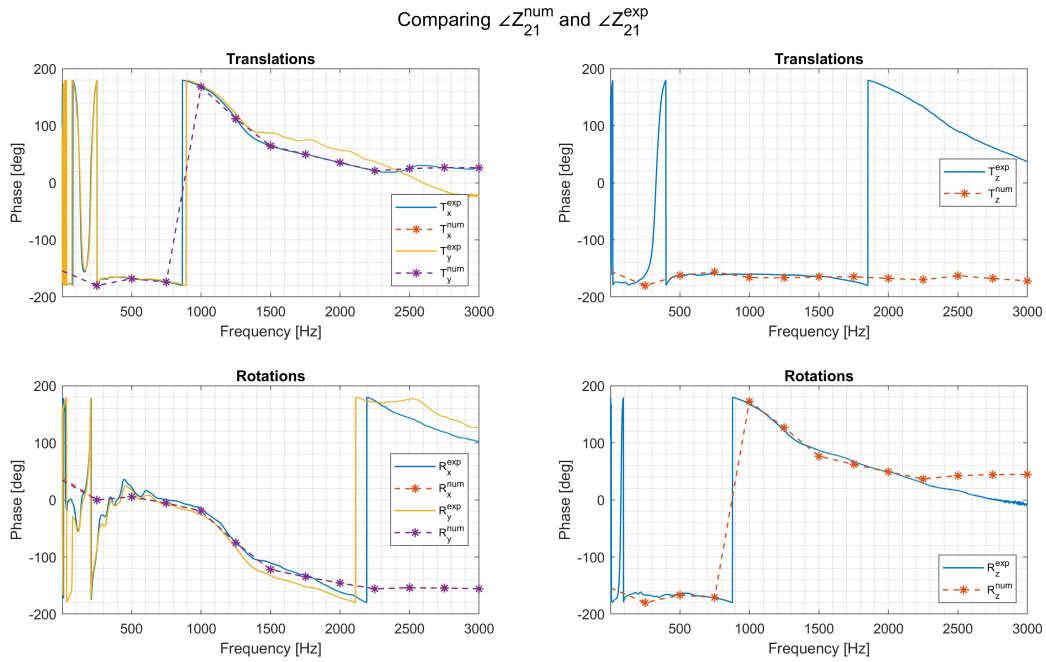


Figure 10.4: Optimized material model performance with respect to the experimental values of $\angle Z_{21}$

Observations $\angle Z_{21}$:

1. The optimized moduli significantly improves $\angle Z_{21}^{num}$.
2. The phase perfectly follows the reference value $\angle T_x^{exp}$.
3. After $f \approx 2250$ Hz the phase of T_x^{exp} is decreasing less than T_y^{exp} . Therefore T_x^{num} , R_x^{num} and R_y^{num} lacking the phase flipping around this frequency.
4. Again optimizing with respect to an average of T_x^{exp} and T_y^{exp} is expected to improve the performance of the other stiffness values.

10.2.3. Optimized moduli

It is previously shown that the optimization method is able to adept to the experimental results. The optimization values used to come to these results are further analysed. The moduli as a function of frequency are presented in Figure 10.6. The figure also presents the final error of the objective function J . The 0 Hz point is not used because the experimental results are affected by the imperfect experimental conditions.

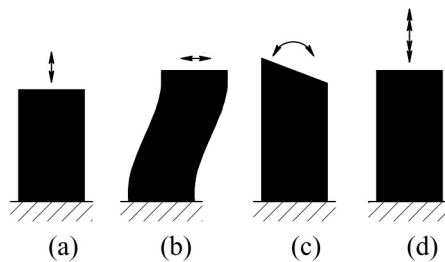


Figure 10.5: Modes of deformation [8]: (a): T_z , (b): $T_{x,y}$, (c): $R_{x,y}$, (d): R_z

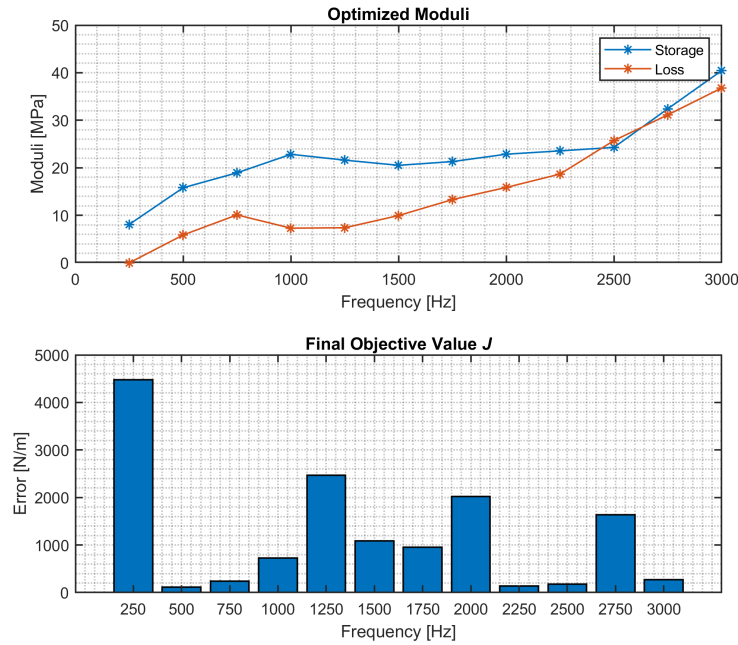


Figure 10.6: Optimized storage and loss modulus $G_{s,l}^{\text{opt}}$ with respect to T_x

Observations $G_{s,l}^{\text{opt}}$:

1. The gradient of the storage modulus behaves as in found in literature and previously described in Section 2.3.1.
2. In Equation 8.5 a static shear modulus of $G_{\infty} \approx 11$ MPa is determined that should correspond to the hardness value of the rubber. The lowest optimization point is at 250 Hz in which $G_{\infty} \equiv G_s = 8.08$ MPa is found. The difference can be declared by the fact that the optimization point is located at the resonance frequency of the rubber object. The modulus is therefore underestimated.

It is shown that the optimization method is able to generate a reasonable optimized viscoelastic material model. The performance is proven to be promising. In the next chapter the optimization is validated by making use of the drivingpoint-stiffness obtained by both the experiment and numerically.

10.3. Improvements

In this section the performance of the applied optimization is analysed. The coherence function is used to compare numerical and experimental results. In Figure 10.7a and 10.7b the coherence of the dynamic transfer-stiffness is presented for the initial and optimized moduli respectively.

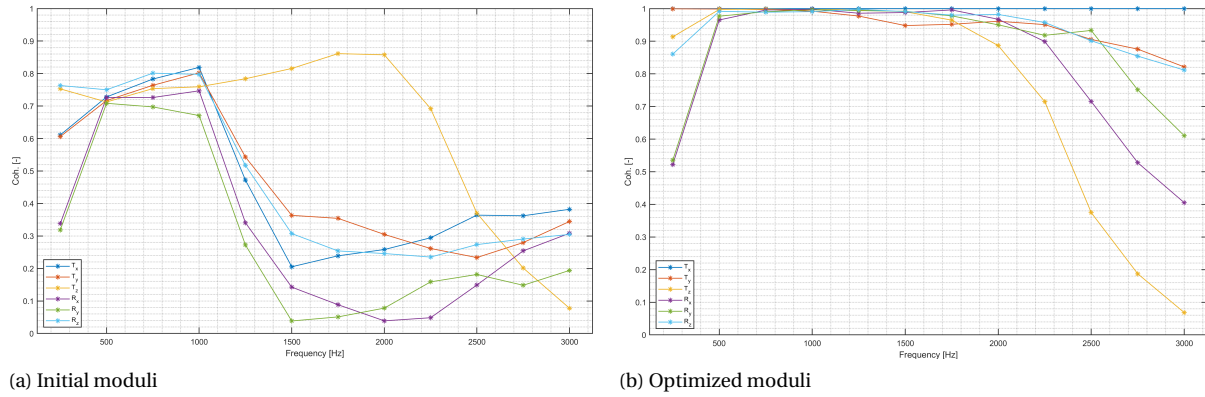


Figure 10.7: The coherence used as a optimization performance measure

Observations:

1. The best improvement is observed for DoF T_x for which the material model is optimized.
2. In general all coherences are improved by the optimization.
3. Mid frequency region is largely improved by the optimization.
4. DoF T_z significantly differs from the others. As previously mentioned T_z is most affect by the elastic mounting. The high frequency coherence of this specific DoF is the only one that is not improved.

Validation

In this section the validation process is presented. It is first needed to update the original FE model. In section 11.1 the additions to the original FE model are presented. With the FE model ready the validation is presented in Section 11.2. In this section the performance of the optimized material model is validated with respect to experimental results. The chapter concludes with Section 11.3 in which all the results for the separate rubber object are obtained.

11.1. Model update

The numerical model is changed to match experimental conditions. In this work the drivingpoint-stiffness is to be used as the validation measure. With the original FE model the numerical and experimental driving-point results are not comparable:

$$\mathbf{Z}_{11}^{\text{num}} \neq \mathbf{Z}_{11}^{\text{AIBexp}} \quad (11.1)$$

With the crosses implemented in the FE model one can say that:

$$\mathbf{Z}_{11}^{\text{AIBnum}} = \mathbf{Z}_{11}^{\text{AIBexp}} \quad (11.2)$$

As aforementioned the drivingpoint-stiffness is affected by the dynamic character of the attached structures characterized by its;

- *Mass M*,
Only the inertia has to be modelled in order to mimic the dynamic character within an acceptable margin up to the first resonance frequency of the transmission simulator.
- *Stiffness K*
The dynamic behaviour of the cross structure is previously shown in Section 9.5.1. In this section it is emphasized that the crosses are behaving rigid up to 3000 Hz.
- *Damping C*
The damping of aluminium[42] is proven to be minor especially with respect to the damping introduced by the rubber.

It enables one to represent the cross as a point mass located within the virtual point as shown in Figure 11.1a and 11.1b. The FE simulation uses the controlled displacement as an input. No precaution has to be taken with respect to triggering non-linearities due to the added mass.

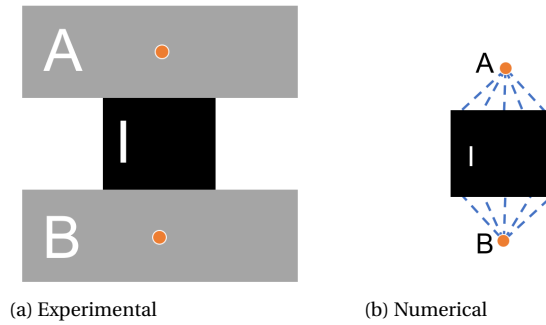


Figure 11.1: Comparison between numerical and experimental situation

The inertia tensor is acting within the local coordinate system of the virtual point. Inertia values are therefore adapting to its position within the global coordinate system. The inertia tensor for the cross is obtained from Abaqus and is given in 11.3. The zero off-diagonal terms are due to the symmetric shape of the cross. Locating the VP not at the centre of mass will result in non-zero off-diagonal values.

$$\mathbf{I}_c = \begin{bmatrix} I_{xx} & & \\ I_{yx} & I_{yy} & \\ I_{zx} & I_{zy} & I_{zz} \end{bmatrix} = \begin{bmatrix} 445.73 & 0 & 0 \\ 0 & 445.73 & 0 \\ 0 & 0 & 835.20 \end{bmatrix} [\text{kg}\cdot\text{mm}^2] \quad (11.3)$$

Adding the inertia to a point mass can be done within the FE software Abaqus by accessing the interaction module and then select "special". The parallel axis theorem [1] is used if the VP cannot be located within the centre of mass of the attached structure.

11.2. Drivingpoint-stiffness validation

The FE model that includes the inertia enables one to validate the performance of the optimization method. In this section the drivingpoint-stiffness $Z_{11}^{AIB\text{num}}$ of the optimized material model is presented. The results are validated with respect to the experimental $Z_{11}^{AIB\text{exp}}$. The magnitude and phase are presented in Figure 11.2 and 11.3 respectively.

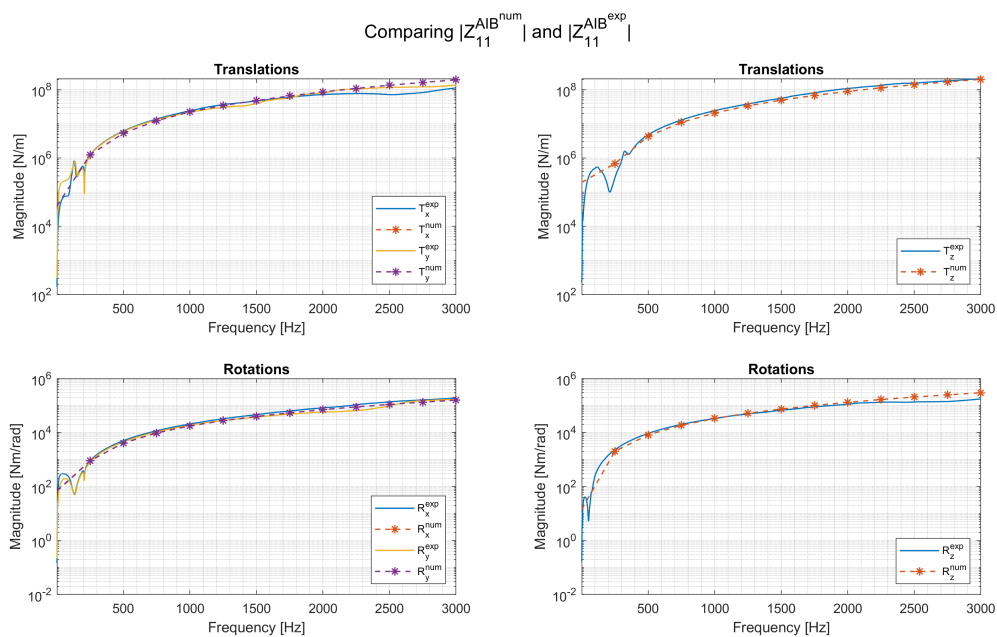


Figure 11.2: Comparison of numerical mass model and experimental drivingpoint-stiffness

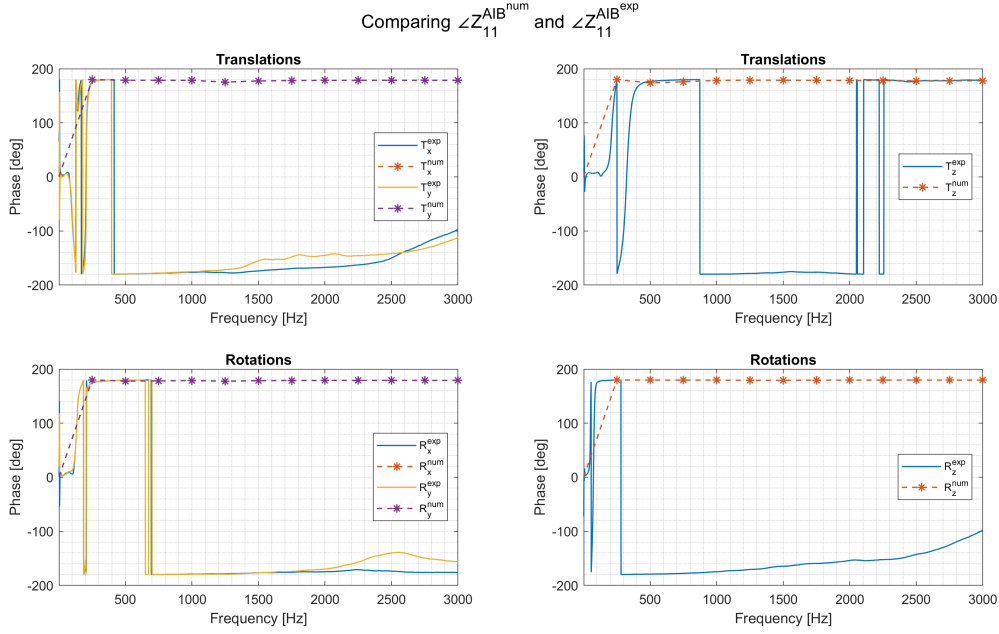


Figure 11.3: Comparison of numerical mass model and experimental drivingpoint-stiffness

Observations:

1. The magnitude of the optimized model follows the experiment within a respectable margin.
2. $f = 0 - 500$ Hz: Due to a coarse simulation it cannot follow this behaviour.
3. The FE model is not able to follow the stiffness dips present at around ± 2500 Hz.
4. The increase of phase as a function of frequency, seen at $T_{x,y}^{\text{exp}}$, $R_{x,y}^{\text{exp}}$ and R_z^{exp} , is not represented by the optimized FE model.

Numerical Explanation:

1. The results do not yet prove the optimization is correct. One conclusion that can be taken is that the crosses can be modelled as a point-mass which only represent the inertial values, but ignoring damping and stiffness.
2. A finer optimization and simulation is needed to conclude the performance in this frequency region.
3. The effect of the material properties seem to have a minor effect on the drivingpoint-stiffness. $|Z_{11}^{AIB\text{exp}}|$ is dominated by the mass of the crosses.
4. It is expected that the phase offset is resulting from the damping of the elastic cords.

The coherence, of the initial and optimized model, with respect to the experiment is used to validate performance:

$$\text{Coherence improvement} = \text{coh}(Z_{11}^{AIB\text{num}}, Z_{11}^{AIB\text{exp}}) - \text{coh}(Z_{11}^{AIB\text{num}}, Z_{11}^{AIB\text{exp}}) \quad (11.4)$$

where the coherence between two complex signals is given by the following formula:

$$\text{coh}(x, y) \triangleq \frac{(x + y)(x^* + y^*)}{2(xx^* + yy^*)} \quad (11.5)$$

where x^* is the complex conjugate of x . This formula is able to compare two signal by considering both amplitude and phase.

The results are presented in Figure 11.4. A clear performance improvement is observed in the first half of the frequency range. In this work the multi-KHz range is considered and as a result the effect of inertia on the dynamic drivingpoint-stiffness dominates the material properties of the vibration damper. This effect

is shown in Figure 11.5 in which the drivingpoint-stiffness is presented with changed stiffness and damping values. Again the one DoF double-mass-spring-damper system is being considered. It can be concluded that the region around the dip is most sensitive for the change in damping and stiffness (material properties). The dip is a result of a resonance which can be observed in the receptance and its location is determined by the properties of the rubber object and the mass of the attached structures.

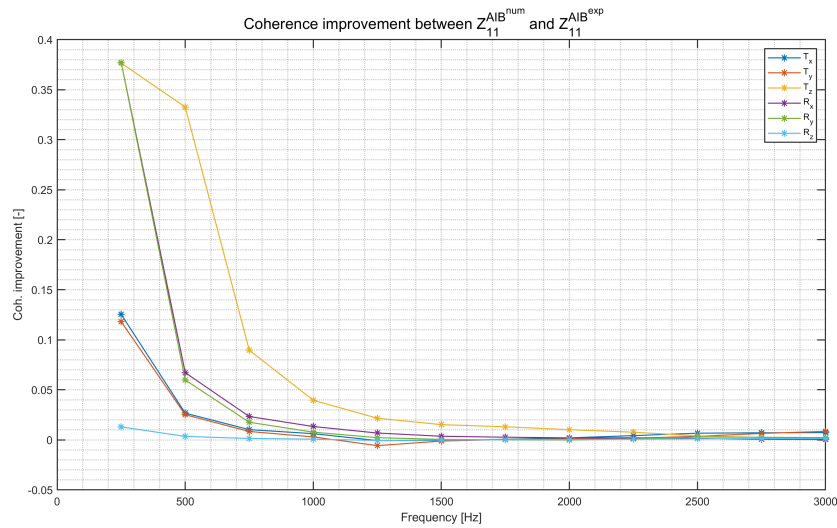


Figure 11.4: Validation with drivingpoint-stiffness

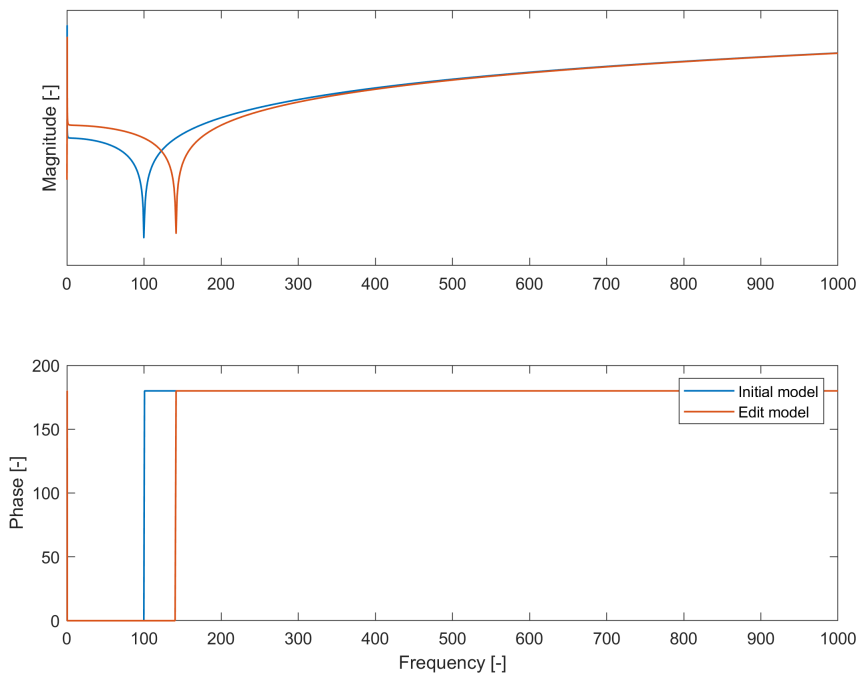


Figure 11.5: Z_{11}^{base} affected by stiffness and damping variations.

It is concluded that the drivingpoint validation is a useful indicator for a limited frequency range. The upper limit behaviour is dominated by the inertia of the attached structures. The material model optimization improves results over the full frequency range, only at higher frequency this is less observable.

11.3. Drivingpoint-Stiffness Rubber

In this section the final results are presented for the numerical drivingpoint-stiffness of the rubber object. To obtain Z_{11}^{num} the inertial values are removed from the FE model. In Figure 11.6 and 11.7 the change in drivingpoint-stiffness is presented with respect to the initial material model. Apart from presenting the results it is difficult to conclude on these results. The results are just a consequence of a difference in material properties.

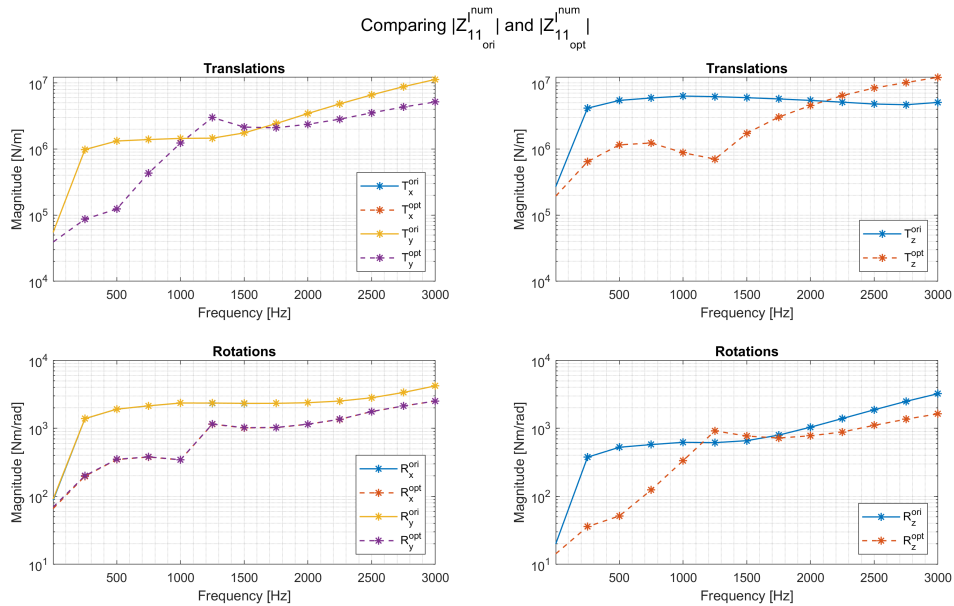


Figure 11.6: Drivingpoint-stiffness $|Z_{11}^{num}|$ comparison between original and optimized moduli

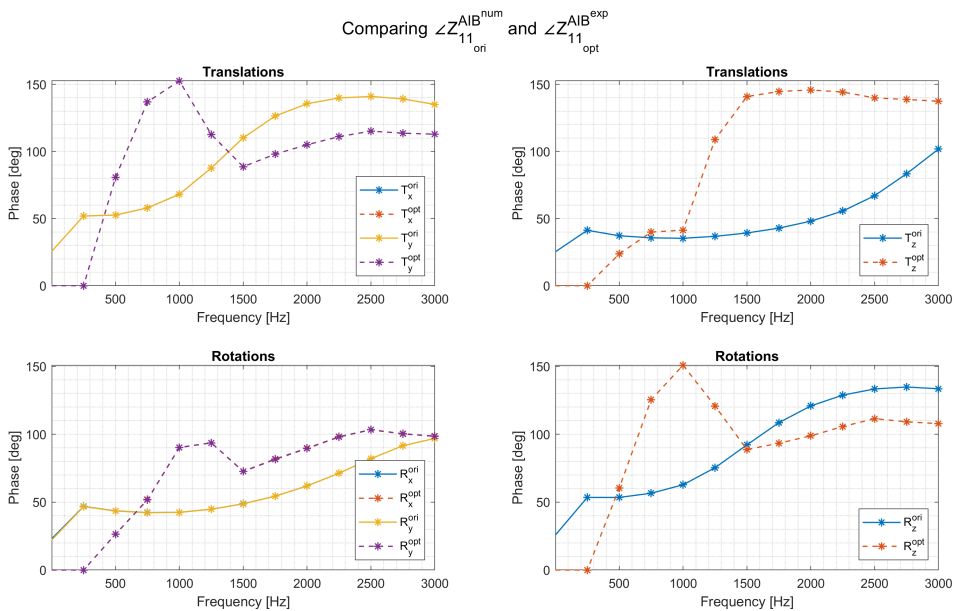


Figure 11.7: Drivingpoint-stiffness $\angle Z_{11}^{num}$ comparison between original and optimized moduli

Observations:

1. The magnitude and phase are significantly affected.
2. In general the optimized magnitude is lower.

3. The optimized stiffness is less continuous. The optimized moduli now represents experimentally observed effects.

Conclusions and Recommendations

In this section one can find the conclusions and recommendations resulting from the work done in this thesis. The goal of this research was to provide a new approach to numerically extract material properties through experimental impact testing. It considers:

- **Chapter 8:** Numerically model the dynamic behaviour of the rubber geometry that is directly comparable to experimental results.
- **Chapter 9:** Experimentally characterize the transfer- and drivingpoint-stiffness of a rubber vibration damper.
- **Chapter 10:** Numerically mimic the experimental result by optimizing the material model parameters.
- **Chapter 11:** Validate results by comparing the drivingpoint-stiffness obtained from the updated numerical model and experimental results. After the validation the drivingpoint-stiffness K_{11}^I is obtained from the numerical model.

The results in this work are findings to the following questions:

- **Can a combination of impact testing and numerical simulation provide a method to obtain rubber material properties?**
- *Which experimental conditions are needed to characterize only the rubber object?*
- *Does an impact test method provide good quality data for the optimization?*
- *Which approach is needed to make the experimental and numerical results comparable?*
- *Which experimental results are best used as a reference value for the optimization?*
- *What optimization approach is best for this case?*
- *Does the optimized material model resembles behaviour observed in literature?*
- *Can the experimental results provide one with a validation measure?*

12.1. Recap

In Chapter 8 the numerical modelling is defined in detail. The Abaqus software is used because of its wide variety of viscoelastic material models. Abaqus has the ability to be activated by Matlab which is proven to be very beneficial. The hybrid elements are used to model the incompressible behaviour. The virtual point method is modelled with a combination of reference points and RBE2 elements. The *tabular data* way of modelling a viscoelastic material is used because it enables one to optimize data with respect to one frequency point.

Chapter 9 described the process of experimentally characterize the dynamic stiffness of the vibration damper. It shows that the impact method is able to characterize the dynamic behaviour. The results of the diagonal terms are comparable to a one DoF double-mass-spring-damper system. The elastic mounting, that should mimic a free-free boundary condition, affects the low frequency behaviour. The transfer-stiffness is obtained by making use of the inverse substructuring method. The receptance FRFs are good, but the conditioning number is high at low frequency. The conditioning number causes the matrix inversion to worsening the results. Especially the rotational transfer-stiffness are proven to be hard to characterize.

In Chapter 10 the material model optimization is presented. A RMSE function for the dynamic stiffness is presented which separates the real and imaginary parts. The global optimization method minimizes this RMSE function. In terms of reference values a reduction is made. The optimization only uses the diagonal terms of the transfer-stiffness for a direct comparison. Using more reference values leads to physically unrealistic material behaviour. In this chapter it is proven that the method significantly improves the numerical results when using experimental results as a reference.

Finally the performance of the optimization is validated in Chapter 11. In the drivingpoint-stiffness a validation measure is found. Up to the first resonance frequency it is sufficient to model the, experimentally used, transmission simulators with only its inertial values. Adding the structures to the FE model makes the drivingpoint-stiffness directly comparable to the experimentally obtained values. It is found that the drivingpoint-stiffness can only be used as a good validation measure at low frequency. The validation frequency range is limited by the first resonance frequency of the object. The object in this case study has its resonance frequency below the first optimization point. The low frequency results, affected by the mounting, are not useful to be optimized.

12.2. Conclusions

In this section the conclusions for this work are presented. The conclusion is subdivided in three main topics, namely:

Numerical

- Virtual point modelling is proven to be a good method to;
 - obtain concentrated results at a location that fits the needs of the user.
 - enables one to directly compare numerical and experimental results.
 - provide a way to overcome the problem of numerical sparse stiffness matrices.
- DMA data is used to describe the relaxation behaviour. Results from other research is sufficient for obtaining initial material model parameters.
- In the FE model, the dynamics of the transmission simulators can be simplified to only its inertial values. One can obtain the drivingpoint-stiffness without applying complex decoupling methods.
- Due to symmetry of the object one is able to reduce the number of simulation from 12 (all DoF) to 4 (T_x/T_y , T_z , R_x/R_y and R_z).
- The method presented in this work provides a way to predict the, hard to measure, rotational stiffness values while experimentally only translational stiffness needs to be characterized.
- A weak link is observed between some DoF of the stiffness matrix. This must be taken into account when analysing the results. In particular the phase is sensitive for numerical noise. The weak DoF are also sensitive for meshing variations. This work presents a measure for detecting these weak links.

Experimental

- The dynamic transfer-stiffness can be obtained in an experimental way by making use of the impact method.
- At low frequency the measured receptance is affected by the elastic mounting. The directions in parallel to the elastic cords are affected the most.
- Both the drivingpoint- and transfer-receptance show behaviour equivalent to a one DoF Double-mass-damper-spring-system. Only the rotational receptance R_x, R_y show a significant cross-coupling with the translation T_x, T_y .
- It is not possible to measure drivingpoint- and transfer-receptance within the same measurement. The force is limited due to sensor limitations. The impact force must be small enough to not overshoot the sensors located at the impact side, but the force must be hard enough to get a good noise-to-signal ratio. It is found that both conditions cannot be met with a consistent impact force.
- The conditioning number is high at low frequency which results in worse performance of the inverse substructuring method. The effect of this is best seen at the rotational transfer-stiffness.

Optimization

- The Surrogate solver is used to find the absolute minimum with bounded inputs. In contrary to other methods, the Surrogate solver is not dependent on the initial values. This makes the solver more robust than others.

- The results show that the optimization method is able to improve the numerical transfer-stiffness with respect to the experimental results.
- The optimization method automatically includes geometry- and loadcase-specific stiffness effects. Including these effects makes the material model case specific. The method expands the standard numerical capabilities where these effects are not taken into account.
- The results shows that the deformation mode for obtaining T_z , R_x and R_y are highly affected by the Poisson's ratio used in the FE model. The numerical dynamic stiffness is very sensitive to small changes in the Poisson's ratio.
- The advised Poisson ratio leads to optimization values which yield unrealistic material behaviour such as negative moduli. Lowering the Poisson ratio is a method for obtaining physically reasonable values.
- The experimental drivingpoint-stiffness is not a good validation measure. The behaviour is dominated by the inertial values of the attached crosses.
- For point-wise optimization the viscoelastic tabular data is a good way of defining material properties.

12.3. Recommendations

In this section improvements for both numerical and experimental methods are provided. The recommendations are resulting from the limitation found in this research and the opportunities for futures ones.

Numerical

- It is advised to use more computational performance. It enables one to perform the optimization at more frequency-points, apply a finer mesh or reduce computational time. The objective function includes the simulation. Finding a minimum is therefore time consuming.
- Fine low frequency optimization is needed to use the drivingpoint-stiffness as a good validation measure. The validation can take place at and around the resonance frequency of the measured object.
- The moduli should be continuous. Applying curve-fitting to the obtained moduli can minimize the dependency on the geometry and loadcase. Performance of the moduli in other loadcases is expected to improve.
- The Surrogate solver enables one to use parallel computing, which could significantly improves computational efficiency. The main challenge is to edit variables in files that are not handled simultaneously due to the parallel computing.
- Precaution needs to be taken before analysing phase results. If the magnitude is very low, numerical noise can significantly affect the obtained phase. In this work a simple symmetry check is sufficient to detect the strong values. Also the presented relative measure is a good indicator for strongly linked DoF.

Experimental

- One can improve the accuracy of low frequency results by optimizing the mounting. The cords should apply minimal force and moment to the structure. Also the elastic properties of the cord with respect to the mass of the structure needs to be chosen such that decoupling takes place at lower frequency.
- The use of more sensors is preferable. The experimental effort can be reduced significantly and results are expected to be more consistent.
- The experiment lacks the ability to obtain drivingpoint- and transfer-stiffness simultaneously. Due to damping there is a large difference in acceleration between the driving- and transferpoint. A hard impact leads to overshoot in drivingpoint sensors and a soft impact results in a high SNR in the transferpoint sensors. If one can use larger range accelerometers at the drivingpoint, it can prevent the sensors from overshooting. The excitation force can therefore be high enough to get a good SNR at the transferpoint accelerometers.

Bibliography

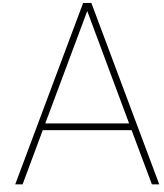
- [1] A. R. Abdulghany. Generalization of parallel axis theorem for rotational inertia. *American Journal of Physics*, 85(10):791–795, 2017. ISSN 0002-9505. doi: 10.1119/1.4994835. URL <http://aapt.scitation.org/doi/10.1119/1.4994835>.
- [2] Yawar Jamil Adeel, Ahsan Irshad Muhammad, and Azmat Zeeshan. Characterization of Hyperelastic (Rubber) Material Using Uniaxial and Biaxial Tension Tests. *Advanced Materials Research*, 570:1–7, 2012. ISSN 1662-8985. doi: 10.4028/www.scientific.net/AMR.570.1.
- [3] Fadi Alkhatib and University of Wisconsin-Milwaukee. Techniques for Engine Mount Modeling and Optimization. (December):1–164, 2013.
- [4] Per-Erik Austrell. Modeling of Elasticity and Damping for Filled Elastomers. page 210, 1997.
- [5] H. Baaser, Ch Hopmann, and A. Schobel. Reformulation of strain invariants at incompressibility. *Archive of Applied Mechanics*, 83(2):273–280, 2013. ISSN 09391533. doi: 10.1007/s00419-012-0652-2.
- [6] Klaus-Jürgen Bathe. *Finite element procedures. Second edition.* 2006. ISBN 978-0-9790049-5-7.
- [7] H H Baumgartl, M., Winter. Determination of relaxation and retardation spectra from dynamical mechanical data. *Rheologica Acta*, 28:511–519, 1989.
- [8] Clemens Beijers, Bram Noordman, and Andre’ de Boer. NUMERICAL MODELLING OF RUBBER VIBRATION ISOLATORS : identification of material parameters. pages 3193–3200, 2004.
- [9] Liliane Bokobza. Mechanical and Electrical Properties of Elastomer Nanocomposites Based on Different Carbon Nanomaterials. *C*, 3(2):10, 2017. ISSN 2311-5629. doi: 10.3390/c3020010.
- [10] D. D. Bortoli, E. Wrubleski, and R. J. Marczak. Hyperfit – Curve Fitting Software For Incompressible Hyperelastic Material Models. *21st Brazilian Congress of Mechanical Engineering*, (April 2016), 2011. doi: 10.13140/2.1.4055.7448.
- [11] David L. Brown. AR-8_Halvorsen_Brown_Sound_and_Vibration 1977.pdf. *Impulse Technique for Structural Frequency Response Testing*, page 12, 1977.
- [12] Roger Brown. *Physical testing of rubber.* Springer, 4th edition, 2006. ISBN 13 9780387282862.
- [13] J Burns and P S Dumbleday. Dynamic bulk modulus of soft elastomers. *Journal of Polymer Science*, 28: 181, 1990.
- [14] L. Chazeau, J. D. Brown, L. C. Yanyo, and S. S. Sternstein. Modulus recovery kinetics and other insights into the Payne effect for filled elastomers. *Polymer Composites*, 21(2):202–222, 2000. ISSN 02728397. doi: 10.1002/pc.10178.
- [15] J Ciambella. Experimental Testing and Nonlinear Viscoelastic Modeling of Filled Rubber. page 151, 2010.
- [16] Michael Coja. *Effective Vibro-Acoustical Modelling of Rubber Isolators.* 2005. ISBN 9171781048.
- [17] M. Fernanda P Costa and C. Ribeiro. Parameter estimation of viscoelastic materials: A test case with different optimization strategies. *AIP Conference Proceedings*, 1389:771–774, 2011. ISSN 0094243X. doi: 10.1063/1.3636846.
- [18] Dassault Systèmes Simulia. Abaqus 6.12: Keywords Reference Manual. *Manuals*, page 1545, 2012.
- [19] Rijk de Rooij and Ellen Kuhl. Constitutive Modeling of Brain Tissue: Current Perspectives. *Applied Mechanics Reviews*, 68(1):010801, 2016. ISSN 0003-6900. doi: 10.1115/1.4032436.

- [20] Julie Diani, Bruno Fayolle, and Pierre Gilormini. A review on the Mullins effect. *European Polymer Journal*, 45(3):601–612, 2009. ISSN 00143057. doi: 10.1016/j.eurpolymj.2008.11.017.
- [21] A. Dorfmann and R. W. Ogden. A constitutive model for the Mullins effect with permanent set in particle-reinforced rubber. *International Journal of Solids and Structures*, 41(7):1855–1878, 2004. ISSN 00207683. doi: 10.1016/j.ijsolstr.2003.11.014.
- [22] G Eisele, P Genender, and K Wolff. Electric Vehicle Sound design - Just Wishful Thinking? *Proceedings of Aachen Acoustics Colloquium*, pages 22–24, 2010.
- [23] M. J. Garcia Tarrago. Engineering rubber bushing stiffness formulas including dynamic amplitude dependence. *Engineering Sciences*, 2006.
- [24] M. J. García Tárrago, L. Kari, J. Vinolas, and N. Gil-Negrete. Frequency and amplitude dependence of the axial and radial stiffness of carbon-black filled rubber bushings. *Polymer Testing*, 26(5):629–638, 2007. ISSN 01429418. doi: 10.1016/j.polymertesting.2007.03.011.
- [25] Alan N. Gent. *Engineering with Rubber*, volume 59. Carl Hanser Verlag GmbH & Co. KG, München, feb 2012. ISBN 978-3-446-42764-8. doi: 10.3139/9783446428713.
- [26] N. Gil-Negrete, J. Vinolas, and L. Kari. A Nonlinear Rubber Material Model Combining Fractional Order Viscoelasticity and Amplitude Dependent Effects. *Journal of Applied Mechanics*, 76(1):011009, 2009. ISSN 00218936. doi: 10.1115/1.2999454.
- [27] M. Haeussler, Steven W. B. Klaassen, and D. J. Rixen. Comparison of Substructuring based techniques for dynamic property identification of rubber isolators. *ISMA 2018 - International Conference on Noise and Vibration Engineering*, (August):1, 2018.
- [28] Paul Håkansson, Anders Pettersson, Kockums Ab, and Matti Ristinmaa. Finite Element Modelling of A Rubber Block Exposed to Shock Loading. page 83, 2000.
- [29] P. Höfer and A. Lion. Modelling of frequency- and amplitude-dependent material properties of filler-reinforced rubber. *Journal of the Mechanics and Physics of Solids*, 57(3):500–520, 2009. ISSN 00225096. doi: 10.1016/j.jmps.2008.11.004.
- [30] Gregor Huber, Thomas A. Vilgis, and Gert Heinrich. Universal properties in the dynamical deformation of filled rubbers. *Journal of Physics Condensed Matter*, 8(29):10–14, 1996. ISSN 09538984. doi: 10.1088/0953-8984/8/29/003.
- [31] Hanen Jrad, Jean Luc Dion, Franck Renaud, Imad Tawfiq, and Mohamed Haddar. Experimental characterization, modeling and parametric identification of the non linear dynamic behavior of viscoelastic components. *European Journal of Mechanics, A/Solids*, 42:176–187, 2013. ISSN 09977538. doi: 10.1016/j.euromechsol.2013.05.004.
- [32] Leif Kari. On the dynamic stiffness of preloaded vibration isolators in the audible frequency range: modeling and experiments. *The Journal of the Acoustical Society of America*, 113(May 1999):1909–1921, 2003. ISSN 00014966. doi: 10.1121/1.1557214.
- [33] Fredrik Karlsson and Anders Persson. MODELLING NON-LINEAR DYNAMICS OF RUBBER BUSHINGS - Parameter Identification and Validation. *Master thesis*, 2003. ISSN 0281-6679.
- [34] Beomkeun Kim, Seong Beom Lee, Jayone Lee, Sehyun Cho, Hyungmin Park, Sanghoon Yeom, and Sung Han Park. A comparison among Neo-Hookean model, Mooney-Rivlin model, and Ogden model for Chloroprene rubber. *International Journal of Precision Engineering and Manufacturing*, 13(5):759–764, 2012. ISSN 12298557. doi: 10.1007/s12541-012-0099-y.
- [35] B.K. Kim, S.K. Youn, and W.S. Lee. A constitutive model of rubber under small oscillatory load superimposed on large static deformation. *Archive of Applied Mechanics (Ingenieur Archiv)*, 73(11-12):781–798, 2004. ISSN 0939-1533. doi: 10.1007/s00419-004-0325-x.
- [36] Zorion Kareaga Laka. Dynamic Stiffness and Damping Prediction on Rubber Material Parts , FEA and Experimental Correlation. page 314, 2016.

- [37] Jeong Hak Lee and Kwang Joon Kim. Characterization of complex modulus of viscoelastic materials subject to static compression. *Mechanics Time-Dependent Materials*, 5(3):255–271, 2001. ISSN 13852000. doi: 10.1023/A:1017996207164.
- [38] Y. H. Lee, J-s Kim, K J Kim, T Ahn, B-i Choi, H J Lee, C.-S. Woo, and K.-S. Kim. Prediction of dynamic stiffness on rubber components considering preloads. *Materialwissenschaft und Werkstofftechnik*, 44(5):372–379, may 2013. ISSN 09335137. doi: 10.1002/mawe.201300139.
- [39] Tian Ran Lin, Nabil H. Farag, and Jie Pan. Evaluation of frequency dependent rubber mount stiffness and damping by impact test. *Applied Acoustics*, 66(7):829–844, 2005. ISSN 0003682X. doi: 10.1016/j.apacoust.2004.10.004.
- [40] Wenbo Luo, Xiaoling Hu, Chuhong Wang, and Qifu Li. Frequency- and strain-amplitude-dependent dynamical mechanical properties and hysteresis loss of CB-filled vulcanized natural rubber. *International Journal of Mechanical Sciences*, 52(2):168–174, 2010. ISSN 00207403. doi: 10.1016/j.ijmecsci.2009.09.001.
- [41] Kevin P. Menard and Noah R. Menard. *Dynamic Mechanical Analysis in the Analysis of Polymers and Rubbers*. Number 9. 2015. ISBN 9780471440260. doi: 10.1002/0471440264.pst102.pub2.
- [42] Himanshu Mevada and Dipal Patel. Experimental Determination of Structural Damping of Different Materials. *Procedia Engineering*, 144:110–115, 2016. ISSN 18777058. doi: 10.1016/j.proeng.2016.05.013. URL <http://dx.doi.org/10.1016/j.proeng.2016.05.013>.
- [43] D. F. Moore and W. Geyer. A review of hysteresis theories for elastomers. *Wear*, 30(1):1–34, 1974. ISSN 00431648. doi: 10.1016/0043-1648(74)90055-6.
- [44] T. Mukhopadhyay, S. Adhikari, and A. Batou. Frequency domain homogenization for the viscoelastic properties of spatially correlated quasi-periodic lattices. *International Journal of Mechanical Sciences*, (September), 2017. ISSN 00207403. doi: 10.1016/j.ijmecsci.2017.09.004.
- [45] Hiroshi Murata, Norihiro Taguchi, Taizo Hamada, and John F. McCabe. Dynamic viscoelastic properties and the age changes of long-term soft denture liners. *Biomaterials*, 21(14):1421–1427, 2000. ISSN 01429612. doi: 10.1016/S0142-9612(00)00010-7.
- [46] Anders Nilsson and Bilong Liu. *Vibro-acoustics*, volume 1. 2012. ISBN 9783662478066. doi: 10.1007/978-3-662-47807-3.
- [47] Scott Allen Noll, Benjamin Joodi, Jason Dreyer, and Rajendra Singh. Volumetric and Dynamic Performance Considerations of Elastomeric Components. *SAE International Journal of Materials and Manufacturing*, 8(3):2015–01–2227, 2015. ISSN 1946-3987. doi: 10.4271/2015-01-2227.
- [48] R. W. Ogden, G. Saccomandi, and I. Sgura. Fitting hyperelastic models to experimental data. *Computational Mechanics*, 34(6):484–502, 2004. ISSN 01787675. doi: 10.1007/s00466-004-0593-y.
- [49] Robin Öhrn. Prediction of static and dynamic behavior of powertrain suspension rubber components. page 81, 2015.
- [50] Anders K Olsson. *Finite Element Procedures in Modelling the Dynamic Properties of Rubber*. 2007. ISBN 9789162871307.
- [51] Anders K Olsson and Per-erik Austrell. Finite Element Analysis of a Rubber Bushing Considering Rate and Amplitude Dependent Effects. pages 77–89.
- [52] Lu Ean Ooi and Zaidi Mohd Ripin. Dynamic stiffness and loss factor measurement of engine rubber mount by impact test. *Materials and Design*, 32(4):1880–1887, 2011. ISSN 02641275. doi: 10.1016/j.matdes.2010.12.015.
- [53] Rickard Österlöf. *Modelling of the Fletcher-Gent effect and obtaining hyperelastic parameters for filled elastomers*. 2014. ISBN 9789175952734. doi: 9789175952734.
- [54] A. R. Payne. The Dynamic Properties of Carbon Black-Loaded Natural Rubber Vulcanizates. Part I. VI (19):57–63, 1837.

- [55] T. Ramachandran, M. C. Lenin Babu, and K. P. Padmanaban. Experimental Investigation of Static and Dynamic Properties of Steel–Rubber, Cast Iron–Rubber and Epoxy Granite–Rubber as IC Engine Mount. *Transactions of the Indian Institute of Metals*, 68(1):83–86, 2015. ISSN 09751645. doi: 10.1007/s12666-015-0612-y.
- [56] C. M. Richards and R. Singh. Characterization of rubber isolator nonlinearities in the context of single- and multi-degree-of-freedom experimental systems. *Journal of Sound and Vibration*, 247(5):807–834, 2001. ISSN 0022460X. doi: 10.1006/jsvi.2001.3759.
- [57] Lucie Rouleau, Rogério Pirk, Bert Pluymers, and Wim Desmet. Characterization and Modeling of the Viscoelastic Behavior of a Self-Adhesive Rubber Using Dynamic Mechanical Analysis Tests. *Journal of Aerospace Technology and Management*, 7(2):200–208, 2015. ISSN 2175-9146. doi: 10.5028/jatm.v7i2.474.
- [58] David Roylance. *Engineering Viscoelasticity*. 2001. ISBN 9781461481386.
- [59] Viktor Sandell. Extraction of Material Parameters for Static and Dynamic Modeling of Carbon Black Filled Natural Rubbers. 2017.
- [60] Mattias Sjöberg. On dynamic properties of rubber isolators. 2002.
- [61] Mattias Sjöberg and Leif Kari. Nonlinear isolator dynamics at finite deformations: An effective hyperelastic, fractional derivative, generalized friction model. *Nonlinear Dynamics*, 33(3):323–336, 2003. ISSN 0924090X. doi: 10.1023/A:1026037703124.
- [62] N. Suphadon, A. G. Thomas, and J. J. C. Busfield. Viscoelastic behavior of rubber under a complex loading. *Journal of Applied Polymer Science*, 113(2):693–699, jul 2009. ISSN 00218995. doi: 10.1002/app.30102.
- [63] N. Suphadon, A. G. Thomas, and J. J. C. Busfield. The viscoelastic behaviour of rubber under a small simple shear oscillation superimposed on a large pure shear. *Polymer Testing*, 29(4):440–444, 2010. ISSN 01429418. doi: 10.1016/j.polymertesting.2010.02.002.
- [64] Anders Thorin, Aurélie Azoug, and Andrei Constantinescu. Influence of prestrain on mechanical properties of highly-filled elastomers: Measurements and modeling. *Polymer Testing*, 31(8):978–986, 2012. ISSN 01429418. doi: 10.1016/j.polymertesting.2012.07.014.
- [65] Rafael Tobajas, Elena Ibartz, and Luis Gracia. A comparative study of hyperelastic constitutive models to characterize the behavior of a polymer used in automotive engines. *Proceedings of 2nd International Electronic Conference on Materials*, page A002, 2016. doi: 10.3390/ecm-2-A002.
- [66] Nicholas W. Tschoegl. Constitutive Equations for Elastomers. *Journal of Polymer Science Part A: Polymer Chemistry*, 9(9171):1959–1970, 1971.
- [67] H. Ucar and I. Basdogan. Dynamic characterization and modeling of rubber shock absorbers: A comprehensive case study. *Journal of Low Frequency Noise Vibration and Active Control*, 37(3):509–518, 2018. ISSN 20484046. doi: 10.1177/1461348417725954.
- [68] M. van der Seijs, D. van den Bosch, D. Rixen, and D. de Klerk. An Improved Methodology for the Virtual Point Transformation of Measured Frequency Response Functions in Dynamic Substructuring. *Proceedings of the 4th International Conference on Computational Methods in Structural Dynamics and Earthquake Engineering (COMPDYN 2013)*, (April 2017):4334–4347, 2014. doi: 10.7712/120113.4816.C1539.
- [69] Maarten Vincent Van Der Seijs. *Experimental Dynamic Substructuring*. Number November. 2016. ISBN 9789461866714. doi: uuid:28b31294-8d53-49eb-b108-284b63edf670.
- [70] S Voormeeren. Coupling Procedure Improvement & Uncertainty Quantification in Experimental Dynamic Substructuring–Validation and Application in Automotive Research. *Delft University of Technology, Delft, the Netherlands*, 2007.

- [71] S N Voormeeren, Modeling Techniques, Maarten Van Der Seijs, Beam Section, Finite Element Method, The Fem, G R Liu, Petr Krysl, S Van Koutrik, Dennis De Klerk, Chapter Outline Head, Jacob Fish, and Special Purpose Elements. *Experimental Dynamic Substructuring*, volume 7. 2014. ISBN 9780080983561. doi: 10.1016/B978-0-08-098356-1.00014-X.
- [72] Jun Wang, Dagang Sun, Shizhong Liu, and Xin Zhang. Damping Characteristics of Viscoelastic Damping Structure under Coupled Condition. *Mathematical and Computational Applications*, 22(1):27, 2017. ISSN 2297-8747. doi: 10.3390/mca22010027.
- [73] Zhi Wei Wang and Jun Wang. Inverse substructure method of three-substructures coupled system and its application in product-transport-system. *JVC/Journal of Vibration and Control*, 17(6):943–952, 2011. ISSN 10775463. doi: 10.1177/1077546310376083.
- [74] D. Wollscheid and A. Lion. Predeformation- and frequency-dependent material behaviour of filler-reinforced rubber: Experiments, constitutive modelling and parameter identification. *International Journal of Solids and Structures*, 50(9):1217–1225, 2013. ISSN 00207683. doi: 10.1016/j.ijsolstr.2012.12.015.
- [75] Yunhe Yu, Nagi G. Naganathan, and Rao V. Dukkipati. Literature review of automotive vehicle engine mounting systems. *Mechanism and Machine Theory*, 36(1):123–142, 2001. ISSN 0094114X. doi: 10.1016/S0094-114X(00)00023-9.
- [76] Qiang Zhang, Xiaoxiong Jin, and Wei Peng. A non-linear finite element analysis of car engine mounting system rubber components. *ISCID 2009 - 2009 International Symposium on Computational Intelligence and Design*, 1:132–135, 2009. doi: 10.1109/ISCID.2009.40.



Theoretical Background

A.1. Virtual Point Theory

Before observing the FRFs some more background information.

- The goal of a set of impacts is to trigger all six DOF of the virtual point. This means that three translations and rotations need to be activated by the set of impacts. Translations are triggered with the right impact direction, however the rotations are sensitive for location. Further away from the virtual point a larger moment can be created. There is a negative side effect to placing these impacts further away from the virtual point. The virtual point transformation assumes that there is a local rigidity. This means that the structure located between impacts and sensors is infinitely stiff. When placing the impacts further away from the virtual point this assumption becomes less reasonable. A compromise has to be found between creating good momentum and not locating the impacts too far away.
- As for the impacts, the sensors must be able to detect three translations and rotations. More than two 3DOF sensors need to be used to fulfill these demands. The placement of sensors is also a compromise between a stronger signal and observing more rigid behaviour.
- The relevant matrices that are constructed are the R and T for both sensor and impact transformations towards the virtual point (VP). These matrices are placed within the IDM structure that stands for Interface Deformation Modes matrices. Left and right multiplication $IDM_u.T \cdot Y A \cdot IDM_f.T$ results in the transformed FRF matrix.

The a-structure is made of a solid piece of aluminium. It is an asymmetric structure and a FE model is available which makes it possible to evaluate results in terms of FRFs. A virtual point is constructed at the long foot of the a-structure.

The goal is to determine the dynamic properties of the A-structure captured within the virtual point. Capturing the dynamics in one point gives the opportunity to easily couple it with other structures. With multiple companies working on the same object makes this a very powerful tool. A virtual point is a non-existing point at which displacement or forces in six DoF can be obtained or applied. The six DoF are three translations and three rotations. Sensors around the virtual point will determine the local displacements that are triggered by the applied impacts. Typically the structure around a virtual point is assumed to be very stiff. This assumption will be used to transform sensor and impact data to the VP. The placement of three sensors with three DoF will result in a 9-DoF receptance matrix. With the so-called Interface Deformation Mode (IDM) filtering process the local rigid behaviour is extracted from the full dynamics. A result of this filtering is that only local rigid behaviour is left for being coupled. The goal of a virtual point is to define the nodal 6x6 receptance matrix that describes the dynamic responses between the VP displacements and forces.

In formula the following can be written down. A schematic overview of a virtual point transformation can be seen in Figure A.1. The classical FRF matrix Y describes the relation between impacts and sensor channels at these specific locations.

$$u = Y f \tag{A.1}$$

B

Parameters

B.1. DMA data

B.2. Material model

Table B.1: Prony parameters obtained from the work of Roylance [58]

M_i	16	4.3	2.0	0.8	0.75	0.45	0.09	0.15	0.10	[Mpa]
τ_i	3.333e-8	1.538e-6	2.000e-5	5.000e-5	4.000e-4	2.857e-2	6.667e-1	3.333e0	2.500e3	[s]

Table B.2: Magnitude of low frequency shear modulus obtained from the work of Gil-Negrete et al. [26]

Hardness [Shore A]	$ G^* $
40	0.6
50	1
60	2.9-3.6
70	6-7.8

Table B.3: Parameters for the fractional derivative viscoelastic model obtained from Gil-Negrete et al. [26]

Hardness [Shore A]	G_e [Mpa]	G_{fd} [Mpa]	α [-]	b [$\text{N s}^\alpha / \text{m}^2$]
50 NR	6.926×10^5	5.79×10^5	0.479	560×10^3
70 NR	1.665×10^6	7.99×10^6	0.382	8.25×10^4

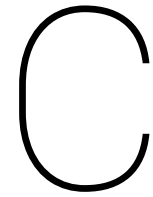
B.3. Equipment

B.3.1. Sensor specification-sheet

Model Number 356A32		Revision: F ECN #: 28478	
TRIAXIAL ICP® ACCELEROMETER			
Performance Sensitivity(± 10%) Measurement Range Frequency Range(± 5%) Resonant Frequency Broadband Resolution(1 to 10,000 Hz) Non-Linearity Transverse Sensitivity Environmental Shock Temperature Range(Operating) Temperature Response Base Strain Sensitivity Electrical Excitation Voltage Constant Current Excitation Output Impedance Output Bias Voltage Discharge Time Constant Settling Time(within 10% of bias) Spectral Noise(10 Hz) Spectral Noise(100 Hz) Spectral Noise(1 kHz) Spectral Noise(10 kHz) Physical Sensing Element Sensing Geometry Housing Material Sealing Size (Height x Length x Width) Weight Electrical Connector Mounting Thread Mounting Torque	SI 10.2 mV/(m/s ²) ± 491 m/s ² pk 1.0 to 4000 Hz 0.7 to 5000 Hz ≥ 25 kHz 0.003 m/s ² rms ≤ 1% ≤ 5% ± 5000 g pk -65 to +250 °F See Graph 0.001 g/με 24 to 30 VDC 2 to 20 mA 5,200 ohm 7 to 16 VDC 0.4 to 1.5 sec 6-9 sec 6 μg/√Hz 20 μg/√Hz 6 μg/√Hz 3 μg/√Hz 2 μg/√Hz Ceramic Shear Titanium Hermetic 11.4 mm x 11.4 mm x 11.4 mm [1] 8.36 g 8-36 4-Pin Side 5-40 Female 4 to 5 in-lb 45 to 55 N-cm	Optional versions have identical specifications as listed for the standard model except where noted below. More than one option may be used. T - TEDS Capable of Digital Memory and Communication Compliant with IEEE P1451.4 TLA - TEDS LMS International - Free Format TLB - TEDS LMS International - Automotive Format TLD - TEDS LMS International - Aerospace/Aviation Format TLU - TEDS Capable of Digital Memory and Communication Compliant with IEEE 1451.4 Output Bias Voltage 7.7 to 17.0 VDC Weight 8.4 gm Mounting Adhesive .23 oz Adhesive	[1] [2] [1] [1] [1] [1] [1] [1] [1] [1] [1] [1] [1] [1] [1] [1]
NOTES: [1] Typical [2] Zero-based, least-squares, straight line method. [3] See PCB Declaration of Conformance PS023 for details.			
SUPPLIED ACCESSORIES: Model 034K10 4-cond. shielded cable, 10 ft (3 m), mini 4-pin plug to (3) BNC plugs (1) Model 080A Adhesive Mounting Base (1) Model 080V09 Petro Visc. (1) Model 081A90 Mounting stud, 10-32 to 5-40 (1) Model 081A30 Mounting stud, 10-32 to 5-40 (1) Model ACS-1T NIST traceable triaxial amplitude response, 10 Hz to upper 5% frequency, (1) Model M061A27 Metric mounting stud, 5-40 to M3 x 0.50 long (1)			
Entered: [Signature] Engineer: [Signature] Sales: [Signature] Approved: [Signature] Date: 3-28-08 Date: 3-27-08 Date: 3-28-08 Date: 3-28-08		Spec Number 16563	
All specifications are at room temperature unless otherwise specified. In the interest of constant product improvement, we reserve the right to change specifications without notice. ICP® is a registered trademark of PCB Group, Inc.			
		PCB PIEZOTRONICS™ VIBRATION DIVISION 3425 Walden Avenue, Depew, NY 14043 Phone: 716-884-0001 Fax: 716-885-3886 E-Mail: vibrator@pcb.com	

B.3.2. Hammer specification-sheet

ICP® IMPACT HAMMER		Revision: L ECN #: 32387
<p>Model Number 086C03</p> <p>Performance Sensitivity(± 15 %) Measurement Range Resonant Frequency Non-Linearity</p> <p>Electrical Excitation Voltage Constant Current Excitation Output Impedance Output Bias Voltage Discharge Time Constant</p> <p>Physical Sensing Element Sealing Hammer Mass Head Diameter Tip Diameter Hammer Length Electrical Connection Position Extender Mass Weight Electrical Connector</p>	<p style="text-align: center;">SI</p> <p>2.25 mV/N ± 2224 N pk ≥ 22 kHz ≤ 1 %</p> <p>20 to 30 VDC 2 to 20 mA <100 ohm 8 to 14 VDC ≥ 2000 sec</p> <p>Quartz Epoxy 0.16 kg 1.57 cm 0.63 cm 21.6 cm 75 gm BNC Jack</p>	<p style="text-align: center;">ENGLISH</p> <p>10 mV/lbf ± 500 lbf pk ≥ 22 kHz ≤ 1 %</p> <p>20 to 30 VDC 2 to 20 mA <100 ohm 8 to 14 VDC ≥ 2000 sec</p> <p>Quartz Epoxy 0.34 lb 0.62 in 0.25 in 8.5 in 2.6 oz BNC Jack</p>
<p>OPTIONAL VERSIONS</p> <p>Optional versions have identical specifications and accessories as listed for the standard model except where noted below. More than one option may be used.</p> <p>T - TEDS Capable of Digital Memory and Communication Compliant with IEEE P1451.4</p> <p>TLD - TEDS Capable of Digital Memory and Communication Compliant with IEEE 1451.4</p>		
<p>NOTES:</p> <p>[1] Typical. [2] See PCB Declaration of Conformance PS068 for details.</p>		
<p>SUPPLIED ACCESSORIES:</p> <p>Model 081B05 Mounting Stud (10-32 to 10-32) (2) Model 084A08 Extender - Steel, 0.6" Diameter (1) Model 084B03 Hard Tip- Hard (S.S) (1) Model 084B04 Hammer Tip- Medium (White Plastic) (1) Model 084C05 Hammer Tip- Soft (Black) (2) Model 084C11 Hammer Tip- Supersoft (Red) (2) Model 085A10 Vinyl Cover For Medium Tip (Blue) (2) Model HCS-2 Calibration of Series 086 instrumented impact hammers (1)</p>		
<p>Entered: <i>AA</i> Date: <i>2/24/10</i></p>	<p>Engineer: <i>SJS</i> Date: <i>12/8/09</i></p>	<p>Sales: <i>JDM</i> Date: <i>2/17/10</i></p> <p>Approved: <i>EB</i> Date: <i>2/17/10</i></p> <p>Spec Number: 15273</p>
		
<p><i>All specifications are at room temperature unless otherwise specified. In the interest of constant product improvement, we reserve the right to change specifications without notice.</i></p> <p>ICP® is a registered trademark of PCB Group, Inc.</p>		
		
<p>3425 Walden Avenue, Depew, NY 14043 Phone: 716-684-0001 Fax: 716-685-3886 E-Mail: vibration@pcb.com</p>		



Impact variation effects on untransformed FRFs

In this section so called experimental pre-knowledge is created. This section is used as a pre-analysis and is used to create knowledge that will improve experimental results. The created knowledge will prevent the usage of wrong impacts and sensor location. The variations that are possible and being analyzed are;

- Impact and sensor positional error
- Impact and sensor directional error

The analysis is done by making use of the Vibes Matlab Toolbox. The Vibes Matlab Toolbox is later referred to as just the Toolbox. This toolbox makes it possible to create a virtual point with a FE model. In short the following steps need to be done in order to come up with a virtual point in the Toolbox.

1. Load FE model
2. Create modal model including damping
3. Apply correct impacts
4. Mount a minimal of three sensors at correct locations
5. Obtain FRF data from impact to sensor
6. Construct relevant matrices
7. Constructed transformed VP FRF matrix

A more in-depth explanation of the individual steps can be found in the upcoming section. The Vibes toolbox is a very useful tool that is used to observe effects of different variations previously mentioned. The Vibes Toolbox makes it possible to place sensors and impacts within a virtual environment. At first the effect impact position and location will have on the Frequency Response Function (FRF) will be observed, assuming there are.

C.1. Effect of Impact Position

Most experimental errors are introduced by humans. Examining the effects of known human measurement errors within a virtual environment is a safe way to develop knowledge and draw conclusions that are not affected by any other external factors. By precisely controlling the variables will improve the quality of the obtained experimental data.

In this work the focus lies on the errors between actual impact position and direction in with assumed to the intended ones. By making use of the Vibes Toolbox a script is created that can vary position and direction of an impact. This will be used to observe the effects of the errors on the obtained FRFs.

Within the script the position is randomly varied around the intended impact position. Figure C.1 shows the effect on the FRF connecting impact 5 to sensor channel 2 in y-direction. In this section so called direct FRFs are analysed and not the virtual point FRFs. Lessons can be learned from the direct FRFs and no IDM

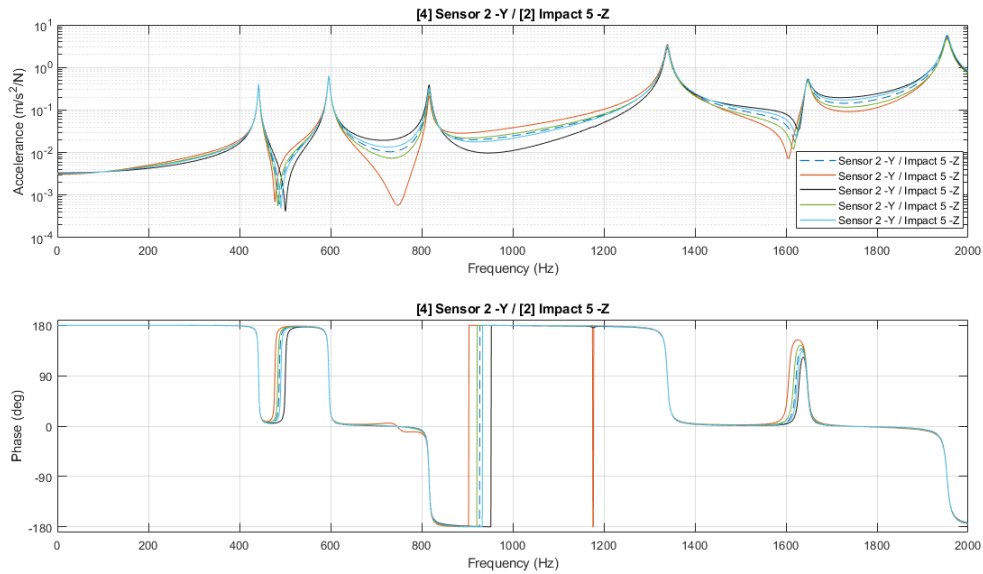


Figure C.1: Mishitting effect

filtering has taken place which makes the observations more raw. This sensor channel shows behaviour that is observed for most of the other channels. The following results are found for a positional impact error:

Observations:

1. No resonance frequency offset
2. Anti-resonance frequency offset which increases at higher frequency
3. Magnitude difference over full frequency range
4. Magnitude order flips after resonance peaks
5. General shape of FRF is minimally affected

Explanation:

1. A resonance peak is located at a natural frequency of the structure. A real structure has an infinite number of natural frequencies whereas a FE model has limited natural frequencies depending on the number of DoF of the model. The natural frequency is a frequency at which the structure resonates resulting in a large amplification of the input. At every natural frequency the structure moves in a so called mode shape. The FRF of the structure is the summation of all the individual modes acting strong in the region of their natural frequency. A resonance peak of the structure is a result of a dominant resonance peak of mode shape i . How an FRF is obtained from a combination of two mode shapes can be seen in Figure C.2.
 - It can be said that one dominant mode shape is responsible for a resonance peak in the complete system. The fact that only the magnitude of a triggered mode varies is the reason why the resonance peak does not shift due to an impact error.
2. An anti-resonance peak is different for the fact that it is a result of merging the FRFs of all mode shapes. The anti-resonance is created when the dominant mode shape that has already occurred is filtered by an out of phase upcoming dominant mode shape. A graphical representation of the previously mentioned can be observed in Figure C.2. The anti-resonance is located at the frequency where the magnitude of the two mode shapes are equal and therefore cancel each other out resulting in a sudden very low amplitude. It can be said that the anti-resonance region is affected by;
 - Position of resonance peaks located before and beyond the location of the anti-resonance.
 - Magnitude of both mode shapes.

Again observing the obtained FRF it can be said that resonance frequency is not affected and therefore not the reason for the anti-resonance shifting. The magnitude and to be more specific

the relative magnitude between the two modes are expected to be responsible for the frequency shift of the anti-resonance. This is reasonable because the structure is excited differently due to changing impact positions. The magnitude at which certain mode shapes are triggered differs between the impact variations. If one is looking for a set of multiple consistent impacts, at and the region around anti-resonance peaks are areas of interest.

3. Another interesting observation from the obtained FRF is the fact that the magnitude order flips from resonance to resonance. Therefore at the moment I do not yet have a physical explanation.

X1/F1 - modes 1 & 2 (+sum)

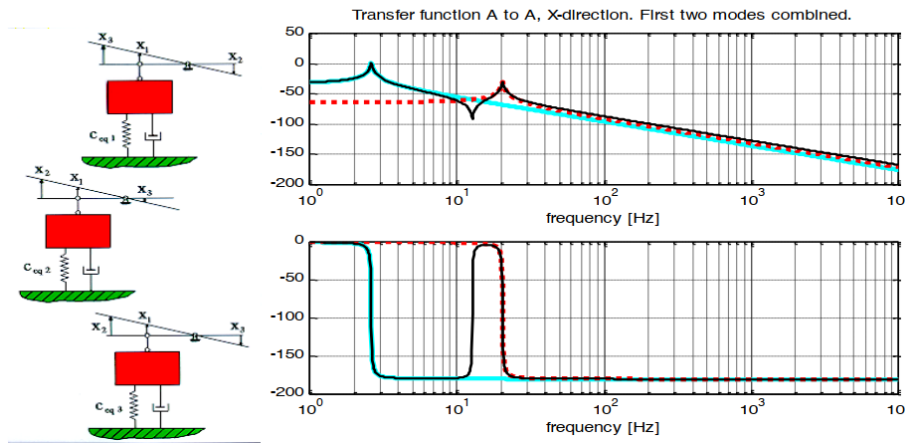


Figure C.2: (anti)-resonance build up

Until now all observation can be linked to the degree at which modes are triggered by a certain impact. Yet what is the reason that the anti-resonance frequency offset increases at higher frequency? Is the magnitude change of the resonance peaks before and after these anti-resonances responsible for how much the anti-res frequency shifts? This and more will be further defined in the upcoming section.

The mode shapes of a simple free-free beam as presented in Figure C.3a are used for this guideline. Sensor and impact are placed at position x_s and x_i between 0 and L . The value X_n at this location is a measure to which degree a mode n is sensed and triggered respectively. In general sensors and impacts are placed close together with respect to the relevant structure size. It means that they are also located closely together with respect to the size of the mode shape. This again means that the level of excitation and measurement of mode n are near equal.

Lets consider the impact placed at $x = 0$ and the sensor is placed at $x = 0.01$. It can be seen that the difference between magnitude of sensor and impact increases with the mode number as can be seen in Figure C.3b. Whereas when moving sensor with impact the differences between the modes are not that significant and also the magnitude varies not that much due to a certain displacement.

Figure C.4 shows the following equations:

$$\text{Mode Excitation Level} = \frac{|X_n(x_s)|}{|X_n(x_i)|} \tag{C.1}$$

For a fixed distance d between impact and sensor and moving both with dx the formula becomes:

$$\text{MEL}(dx) = \frac{|X_n(x_s + dx)|}{|X_n(x_s + d + dx)|} - \frac{|X_n(x_s)|}{|X_n(x_s + d)|} \tag{C.2}$$

Moving only the impact with a distance dx results is the following equation:

$$\text{MEL}(dx) = \frac{|X_n(x_s)|}{|X_n(x_s + d + dx)|} - \frac{|X_n(x_s)|}{|X_n(x_s + d)|} \tag{C.3}$$

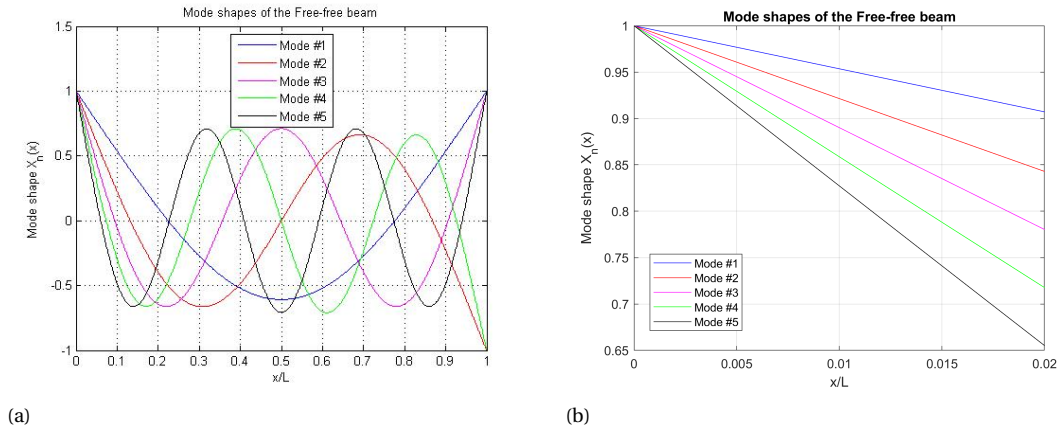


Figure C.3: Mode Shapes

As previously mentioned the level to which a mode is excited does not vary with respect to dx when relative distance is a fixed value as represented by Equation C.2. Differences becomes larger when d is small. So impacts very close to a sensor is very sensitive towards a positional error.

From the MEL value with only moving impact, large differences are observed as a function of the value dx and the relative distance d .

It is now proven that assuming a modal model, the degree to which a mode is triggered varies when relative distance between impact and sensor is changed. The Mode Excitation Level does not change if sensor and impact are positional varied with an equal value. The fact that the MEL varies is responsible for the offset seen for the anti-resonance frequencies.

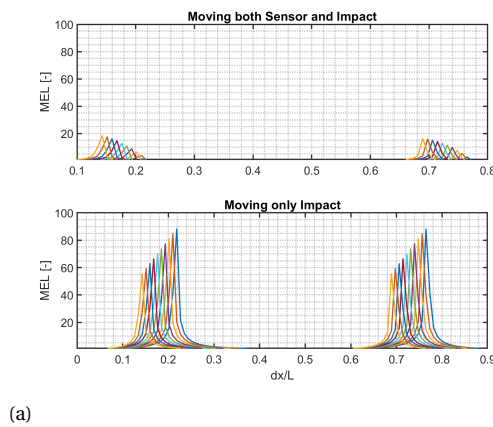


Figure C.4: Mode Excitation Level

What's left is the explanation for the fact that certain anti-resonances are shifting more than others. It is therefore interest to consider the same equations as before but examine them for different modes.

The following conclusion can be drawn from the free-free beam example:

- Sensor and Impact location determines to which degree a certain mode is measured and excited respectively.
- Sensor and impact close together show less sensitivity to moving both impact and sensor equally over the surface.
- Moving both sensor and impact shows less variation as when only impact is moved by the same distance. Sensitivity increases with the starting distance between impact and sensor.
- The ratio between relative distance between sensors and impact and the size of the mode shape is

measure for the sensitivity. More exact: the distance and the dominant mode shape size for a certain axes.

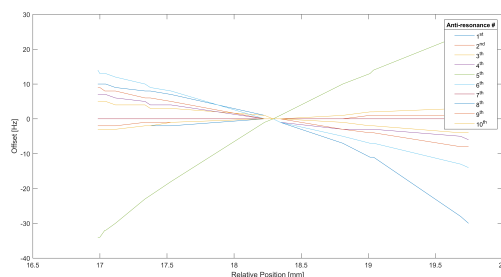
-

The different impact position results in;

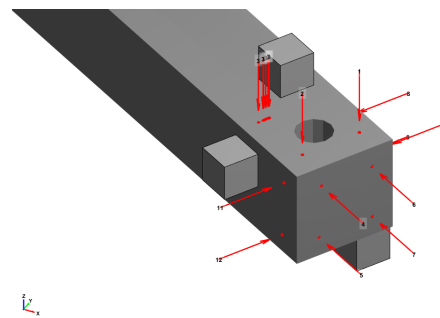
- exciting the structure in a different location
- changing relative distance with respect to sensor locations

What if the impact offset is taken relative to the sensor position from which the signal is being observed. Results for this are shown in Figure C.5. The position is varied in parallel with the x-axis of the virtual point as can be seen in Figure C.5b. A clear relation can be observed between the absolute positional offset between sensor and impact and the anti-resonance frequency shift. It can therefore be stated that the distance between impact and sensor plays a dominant roll when it comes down to the anti-resonance frequency shift. Differences in sensitivity is observed for the anti-resonance frequencies, but they all show a near linear relation as a function of relative offset. The lines all goes trough zero because they are normalized for the correct FRF with the corresponding anti-resonance values. The lines do not show the same angle and therefor not every anti-resonance has the same sensitivity towards the positional offset of the impact. With this results the following can be concluded:

- The position at which the structure is hit is not directly responsible for the observed anti-resonance frequency shift.
- The relative distance between impact and sensor position plays a dominant roll when it comes down to the anti-resonance frequency shift.
- The lines do not show the same angle and therefor not every anti-resonance has the same sensitivity towards the positional offset of the impact.



(a) Relation



(b) 3D view offset

Figure C.5: Effect of relative positional offset on anti-resonance frequency shift

It is now known that the impact position mainly affects the anti-resonance region. From practical knowledge it is known that a set of multiple impacts at the same intended location is used to improve results. But how in general are FRFs influenced by averaging and how does it affect the obtained virtual point transformed FRFs. In the next chapter a more in-depth view on this is presented.

C.2. Effect of Impact Direction

Apart from the fact that hitting the structure can be done off-position the impact hammer can also hit the object under a slight angle. In this small study the angle of the impact hammer is varied while the impact-position is held fixed. This variation is shown in Figure C.6 where the angle of impact 5 is varied within in 3D environment of the Vibes Toolbox. The angle is varied randomly between ± 5 around the x- and y-axes of the virtual point coordinates.

Observing the FRF presented in Figure C.7, between the impact and a parallel sensor channel results in the following conclusions:

- Differences are minimal in terms of magnitude and location of (anti-)resonance frequencies.
- Minor anti-resonance frequency offset at higher frequency.

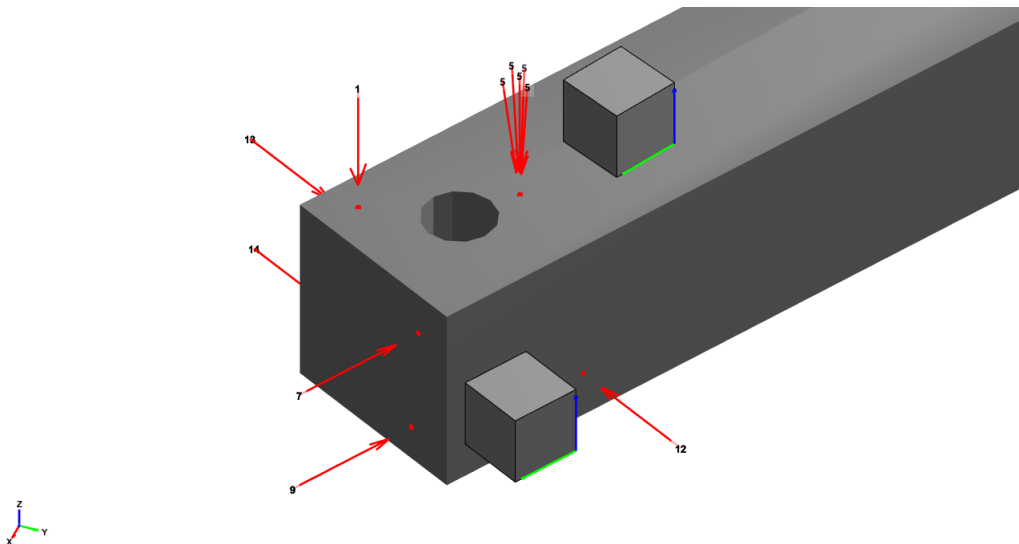


Figure C.6: Impact 5 hitting under different angles

The fact that differences are minimal can be explained by the fact that;

- the angle α between intended impact direction and relevant sensor channel is a measure for the sensitivity
- the measured signal is the $\cos \alpha$
- $\frac{\partial \cos \alpha}{\partial \alpha} = \sin \alpha$ is a measure for the sensitivity towards a directional offset

Figure C.8 shows the sine as a function of angle in radians. Taken the case of an aligned sensor channel the angle is zero and zero is the indicator towards sensitivity. Taken a perpendicular sensor channel, meaning $\alpha = \pi/2$, the sensitivity is at its maximum.

From this observations the following conclusions can be drawn:

- Small impact angle offset has large effect of FRF obtained in perpendicular sensor channels
- $\sin \alpha$ is an indicator for the sensitivity towards a directional offset
- Impact angle error can be detected by low frequency magnitude offset and therefor low frequency coherence of perpendicular sensor channels

For this case the sine of the angle is an indicator for how much the perpendicular sensor channels are triggered. A small angle results in a large variation of input magnitude which is assumed to be zero. It is therefor reasonable to assume that the effect must be clearly visible on a FRF of a sensor channel pointing perpendicular to the intended impact direction. It can be seen from the results in Figure C.9 that the impact angle error has a significant effect on the perpendicular direction FRFs. The magnitude at lower frequencies show a significant variation, as a result of the previously mentioned sine of the impact angle which is very sensitive. The effect is not so continuous as it was for the impact positioning. Looking further ahead these perpendicular sensor channels are used to construct the cross stiffness's which are known to be very hard to determine. It is therefor important to check the lower frequency coherence for perpendicular sensor channels.

One result of a directional error leads to an increase of impact in the directions other than the one hitting in. Because the angle of impact determines at which direction the magnitude becomes larger, the results of both other directions needs to be considered. For example when hitting in the Z-direction, the results of the X- and Y-direction needs to be considered. The absolute magnitude of both FRFs will result in a measure that can detect directional errors in impacts. There cannot be sought for a minimum because modes can be strengthened as well as weakened.

$$IMPACT_z = \sqrt{FRF_x^2 + FRF_y^2} \quad (C.4)$$

It is found that the real value of Equation C.4 is a good indicator for finding wrong directional impacts. Figure C.10 shows zoomed views of interest for this section. It can be seen that the real value shows great sensitiv-

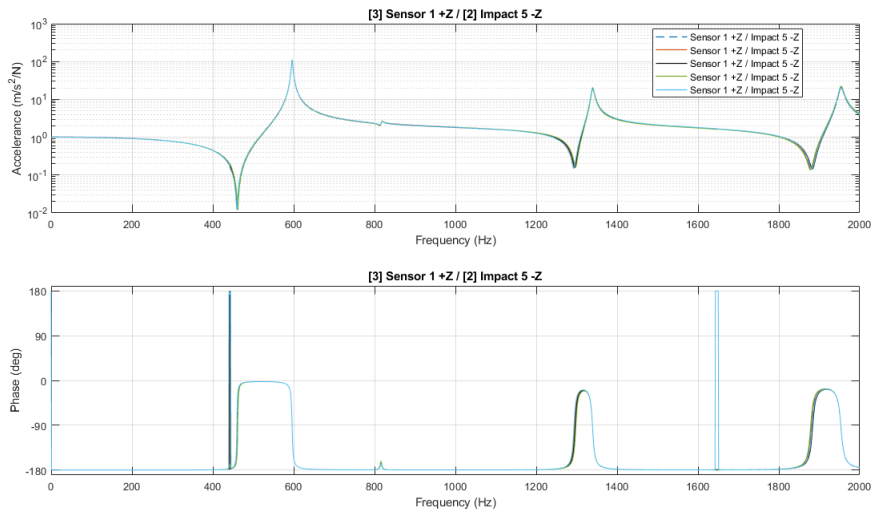


Figure C.7: FRF to parallel sensor channel

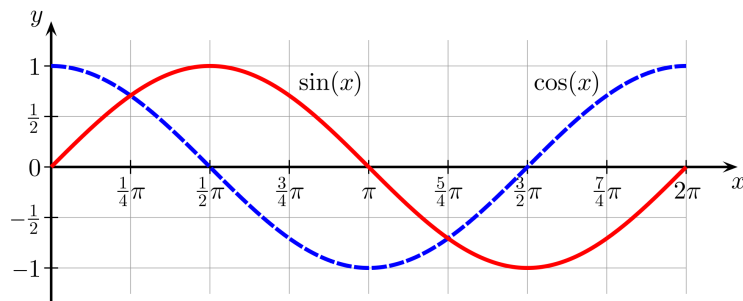


Figure C.8: Sine and Cosine function plots

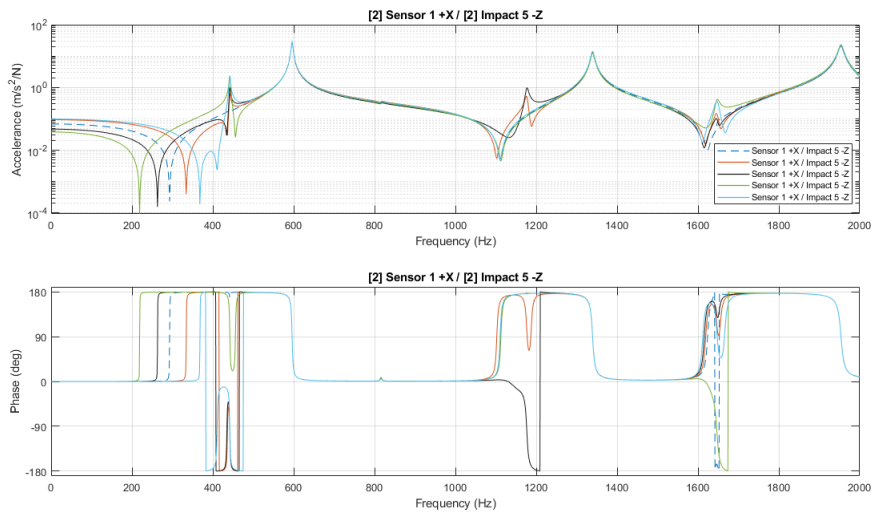


Figure C.9: FRF of a perpendicular sensor channel

ity towards the impact direction. Less disturbance is observed around this frequency for the correct impact. It is shown that certain frequency regions are extra sensitive for directional variations while at other frequencies the differences are minor. The degree of sensitivity is indirect effect of the sensitivity of the dominant modes

before and after this location. The sensitive region can be used for detection of directional misalignment between sensor and impact.

The regions at which this effect occurs are characterized by the so called flipping, which means that the angle determines if there first comes a peak or a dip. The region can be found by taking the derivative from the signal and find where variance is large. These regions are determined with this working principle.

1. determine $re[FRF_x + FRF_y]$
2. find variance between a set of impacts
3. search for maximum values and determine corresponding frequencies

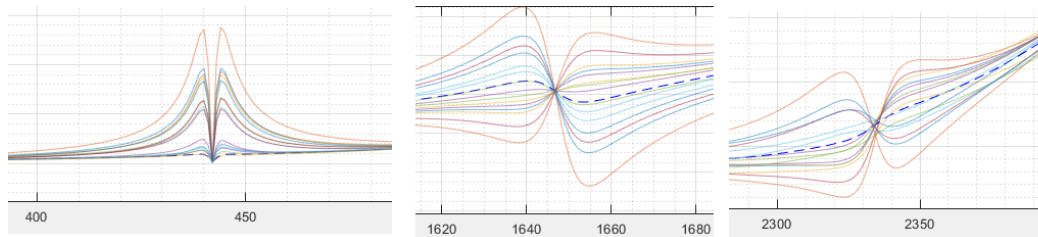


Figure C.10: Absolute FRF of perpendicular sensor channels

From this observation the following conclusions can be drawn:

- At the sensitive frequency region of absolute perpendicular sensor channels directional error can be detected.
- Sensitive region can be detected by finding region where derivative shows large variance.
- Orthogonal sensor channels show directional error sensitivity. The degree of sensitivity depends on how easily the structure is excited in the direction of that specific channel. A dominant factor for this can be the inertia of the structure.

Another interest observation is that not every orthogonal sensor channel has the same sensitivity. The channel which points most towards a low inertia direction shows the most sensitivity. It can be explained by the fact that the structure is excited more easily in that direction due to the small angle at which the structure is hit.

C.3. Averaging of FRFs

In this section the observed effects due to positional and directional errors are considered and it is found how averaging is affected by these observations.

C.3.1. Averaging a set of positional variations

In this section the focus lies on finding how averaging affects the obtained FRFs. From the previous section the effects are known and focus lies on these points. First recap which differences are expected;

- Mishitting determines to which level the individual modes are triggered, which leads to;
- magnitude differences and therefor;
- anti-resonance shifts

Currently the following averaging steps are taken in experimental situations:

1. Standard averaging of multiple hits intended at the correct and same location. Coherence of a set of impacts is visually inspected for all sensor channels. Low coherence channels are removed.
2. IDM filtering which defines the virtual point FRF from a linear combination of obtained direct FRFs.
3. Step two is done after step one which makes the normal averaging effect being active within two steps.

The first goal is to find answer to the following question:

- What local effect has averaging on the position and the magnitude of the (anti-)resonance?

Again the Toolbox is used to vary impact position. One impact is varied over the surface that is hit. To give a more broader view on the problem multiple plots are used for the analysis: magnitude and phase but also

real and imaginary values.

The first case is where only error is introduced such that impact position is randomly distributed around the intended point of impact. The positional offset within a circle of 2 mm around the intended position. Such a range is picked because it seem a reasonable offset for precise hammering. It can be seen from the plots that the correct FRF is located in between the range of the maximum deviating FRFs. This leads to the idea that averaging is reasonable to improve results. Averaging and considering a random impact offset the mean FRF lead to;

- More precise location of anti-resonance frequencies
- Improved magnitude over full frequency range
- Weakened magnitude of actual FRF at (anti-)resonance frequencies

It should be noted that the random error is expected to be the main reason for this method to work. Can we draw a more valuable conclusion from the results so far? Plotting the anti-resonance frequency offset with respect to positional offset no direct relation can be observed. Not for offset in x-,y-direction nor the absolute offset. The position at which the structure is hit is therefor not responsible for the observed anti-resonance shift.

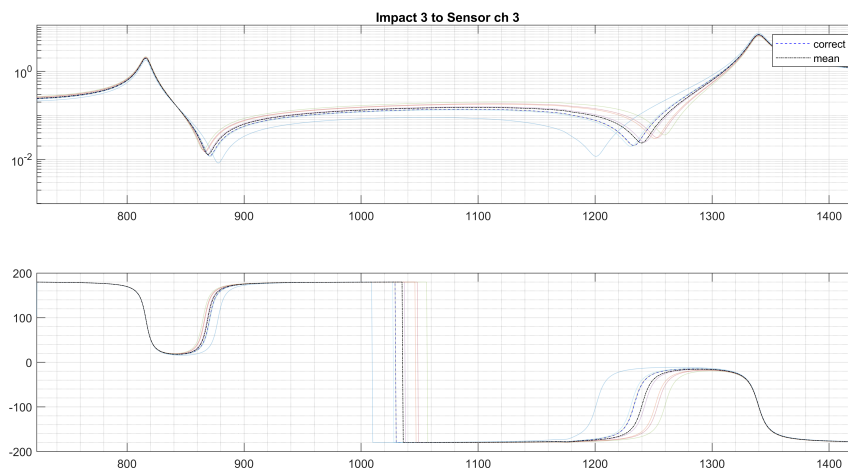


Figure C.11: Mean vs. Correct FRF due to positional variations

A normal averaging would result in equal contribution of every impact. With the linear relation observed between distance and anti-resonance shift normal averaging is able to improve results. The effect of averaging is presented in Figure C.11 where the transparent lines are variations from which the average is taken. The general shape of the FRF is also preserved. The effect of hitting the structure randomly around a known location can be averaged out and results can be improved. It is however questionable if this is reasonable to assume? Does a person hit the structure randomly around the intended locations? That is questions which will be answered later on.

C.3.2. A set of directional variations

As for the averaging of positional variations, also the averaging of directional variations needs to be considered. For example Figure C.12 shows an averaged FRF for a set of directional varied impacts. The most sensitive sensor channels are the orthogonal ones relative to the impact and the result of such a channel is presented in Figure C.12. The transparent lines show the individual variations where as also the correct and averaged FRFs are shown. The large magnitude deviation at the low frequencies results in significant difference in that region and also at the first (anti-)resonance frequency. Towards higher frequency the difference becomes smaller and averaging is moving the mean FRF towards the correct one.

- Low frequency magnitude offset results in large deviation around the first (anti-)resonance frequency.
- Averaging leads to large error at lower frequency.

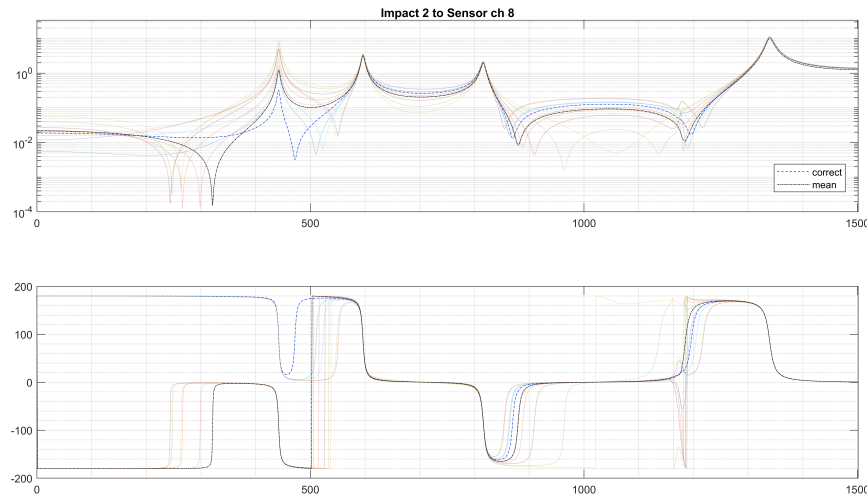


Figure C.12: Averaged FRF of directional variations

C.3.3. Coherence check vs. Averaging

It is known from practice that the following is a normal working principle;

1. hit multiple times at intended location
2. eliminate signals that improves coherence, normally check for sensitive sensor channels.
3. use a set of two or three impacts for averaging

A coherence check is used for finding consistent data, which means that the impact excites the same dynamics as others. This generally spoken means that weak or noise signals are removed. It also results in removing impacts that lie most far away from the set of impacts because this deviates the most from the average. A consistent set of impacts is created with the coherence check, but nothing can be said if the impacts that are left are in fact closer to the intended position. Exact position of the impact needs to be determined in a later stadium.

C.3.4. Random vs. Continuous error

Up to now the error that is introduced is taken as a random offset. From practical knowledge it is however expected that the offset is not only random but also of a continuous form. Averaging will not lead to finding an improved FRF of the intended location. The averaged FRF will become more a represent of a location in the middle of the random error. It is therefore questionable if averaging is useful when also continuous error is introduced due to human interaction. So averaging can not lead to a FRF positioned at the intended location. Assuming this is true, averaging generally spoken lead to a weaker signal of an unknown location. In this work tactics are discussed which are used to find the impact position and these techniques will be assumed to perform less when averaging is done.

- The averaged FRF will become more a represent of the middle of the random error
- Averaging does not lead to FRF of the intended position if continuous error is assumed
- FRF becomes less sensitive for impact improvement techniques
- Coherence check leads to removing impacts most far away from the set of impacts.

C.4. Summary

In the previous section effects of varying both position and direction of an impact are analyzed. This means position along the surface is varied as well as the angle under which it hits the specific surface. This is of interest because humans are performing the hammering and knowing exact location and direction of the impact is key for obtaining a good virtual point.

C.4.1. Positioning variations

For a change in position the following results are being observed;

- Anti-resonance frequency offset
- No resonance frequency offset
- Offset gets larger at higher frequency
- Magnitude difference observed at full range of frequency
- General shape of FRF are minimally affected by mishitting
- Magnitude order flips after resonance peaks

It is found that the change of relative distance between sensor and impact results in the anti-resonance frequency shift. The magnitude of modes are measured differently which results in a difference that leads to the anti-resonance frequency shift. A linear relation between relative distance and anti-res frequency shift is observed where different sensitivity is observed for a multiple of anti-resonances.

For improvement by taking a set of impacts at the same intended location, averaging effects are considered. It is shown that averaging can minimize the effect of random errors. Because hammering is human work the assumption that impact position is randomly but equally distributed may not be valid. When also continuous error is considered, the effect of averaging becomes questionable. The FRF of the intended impact location can no longer be reconstructed so averaging will only lead to weakened signal of an unknown impact location due to the continuous error. Averaging can make the FRF less sensitive for techniques for finding exact impact location and therefore less useful. Considering continuous errors are relevant and significant the following working principle is advised;

1. Hit structure multiple times at intended location
2. Select a set of high coherence impacts with a focus on anti-resonance frequency regions. A set of high coherence impacts makes it that good dynamics are triggered. It will not lead to selecting impact closer to the intended impact location.
3. Precise impact location is unknown and therefore use only one impact of the set for constructing the virtual point FRFs when impact location search techniques are being used later.

C.4.2. Directional variations

Error can also be introduced by hitting the structure under a slight angle. A change of angle has only minor effect due to the fact that the change in magnitude in parallel to the intended direction is very small. For a more intuitive perspective it can be seen as the derivative of the sine and cosine functions. The change in parallel with the impact is represented by the derivative of the cosine where as the change orthogonal to the impact is represented by the derivative of the sine. At and around a near zero angle the change (derivative) of the cosine function is also near zero where as the derivative of the sine function is at its maximum. This fact makes it that orthogonal sensor channels show large sensitivity towards directional variations of an impact.

It is also proven that the orthogonal sensor channels show difference dependency towards to directional offset of an impact. It is observed that the channel which points most towards a low inertia direction shows the most sensitivity. It can be explained by the fact that the structure is excited more easily in that direction due to the small angle at which the structure is hit.

Again for the orthogonal sensor channels FRFs are obtained which does not show enough comparison to think that averaging would result in an improved FRF. The large magnitude deviation at the low frequencies results in significant difference in that region and also at the first (anti-)resonance frequency. Towards higher frequency the difference becomes smaller and averaging is moving the mean FRF towards the correct FRF. In terms of directional error a method is presented to find for the most optimal impact which is the most perpendicular impact of the set available. For example when hitting in the Z-direction, the accelerations of the X- and Y-direction needs to be considered. The absolute magnitude of both FRFs should be minimal at near zero Hz and can be determined at all sensors. The one impact that shows the lowest value is considered to be the most optimal of the set of impacts available.



Software

D.1. Software interaction

In this section it is explained how the interaction between Matlab, Python and Abaqus is effectively integrated with the goal of obtaining the dynamic stiffness as a function of frequency. A list of files that are used during the analysis:

Original files

- Matlab run file
- Matlab optimization file
- Matlab parameter file
- Python main script
- function files

Created files

- python script with variables
- .ODB Output DataBase file
- .txt files with relevant data from .ODB
- .INP input file

Next the working principle is explained by the steps below. The steps are seen from the *main run file* point of view:

- Runs parameter file
 - variables can be edited in this file. A list of the variables is shown in Table D.1
 - viscoelastic data is read from *DMA_dataset.txt*
 - viscoelastic data is transformed to a so called tabular form which can be handled by Abaqus
 - relevant variables are written to python script named *variables.py*
 - makes changes to the main script used by Abaqus
 - ◊ varies BC of the VPs, which cannot be inputted through the *variables.py* file
- Runs Abaqus simulation making use of main python script
 - reads variables from the *variables.py* file
 - starts Abaqus with or without GUI
 - script for building up the complete FE model
 - ◊ create cylinder part + two VPs
 - ◊ assemble the parts
 - ◊ apply material properties
 - ◊ create node sets with coupling
 - ◊ create steady state dynamic direct step
 - ◊ apply BC
 - ◊ apply mesh
 - ◊ job submission
 - ◊ save relevant data by executing *save_dyn_data.py* file
- Determine complex dynamic stiffness matrix
 - read data from .txt
 - use *K_column.m* function file to calculate one column of complex dynamic stiffness matrix

- Repeat the simulation for all DOF and VPs
- Optimize material model data and repeat the process

Table D.1: Editable variables

Variable name	Description	Unit
Material		
par.mat.E	Elastic modulus	[N/mm]
par.mat.poisson	Poisson Ratio	[-]
par.mat.rho	Density	[Tonne/mm ³]
Geometry		
par.size.t	Thickness cyl.	[mm]
par.size.r	Radius cyl.	[mm]
par.VP.VPin	Coordinates VP input	[mm]
par.VP.VPout	Coordinates VP output	[mm]
Mesh		
par.mesh.size	element size	[mm]
Step		
par.step.f_points	# frequency data points	[-]
par.step.f_min	min. frequency of interest	[Hz]
par.step.f_max	max. frequency of interest	[Hz]
par.step.f_bias	distribution of points	[-]
par.disp	amplitude harmonic excitation	[mm & rad]
par.jobname	name of job	[string]
par.mo	run with(out) GUI	[string]

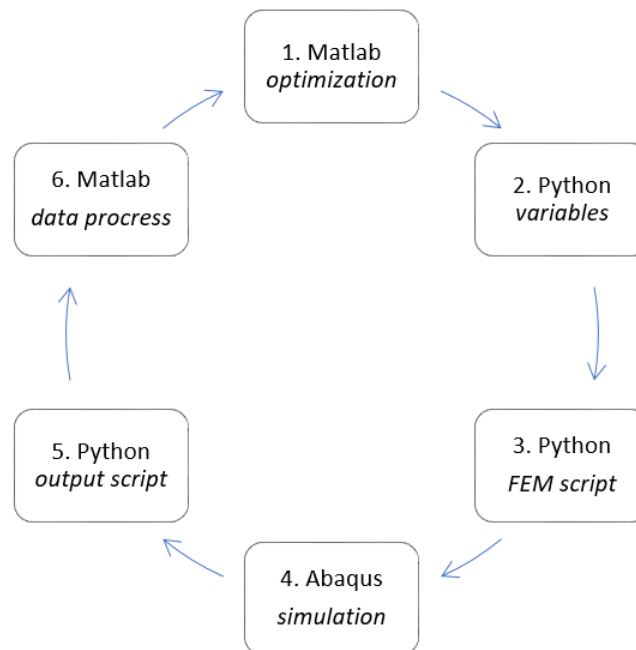


Figure D.1: Flow chart of the software interaction

D.2. Data-processing

The process of transforming the data obtained from the Abaqus simulations to the dynamic stiffness is explained in more detail in this section. The post-processing starts with the *.txt* files written by Abaqus. This

file contains the complex valued reaction forces and displacements for all relevant DoF of the virtual points. These are outputted for every step and frequency point.

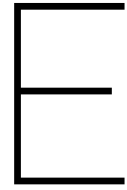
Multiple steps of the steady state dynamic direct analysis are performed to compute the complete dynamic stiffness matrix. Within each step a frequency sweep is executed with a harmonic excitation in one DOF where the others are fixed in their movement. Displacement and reaction forces within the two virtual points are stored and used.

The basics for the dynamic stiffness calculation are the forces and displacements. The dynamic stiffness matrix consist of 12x12 elements which are a result of six DOF for each two virtual points. The stiffness matrix is build up by individual columns that are resulting from each step. All the reaction forces divided by the displacement of the oscillating DOF result in the column of the stiffness matrix in the free moving DOF.

Due to multiple symmetric properties it is needed to execute minimal number of four simulations. The magnitude and phase of both displacement and force are handled separately. It is therefore needed to calculate the dynamic stiffness in an alternative way. Magnitude and phase of the dynamic stiffness are calculated with equation D.1 and D.2.

$$|Z_{mn}| = \frac{|f_m|}{|u_n|} \quad (D.1)$$

$$\angle Z_{mn} = \angle f_m - \angle u_n \quad (D.2)$$



Additional Experimental Results

E.1. Validating matrix symmetry

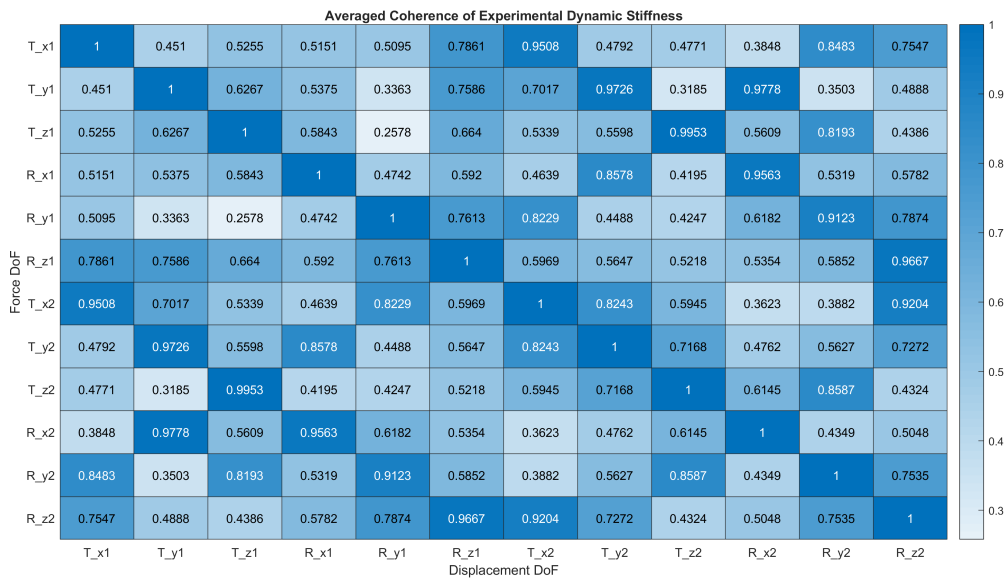


Figure E.1: Checking matrix symmetry by making use of the coherence function. The coherence of the full 12x12 matrix can indicate the consistency of the two transfer-stiffness measurements. The diagonal terms of the transfer-stiffness shows a high coherence value which is good. In general it is clear that multiple cross-stiffness values are hard to determine.